

# Updating the treatment of the direct aerosol effect in the Global Environmental Multiscale model with Atmospheric Chemistry (GEM-AC)

Jennifer L. Beale

A Dissertation submitted to the faculty of graduate studies in partial fulfillment of the  
requirements for the degree of  
Doctor of Philosophy

Graduate Program in Atmospheric Science  
York University,  
Toronto, Ontario

June 2016

© Jennifer Beale, 2016

# Abstract

Atmospheric aerosols alter the atmospheric energy budget through their scattering, absorption, and emission properties within certain spectral bands. The direct aerosol effect is a fundamental aspect of every climate and chemical transport model. Aerosol optical properties are incorporated into the Global Environmental Multiscale model with Atmospheric Chemistry (GEM-AC) which is equipped with the M7 aerosol submodel. With the recent progress in atmospheric and chemical transport modelling, an interactive dust emission scheme and a sea-state dependent sea salt emission scheme are also implemented in GEM-AC. An option between volume fraction mixing and Bruggeman mixing for the mixing state of soluble aerosols is provided. In addition, there is an option to include the aerosol direct effect at all nine longwave spectral bands in GEM-AC. Eight experiments are performed to document the new direct effect of the M7 aerosols and the effects of: the aerosols in all nine longwave spectral bands, the soluble aerosol mixing state options, the interactive dust scheme, and the sea-state dependent sea salt emission scheme. Aerosol optical properties are compared against three AERONET observation sites. Implementation of the aerosol direct effect and the new aerosol options in GEM-AC maintain the model as a practical tool for climate and chemical transport modelling.

# Acknowledgements

My dissertation is in memory of my advisor, John C. McConnell (1945-2013), who left us far too early, but indelibly left us with his unremitting curiosity and his eternal motivation to question everything.

Thank you Jacek Kaminski, Kirill Semeniuk, and Alex Lupu for getting GEM-AC into a state such that my model additions and dissertation could be completed.

And thank you Tom McElroy and Jacek Kaminski for taking me under your wings to see my dissertation through.

*For everyone who has ever taught me anything.*

*Steve,*

$$\sqrt{-1} \quad l \in \{V\} \quad \int_0^u du' \quad \frac{1}{0}$$

# Contents

<b>Abstract</b>	<b>ii</b>
<b>Acknowledgements</b>	<b>iii</b>
<b>Table of Contents</b>	<b>v</b>
<b>List of Figures</b>	<b>viii</b>
<b>List of Tables</b>	<b>xi</b>
<b>1 Introduction</b>	<b>1</b>
1.1 Background . . . . .	1
1.2 Outline . . . . .	5
<b>2 Motivation</b>	<b>7</b>
2.1 Objectives . . . . .	7
2.2 Motivating Example: A Simple Case of Atmospheric Aerosol Heating and Cooling . . . . .	8
<b>3 Model Configuration</b>	<b>13</b>
3.1 GEM-AC Domain . . . . .	13
3.2 GEM-AC Radiative Transfer . . . . .	14
3.3 M7 Size Distribution Configuration . . . . .	14

<b>4</b>	<b>Extensions to the GEM-AC Model</b>	<b>18</b>
4.1	Aerosol Optical Property Calculations . . . . .	18
4.2	Interactive Dust Aerosol Emissions . . . . .	29
4.3	Significant Wave Height Dependent Sea-Salt Aerosol Emissions . . . . .	32
<b>5</b>	<b>Modelling Scenarios and Discussions</b>	<b>35</b>
5.1	Experiment Descriptions . . . . .	35
5.2	Aerosol Optical Property Distributions . . . . .	37
5.3	Aerosol Mode and Species Distributions . . . . .	58
5.4	Example of an Implication for Atmospheric Chemistry . . . . .	64
<b>6</b>	<b>Conclusion</b>	<b>68</b>
6.1	Contributonal Objective . . . . .	68
6.2	Contributonal Results . . . . .	69
6.3	Limitations of this Research . . . . .	69
6.4	Recommendations for Future Work . . . . .	70
6.5	Final Remark . . . . .	70
	<b>Appendices</b>	<b>72</b>
<b>A</b>	<b>Motivation and Background of Atmospheric Dust Modelling on Mars</b>	<b>73</b>
<b>B</b>	<b>Simple Column Model of Dust in the Mars Atmosphere</b>	<b>77</b>
B.1	The Size and vertical distribution . . . . .	77
B.2	Optical Properties . . . . .	78
B.3	Radiative transfer parameterization . . . . .	85
<b>C</b>	<b>Radiative Heating and Cooling of Mars Dust Aerosol</b>	<b>93</b>

C.1 Heating rates of upper-level dust maximum scenarios . . . . .	94
C.2 Sensitivities to the ground temperature and surface emissivity . . . . .	97
C.3 Sensitivities to the effective radius and effective variance . . . . .	100
C.4 Effects of linearly decreasing $R_{eff}$ and $\nu_{eff}$ . . . . .	103
C.5 A single dust size versus a size distribution . . . . .	105
C.6 Dust impacts under nighttime temperature conditions . . . . .	109
<b>D Global and Zonal Averages of Soluble Aerosol Number Densities</b>	<b>112</b>
<b>E Global and Zonal Averages of Insoluble Aerosol Number Densities</b>	<b>121</b>
<b>F Global and Zonal Averages of the Aerosol Species</b>	<b>128</b>
<b>G Seasonal Global Load Averages of Aerosol and Chemical Species</b>	<b>145</b>
<b>Bibliography</b>	<b>151</b>

# List of Figures

2.1	The Mars dust column. . . . .	12
3.1	Aerosol mixing states . . . . .	16
4.1	Absorption difference between externally mixed and internally mixed aerosols	22
5.1	2012 10 m aerosol optical depth . . . . .	40
5.2	2012 zonally averaged aerosol optical depth . . . . .	42
5.3	2012 10 m aerosol absorption optical depth . . . . .	43
5.4	2012 zonally averaged aerosol absorption optical depth . . . . .	45
5.5	2012 10 m aerosol single-scattering albedo . . . . .	46
5.6	2012 zonally averaged aerosol single-scattering albedo . . . . .	47
5.7	2012 10 m aerosol asymmetry parameter . . . . .	48
5.8	2012 zonally averaged aerosol asymmetry parameter . . . . .	50
5.9	GEM-AC output versus AERONET: December 2012 at Calhau, Cape Verde	52
5.10	GEM-AC output versus AERONET: July 2012 at Dakar, Senegal . . . . .	53
5.11	GEM-AC output versus AERONET: December 2012 at Dakar, Senegal . . . . .	54
5.12	GEM-AC output versus AERONET: July 2012 at Ispra, Italy . . . . .	54
5.13	2012 10 m air temperature . . . . .	57
5.14	2012 zonally averaged air temperature . . . . .	59
5.15	2012 10 m N <sub>2</sub> O <sub>5</sub> volume mixing ratio . . . . .	66
5.16	2012 zonally averaged N <sub>2</sub> O <sub>5</sub> volume mixing ratio . . . . .	67

B.1	Mass mixing ratio and total number density profiles . . . . .	79
B.2	Real and imaginary Mars dust refractive indices. . . . .	81
B.3	Mars dust optical properties as a function of dust size . . . . .	84
C.1	Heating rates and flux divergences. . . . .	96
C.2	Heating rates for total vertical optical depths 1.0, 2.0, and 5.0 . . . . .	97
C.3	Heating rates for varying $T_G$ and $\varepsilon$ . . . . .	100
C.4	Heating rates for varying $R_{eff}$ and $\nu_{eff}$ . . . . .	101
C.5	Heating rates for linearly decreasing $R_{eff}$ and $\nu_{eff}$ . . . . .	105
C.6	Heating rates for a single-size dust particles versus a size distribution of dust	106
C.7	Heating rates for nighttime conditions . . . . .	110
D.1	2012 10 m mode 1 aerosol number concentration . . . . .	113
D.2	2012 zonally averaged mode 1 aerosol number concentration . . . . .	114
D.3	2012 10 m mode 2 aerosol number concentration . . . . .	115
D.4	2012 zonally averaged mode 2 aerosol number concentration . . . . .	116
D.5	2012 10 m mode 3 aerosol number concentration . . . . .	117
D.6	2012 zonally averaged mode 3 aerosol number concentration . . . . .	118
D.7	2012 10 m mode 4 aerosol number concentration . . . . .	119
D.8	2012 zonally averaged mode 4 aerosol number concentration . . . . .	120
E.1	2012 10 m mode 5 aerosol number concentration . . . . .	122
E.2	2012 zonally averaged mode 5 aerosol number concentration . . . . .	123
E.3	2012 10 m mode 6 aerosol number concentration . . . . .	124
E.4	2012 zonally averaged mode 6 aerosol number concentration . . . . .	125
E.5	2012 10 m mode 7 aerosol number concentration . . . . .	126
E.6	2012 zonally averaged mode 7 aerosol number concentration . . . . .	127

F.1	2012 10 m ASO <sub>4</sub> volume mixing ratio . . . . .	129
F.2	2012 zonally averaged ASO <sub>4</sub> volume mixing ratio . . . . .	130
F.3	2012 10 m ANH <sub>4</sub> volume mixing ratio . . . . .	131
F.4	2012 zonally averaged ANH <sub>4</sub> volume mixing ratio . . . . .	132
F.5	2012 10 m ANO <sub>3</sub> volume mixing ratio . . . . .	133
F.6	2012 zonally averaged ANO <sub>3</sub> volume mixing ratio . . . . .	134
F.7	2012 10 m AH <sub>2</sub> O volume mixing ratio . . . . .	135
F.8	2012 zonally averaged AH <sub>2</sub> O volume mixing ratio . . . . .	136
F.9	2012 10 m AOC volume mixing ratio . . . . .	137
F.10	2012 zonally averaged AOC volume mixing ratio . . . . .	138
F.11	2012 10 m ABC volume mixing ratio . . . . .	139
F.12	2012 zonally averaged ABC volume mixing ratio . . . . .	140
F.13	2012 10 m ADU volume mixing ratio . . . . .	141
F.14	2012 zonally averaged ADU volume mixing ratio . . . . .	142
F.15	2012 10 m ASEA volume mixing ratio . . . . .	143
F.16	2012 zonally averaged ASEA volume mixing ratio . . . . .	144

# List of Tables

3.1	M7 size distribution: partitioning of the emitted modes (BASE experiment)	17
3.2	M7 size distribution: partitioning of the transported modes (BASE experiment)	17
4.1	Size parameter and refractive index bins used to generate the three-dimensional optical property input tables . . . . .	21
4.2	Wavelength dependent refractive indices of the eight aerosol species . . . . .	28
4.3	Dust emission parameters . . . . .	30
4.4	Dust emission bounding diameters . . . . .	30
4.5	Sea-salt emission number fluxes . . . . .	34
5.1	List of experiments . . . . .	36
5.2	2012 selected AERONET sites . . . . .	49
5.3	2012 global averages of 10 m temperature . . . . .	58
5.4	2012 global averages of aerosol mode number density . . . . .	61
5.5	Annual global load averages of aerosol species and chemistry . . . . .	63
B.1	Wavelength band single-scattering albedos and asymmetry factors of each size distribution configuration . . . . .	86
B.2	Two- and four- stream combination parameters. . . . .	90
G.1	Winter 2012 global averages of aerosol mode number density . . . . .	146
G.2	Spring 2012 global averages of aerosol mode number density . . . . .	146

G.3	Summer 2012 global averages of aerosol mode number density . . . . .	146
G.4	Autumn 2012 global averages of aerosol mode number density . . . . .	147
G.5	Winter global load averages of aerosol species and chemistry . . . . .	147
G.6	Spring global load averages of aerosol species and chemistry . . . . .	148
G.7	Summer global load averages of aerosol species and chemistry . . . . .	149
G.8	Autumn global load averages of aerosol species and chemistry . . . . .	150

# Chapter 1

## Introduction

### 1.1 Background

Aerosols significantly and directly effect the net energy flux balance in the atmosphere through scattering and absorption of solar radiation and through the absorption of planetary radiation (Haywood and Boucher (2000), IPCC Fifth Assessment Report 2013). While aerosols also indirectly effect the earth system (modification of cloud properties (Twomey, 1959; Albrecht, 1989; Lohmann and Feichter, 2005), feedback on the hydrological cycle (Ramanathan et al., 2001; Ramachandran and Kedia, 2013), impact on the ocean biogeochemical cycle (Johnson et al., 2003; Mahowald et al., 2011), interaction with atmospheric chemistry (Andreae and Crutzen, 1997; Tang et al., 2003), and contribution to air quality (Poeschl, 2005; Fuzzi et al., 2015)), this dissertation focuses on the aerosol direct effect.

The scattering and absorption by aerosols is a complex process to capture in climate, atmospheric chemistry and transport models. The optical properties of aerosols quantify their scattering and absorption, while the aerosol size distribution, composition, solubility, and refractive indices control their optical properties. These parameters, however, have large spatial and temporal variability and can be difficult to accurately represent in atmospheric

models. Despite the complexity, aerosol representation is a critical component in atmospheric modelling applications.

The aerosol direct effect is the combined effect that natural and anthropogenic aerosols have on the radiative energy budget. The direct effect by aerosols has been assessed by measurements, models, and integration between models and measurements (Yu et al., 2006). There are three optical properties of aerosols that describe their interaction with radiation: the aerosol optical depth, the aerosol single-scattering albedo, and the aerosol asymmetry parameter. The aerosol optical depth is the distance over which radiation is attenuated by a factor of  $e$  due to the scattering and absorption by aerosols through a vertical column in the atmosphere. Aerosol scattering is measured by two parameters: the ratio of the scattered radiation to the total extinction (absorption plus scattering) is the single-scattering albedo, and the angular distribution of the scattered radiation is the asymmetry parameter. Mathematical descriptions of the three aerosol optical properties are given Section B.2.2, B.2.3, and B.2.4. All global models should have representation of these aerosol optical properties because of their interaction with radiation at all wavelengths.

Aerosol optical properties have large spatial and temporal variability which is difficult to capture in global models. Different geographical regions are associated with different aerosol species and each aerosol species is emitted into the atmosphere at varying vertical levels (Dentener et al., 2006; Sofiev et al., 2013; Boichu et al., 2016). The temporal variability of aerosols depends on the atmospheric conditions for emission, nucleation, processing, and transport. In particular, relative humidity is a critical factor in aerosol growth for soluble species (Flores et al., 2012), however, it is strongly variable and can have large uncertainty in the global models due to the large scale circulation and the numerical parameterisations of advection and microphysical processes (Sherwood, 1996; Risi et al., 2012). Upon emission, the aerosol size distribution and chemical composition is altered during atmospheric transport by microphysical processing and interaction with gas-phase molecules which are

generally dependent on relative humidity.

Aerosol optical properties are dictated by their chemical composition. Typically, global atmospheric chemistry and transport models treat five distinct aerosol species: dust, sea salt, sulphate, organic and black carbon. Most recently, the treatment of additional components such as nitrate, ammonium, and secondary organic aerosols has become popular. All aerosol species are capable of soluble mixing. At source regions, however, the aerosol species such as dust, black carbon, and organic carbon are emitted in their natural state as externally mixed aerosol. Atmospheric processing during transport ages the aerosol such that other aerosol species and water can be taken up and condensed upon the aerosol surface. Aerosol optical properties are controlled by the aerosol refractive index, and the aerosol refractive index is controlled by the aerosol chemical composition.

Calculation of the refractive indices of mixed aerosols, either newly emitted or aged during transport, requires an approximation to mixing among the soluble and insoluble aerosol species. Within the last 15 years, as the importance of aerosol solubility to the microphysics became apparent, model development began to distinguish between internally and externally mixed aerosols. The representation of soluble aerosol mixtures within the models requires microphysical modelling to capture the development of the mixture and the equilibrium between the aerosols and water vapour. Soluble aerosol mixing tends to have little effect on the amount the aerosol scatters, however, it can have a large effect on the amount the aerosol absorbs (Stier et al., 2007). Several methods of soluble aerosol mixing exist: the volume fraction method which is computationally efficient but can overestimate aerosol absorption, and the Bruggeman method which is less computationally efficient but does not tend to overestimate aerosol absorption. Both of these methods are applied in this dissertation and are described in Sections 4.1.5 and 4.1.5.

Accurate representation of the aerosol chemical composition also requires accurate emissions from source regions since different aerosol species are associated with different geo-

graphical regions (Owen and Steiner, 2012). Aerosol emissions usually depend on atmospheric conditions and thus most global models seek efficient parameterised emissions that are interactive with the model meteorology. Dust and sea salt have tended to be the focus of the development of interactive parameterisations in global models. Dust aerosol contributes the most to the overall extinction of radiation due to its strong absorption and scattering properties, and extensively interacts with atmospheric chemistry (Wang et al., 2011). Sea salt is emitted from two thirds of Earth’s surface, strongly scatters solar radiation, and easily mixes with other aerosol species (Spada et al., 2013).

The size of an aerosol particle is another major factor governing its optical properties. Aerosol interaction with radiation either scatters or absorbs some fraction of the energy that impinges upon it per cross-sectional area of the particle (Section B.2.1). Atmospheric aerosols range in diameter size from 0.001  $\mu\text{m}$  to 10  $\mu\text{m}$ . The sizes in a population of aerosols tend to be approximated by either a log-normal or a modified gamma distribution in the atmospheric models (McGraw et al., 1998). Upon aerosol emission and in situ formation, aerosols undergo a change in size during subsequent atmospheric processing as the aerosols are transported in the atmosphere. As such, aerosol microphysical processing tends to characterise the modal nature of the aerosol size distribution and impact the aerosol optical properties.

Aerosol size distributions in models are typically represented using aerosol modes or aerosol size bins. For computational efficiency in the global models, the modal approach in the microphysical modelling is often taken as opposed to using sectional size bin methods. Some size bins schemes are the Piecewise Log-normal Approximation (von Salzen, 2006) employed in the fourth generation of the Canadian Atmospheric Global Climate Model (CanAM4) (Peng et al., 2012), the sectional Model for Simulating Aerosol Interactions and Chemistry (MOSAIC) aerosol module used in several versions of the Weather Research and Forecasting model (WRF) (Chapman et al., 2009; Wyant et al., 2015), or the Sectional Aerosol module for Large Scale Applications (SALSA) module installed in ECHAM5-HAM in Berman et al.

(2012). The two common modal microphysical models designed specifically for efficient use in global climate, chemistry, and atmospheric transport models are the M7 model (Vignati et al., 2004), and the Global Modal-aerosol eXtension (GMXe) model (Pringle et al., 2010). The modal aerosol submodel, M7, is used in this dissertation (Section 3.3).

Efficient and accurate aerosol parameterisations are continually improved upon and integrated within global climate, chemistry, and atmospheric transport models. Incorporating the aerosol direct effect along with several recently developed aerosol parameterisations into the Global Environmental Multiscale model with Atmospheric Chemistry (GEM-AC) is a major step in keeping the model practical as continuous advancements are made in atmospheric models.

## 1.2 Outline

As discussed in this introduction, aerosols are central to climate and chemical transport models. Chapter 2 motivates the work presented in this dissertation by demonstrating the fundamentals of the aerosol direct effect using a simple example. This dissertation documents the implementation of the direct aerosol effect, an interactive dust emissions scheme, and an updated interactive sea salt emissions scheme in the Global Environmental Multiscale model with Atmospheric Chemistry (GEM-AC) supplemented with the M7 aerosol submodel. The aspects of the configuration of GEM-AC and M7 that are fundamental for this dissertation are outlined in Chapter 3. The aerosol optical property calculation of the M7 aerosol distribution is provided in Chapter 4. Recent parameterisations of dust and sea salt emission that are interactive with the model meteorology are installed in GEM-AC, and are described in Chapter 4. Eight model experiments were performed to document the various new configurations of aerosol representation for the direct aerosol effect in GEM-AC. The eight experiments

and the results are discussed in Chapter 5. This dissertation is concluded in Chapter 6.

# Chapter 2

## Motivation

### 2.1 Objectives

The objectives of this dissertation were:

- Equip GEM-AC with the aerosol direct effect.
- Equip GEM-AC with a dust emission routine that relies on the model meteorology.
- Equip GEM-AC with a new sea salt emission routine that encapsulates ocean wave state as a function of wind speed and sea surface temperature.

Updating the treatment of the aerosol direct effect in GEM-AC requires an understanding of the most fundamental atmospheric radiative effects that aerosols can have, and this basic understanding should not be lost as the capabilities and accuracy of global models increase each year. A simple case of a vertically-dependent, size distributed aerosol affecting the radiative heating and cooling in a cloud-free and chemistry-free atmospheric column is an ideal tool to exhibit the fundamentals behind the aerosol direct effect. In order to accomplish the objectives listed above, a learning tool was developed and assessed. The learning tool was a

column model of atmospheric dust mimicking the atmosphere of Mars in a simplified way.

## 2.2 Motivating Example: A Simple Case of Atmospheric Aerosol Heating and Cooling

A dust column model of the atmosphere of Mars was chosen to explore the potential impacts that a single aerosol species can have in a simplified atmospheric column. The background to previous work on dust modelling in the atmosphere of Mars is given in Appendix A. While the Mars atmosphere is not chemistry and cloud free, it was treated as such in this work for simplicity. The full methodology that was used in building the column model is given in Appendix B with a discussion of the results in Appendix C.

### 2.2.1 The atmospheric column of Mars dust

The column model is depicted in Figure 2.1 with 80 vertical levels ranging from 0 to 80 km in 1 km increments and a log-normal size distribution (Equation B.1) of dust ranging in radius from 0.1 to 5.0  $\mu\text{m}$  with 0.1  $\mu\text{m}$  increment bins. Optical properties are calculated using Mie scattering at 126 wavelengths within the range 0.2 to 200.0  $\mu\text{m}$  and then integrated over two shortwave bands (0.2 to 0.5  $\mu\text{m}$ , 0.5 to 5.0  $\mu\text{m}$ ) and three longwave bands (5.0 to 11.5  $\mu\text{m}$ , 11.5 to 20.0  $\mu\text{m}$ , 20.0 to 200.0  $\mu\text{m}$ ) (Appendix section B.2.1). Each layer is treated as homogeneous. The radiative fluxes are calculated using two-stream quadrature in the shortwave and a two- and four-stream combination quadrature in the longwave. As described by Toon et al. (1989), the adding and doubling method is applied to form a set of radiative transfer equations for 80 homogeneous dust layers for upward and downward fluxes at each interface

level and for each of the five wavelength bands. The set of linear equations is solved by taking advantage of triangular matrix properties of the set of equations. The shortwave and longwave radiative transfer parameterisations are presented in Section B.3.

### **2.2.2 Mars dust aerosol radiative heating and cooling in the column model**

The basic responses of the direct aerosol effect of dust to both the dust vertical distribution and the dust size distribution are presented. This motivational study identifies the basic impact of:

- the effective radius and effective variance of the size distribution in addition to the ground temperature and infrared surface emissivity,
- a linearly decreasing effective radius and effective variance,
- the difference between a single-size dust particle and a size distribution of dust particles, and
- the ground and dust configurations under nighttime temperature conditions to heating within both an upper level dust maximum (ULDM) and a classic vertical distribution in which the number distribution monotonically increases with height (Conrath profile).

For the development of global climate models (GCMs), these results could be useful in assessing errors due to assumptions in atmospheric dust heating.

The potential differences in the vertical profile of atmospheric heating to various size and vertical distributions of dust are presented and discussed in Appendix C and the main results are highlighted here. Interactive dust properties (size distributed dust aerosol dependent on

model meteorology) must be represented accurately in GCMs. To keep in mind the radiative effect difference between a concentration of single-size dust particles and a size distribution of dust particles, the respective atmospheric heating rates are compared. For the size distribution parameter range explored here, atmospheric heating rates from dust aerosol tend to be more sensitive to the effective radius of the distribution and less sensitive to the effective variance. The strong sensitivity of the heating rates to the effective radius is further noted by the dramatic decrease in upper layer heating using a linearly decreasing effective radius with height as opposed to a constant  $R_{eff}$ . Physically, and in GCMs, a decreasing  $R_{eff}$  with height could be caused by sedimentation of the dust or enhanced sedimentation by the formation of ice crystals. Also pertaining to the vertical distribution is that the higher in altitude an ULDM, the higher in altitude and larger in magnitude the peak heating rate. Furthermore, the nighttime effects of the size distribution parameters are smaller than the daytime effects, but the ground temperature has a stronger influence on the nighttime atmospheric heating rates than during the daytime.

### **2.2.3 Significance of the results for atmospheric aerosol effects in Earth's atmosphere**

The results accentuate the atmospheric heating rate sensitivities that can exist in a simplified case of a vertically-distributed size distribution of a single aerosol species. Yu and Zhang (2011) show that aerosol optical properties are very sensitive to the aerosol size distribution as well as to the representative refractive indices. Despite the complexity, the inclusion of aerosol microphysics is essential in climate models, as exemplified in Chapter 1. The presentation of the radiative effects of a size bin distributed single-specied aerosol in a one-dimensional column motivates the need to include the radiative effects of modal distributions of multiple aerosol species in the three-dimensional Global Environment Multiscale

model with Atmospheric Chemistry (GEM-AC). The direct effect of the dust aerosol in a simplified column model provides a simple picture of the sensitivities and issues that could be involved in the aerosol direct effect in GEM-AC).

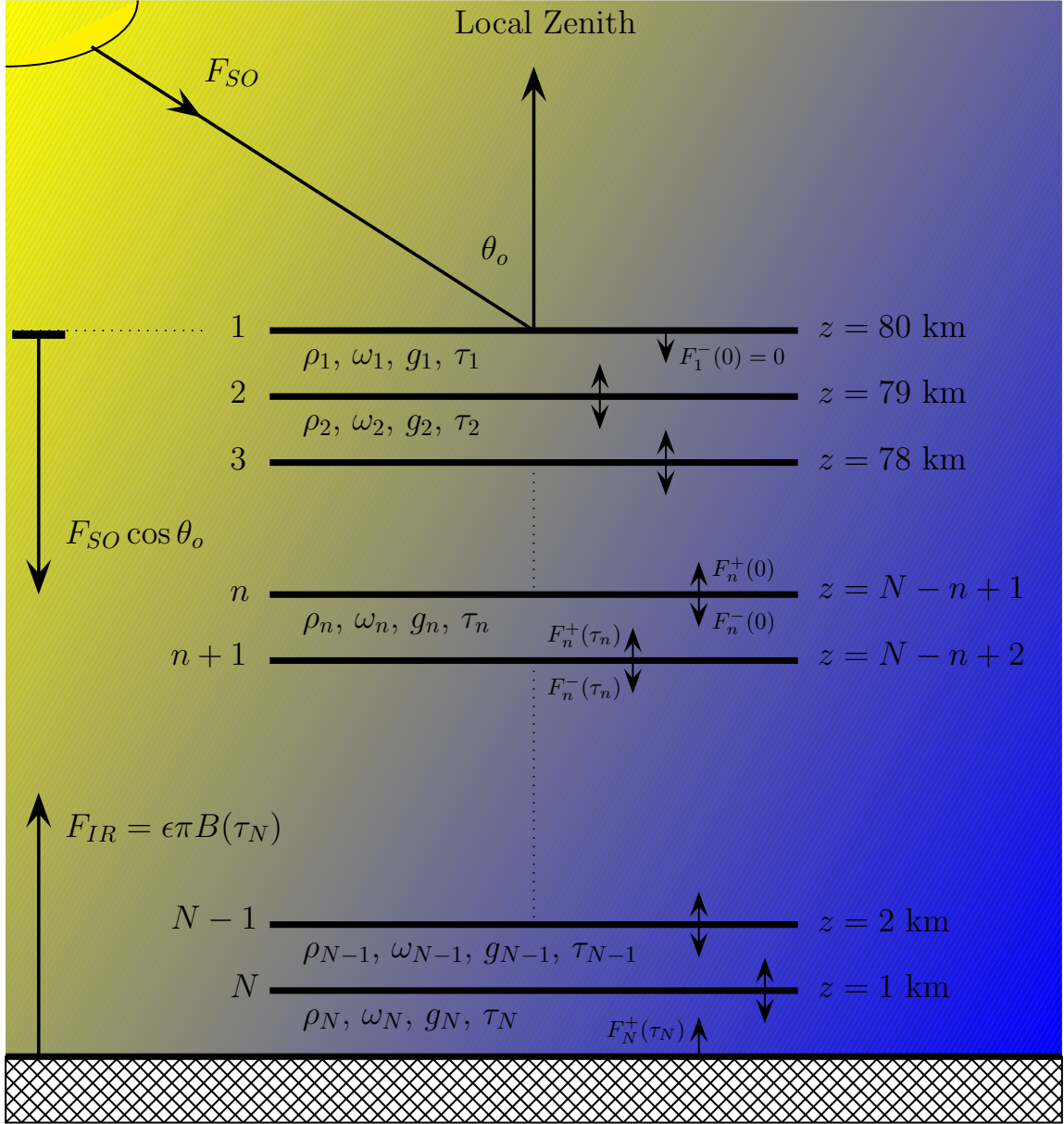


Figure 2.1. The  $N = 80$  defined dust layers in the Martian dust column. Also shown are the upward ( $F^+$ ) and downward ( $F^-$ ) emergent fluxes from each layer ( $n$ ) and the solar ( $F_{SO}$ ) and thermal infrared ( $F_{IR}$ ) source fluxes. Each dust layer has a background atmospheric density ( $\rho$ ), single-scattering albedo ( $\omega$ ), asymmetry parameter ( $g$ ), optical thickness ( $\tau$ ), and total dust number density ( $N_t$ ).

# Chapter 3

## Model Configuration

The Global Environmental Multiscale model with Atmospheric Chemistry (GEM-AC) is a chemical weather model with interactive free tropospheric and stratospheric chemistry, and air quality processes implemented in the GEM model. The GEM model was developed by the Meteorological Service of Canada for operational weather forecasting. GEM-AC is the second generation version of the Global Environmental Multiscale model with Air Quality (GEM-AQ; Kaminski et al. (2008)). Without the direct aerosol effect, GEM-AC has been used in upper troposphere/lower stratosphere aviation emission studies over the arctic (Kaminski et al., 2013; Porebska et al., 2015). Evaluation of the GEM-AC gas phase species is presented in Lupu et al. (2013). The aerosol distribution is provided by the M7 aerosol submodel and is described Section 3.3.

### 3.1 GEM-AC Domain

The model domain in this work is global uniform on a  $3^\circ \times 3^\circ$  grid with the vertical extending into the mesosphere ( $\sim 60$  km). Hybrid sigma-pressure coordinates with 70 ver-

tical levels are used in GEM-AC: terrain following sigma levels at the surface transition to pressure levels at the top of the model. Vertical profiles of the zonal averages presented in Chapter 5 are kept in hybrid sigma levels instead of pressure levels. Model simulations were performed November 1, 2011 to December 31, 2012, inclusive. The first two months are model spin-up and are not used in the analysis. Different time steps were set for the model dynamics, physics, and chemistry. Model dynamics and physics advance every 30 minutes, however, the chemistry time step is 1 hour. The model output files that are used in the analysis are generated at 3-hour intervals.

## **3.2 GEM-AC Radiative Transfer**

Radiative transfer in GEM-AC use the schemes in the CCCma Third and Fourth Generation Atmospheric General Circulation Models (versions AGCM3 and AGCM4). Solar radiation is transferred through the atmosphere via the parameterisation by Fouquart and Bonnel (1980) (both AGM3 and AGM4 versions). The transfer of terrestrial radiation is treated by the updated parameterisations in AGM4, which uses the correlated k-distribution method by Li (2002), Li and Barker (2002), and Li and Barker (2005) for gaseous absorption, and treats transfer among cloud structure using the McICA method by Pincus et al. (2003) and Barker et al. (2008).

## **3.3 M7 Size Distribution Configuration**

Aerosols are distributed in GEM-AC using the aerosol submodel M7 (Vignati et al., 2004). M7 is a modal aerosol model designed for efficient coupling with global climate and

atmospheric chemistry models. The five size-resolved aerosol species are sulphate, organic carbon, black carbon, dust, and sea salt. Aerosol water, nitrate, and ammonium are processed in bulk and then redistributed to the soluble modes. Soluble aerosols are size distributed over four log-normal modes and insoluble aerosols are size distributed over three log-normal modes. The size partitioning of aerosol emission (and production) and aerosol transport are described in Section 3.3.2 and 3.3.3.

### 3.3.1 Soluble vs. insoluble aerosols

Aerosol modes 1 to 4 contain soluble aerosol which are treated as internally mixed, while modes 5 to 7 contain insoluble aerosols which are treated as externally mixed. An internally mixed aerosol particle contains a portion of each aerosol type that is allowed in the mode as the aerosol is transported through the model. On the other hand, an externally mixed aerosol particle is 100% of one aerosol type and can be any of the aerosol types that is allowed in a particular transported mode. The general difference between the soluble and insoluble aerosols is presented pictorially in Figure 3.1.

### 3.3.2 Emission modes

The partitioning of aerosol emissions among the four soluble and 3 insoluble modes is shown in Table 3.1. Production of sulphate occurs in the nucleation mode.

Dust, black carbon, and organic carbon emissions are sourced from the AeroCom benchmark emission dataset (Dentener et al., 2006). Black carbon emission is allocated entirely to the insoluble Aitken mode. Organic carbon emission is partitioned into the Aitken modes as 65% soluble and 35% insoluble with an organic matter to organic carbon mass ratio of 1.4%. Following (Wang et al., 2012), dust emission is partitioned as 10% into the insoluble

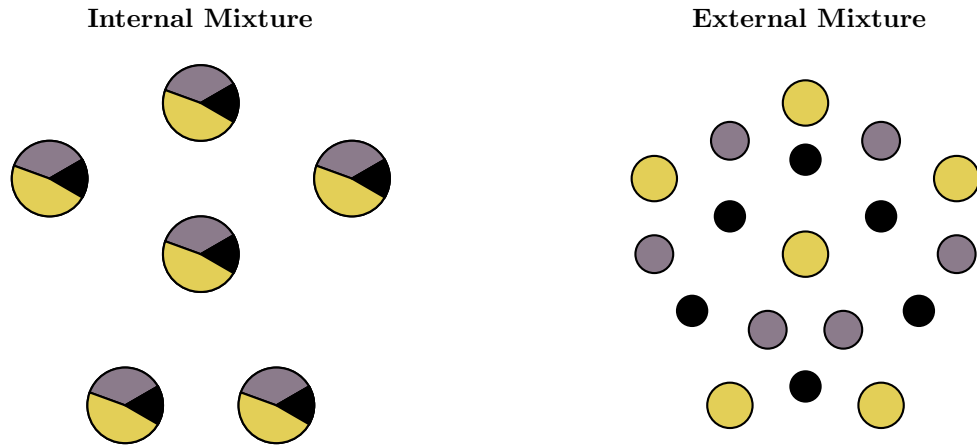


Figure 3.1. A general picture showing the physical difference between internally mixed and externally mixed modes. Each colour represents one distinct aerosol species.

accumulation mode and 90% into the insoluble coarse mode (the AeroCom partitioning of 98.6%/1.4% is considered in the DUCO experiment which is described in Section 5.1).

Sea salt emissions use the M7 scheme, which are wind speed dependent and are sourced from pre-calculated tables of mass concentration and number density fluxes that are based on the work of Monahan et al. (1986) and Smith and Harrison (1998). The emissions distribution follows Guelle et al. (2001), which combines the size distribution results of Monahan et al. (1986) and Smith and Harrison (1998). The emitted sea-salt aerosols are partitioned into the soluble accumulation and coarse modes (Table 3.1).

### 3.3.3 Transported modes

Microphysical and chemical processing in atmospheric transport changes the aerosol number and mass in each mode. The treatment for number and mass transfer in the M7 submodel is described in Vignati et al. (2004). In this dissertation, the allowed partitioning among the modes for transported aerosols is shown in Table 3.2.

Aerosol mode ( $R_P$ in $\mu\text{m}$ )	Emitted Component			
	ASEA	AOC	ABC	ADU
(mode 1) Nucleation ( $R_P < 0.005$ )	-	-	-	-
(modes 2,5) Aitken ( $0.005 < R_P < 0.05$ )	-	S (65%)& NS (35%)	NS (100%)	-
(modes 3,6) Accumulation ( $0.05 < R_P < 0.5$ )	S (variable)	-	-	NS (10%)
(modes 4,7) Coarse ( $R_P > 0.5$ )	S (variable)	-	-	NS (90%)

Table 3.1. M7 size distribution of aerosol emission.  $R_P$  is the aerosol radius. S=soluble and NS=insoluble mean that modes 1 to 4 are soluble and modes 5 to 7 are insoluble. ADU = dust, ABC = black carbon, AOC = organic carbon, and ASEA = sea salt.

Aerosol mode ( $R_P$ in $\mu\text{m}$ )	Transported Component				
	ASEA	ASO <sub>4</sub>	AOC	ABC	ADU
(mode 1) Nucleation ( $R_P < 0.005$ )	-	S	-	-	-
(modes 2,5) Aitken ( $0.005 < R_P < 0.05$ )	-	S	S & NS	S & NS	-
(modes 3,6) Accumulation ( $0.05 < R_P < 0.5$ )	S	S	S	S	S & NS
(modes 4,7) Coarse ( $R_P > 0.5$ )	S	S	S	S	S & NS

Table 3.2. Species are transported in each mode as shown. Modes 1-4 are soluble and modes 5-7 are insoluble. ADU = dust, ABC = black carbon, AOC = organic carbon, and ASEA = sea salt.

# Chapter 4

## Extensions to the GEM-AC Model

### 4.1 Aerosol Optical Property Calculations

#### 4.1.1 Logistics

Equipping GEM-AC with the aerosol direct effect requires calculation of the aerosol optical properties. The aerosol optical properties of the M7 aerosol size distribution must be calculated at each time step in the physics module and input into the radiative transfer subroutines. However, the optical property calculation requires chemical fields from the chemistry module which is called after the physics module. Thus, the aerosol optical property calculation begins at the second timestep.

#### 4.1.2 Method overview

The aerosol optical properties of the entire M7 distribution at each time step, horizontal position, vertical level, and spectral band is required as input into the radiative transfer routine described in Section 3.2. The aerosol optical properties of each of the seven aerosol

modes are calculated using three-dimensional optical property look-up tables according to the methods in Sections 4.1.5 and 4.1.6. The aerosol extinction optical depth, absorption optical depth, single-scattering albedo, and asymmetry parameter is generated following the method in Section 4.1.7. To incorporate the aerosol optical properties into the model, the following subroutines were added:

- `aerooptpro_m7.cdk90`
- `aerooptpro_m7_param.cdk90`
- `aeroopt_param.cdk`
- `aeroopt_read.cdk`

and the following subroutines were modified to either include the new subroutines or test the experiments described in Section 5.1:

- `mod_cccmarad.ftn` (originally `cccmarad.ftn`)
- `mod_raddriv.ftn` (originally `raddriv.ftn`)
- `phy_exe_mod.ftn` (originally `phy_exe.ftn`)
- `cc_nml_vars.cdk`
- `cc_nml.cdk`
- `itf_phy_exe.ftn`
- `itf_phy_slb.ftn`
- `phy_ini.ftn`
- `phybus.cdk`

- options.cdk
- ac1\_chemexe1.ftn90
- ac1\_aerosol\_emis\_sfc\_apply.ftn

### 4.1.3 Optical property input tables

Extinction efficiency ( $Q_{ext}$ ), absorption efficiency ( $Q_{abs}$ ), and asymmetry parameter ( $g$ ) data files are created *a priori* and are called as input during model entry. Each input file acts as a look-up table and consists of 60 matrices with 36 columns and 40 rows, which represent 60 size parameter bins, 36 real refractive index bins, and 40 imaginary refractive index bins. Table 4.1 gives the size parameter bins and the refractive index bins. The three files ( $Q_{ext}$ ,  $Q_{abs}$ , and  $g$  files) containing the three-dimensional look-up tables were generated by inputting the size parameter and refractive index bin vectors in Table 4.1 into the Mie-scattering code described in Section B.2.1.

### 4.1.4 Radiative properties of soluble vs. insoluble aerosols

The difference between the radiative absorption by a population of externally mixed aerosols and internally mixed aerosols is shown in Figure 4.1. In the external mixture, some particles are strong absorbers and some particles are weak absorbers. In the internal mixture, some of the strongly absorbing species is in each aerosol particle which makes the absorption cross-section of the internally mixed particles larger than in the external mixture. This strength of the absorption cross-section in soluble aerosol modes is central to the difference between the volume fraction mixing method and the Bruggeman mixing method discussed in Section 4.1.5. The method to calculate the optical properties in each of the internally mixed

Bin	$x$	$n$	$k$	Bin	$x$	$n$	$k$	Bin	$x$	$n$	$k$
1	0.001	1.05	1.0e-5	21	3.8	2.05	0.85	41	7.8	-	-
2	0.005	1.10	1.0e-4	22	4.0	2.10	0.90	42	8.0	-	-
3	0.01	1.15	1.0e-3	23	4.2	2.15	0.95	43	8.2	-	-
4	0.05	1.20	0.010	24	4.4	2.20	1.00	44	8.4	-	-
5	0.1	1.25	0.050	25	4.6	2.25	1.05	45	8.6	-	-
6	0.5	1.30	0.10	26	4.8	2.30	1.10	46	8.8	-	-
7	1.0	1.35	0.15	27	5.0	2.35	1.15	47	9.0	-	-
8	1.2	1.40	0.20	28	5.2	2.40	1.20	48	9.2	-	-
9	1.4	1.45	0.25	29	5.4	2.45	1.25	49	9.4	-	-
10	1.6	1.50	0.30	30	5.6	2.50	1.30	50	9.6	-	-
11	1.8	1.55	0.35	31	5.8	2.55	1.35	51	9.8	-	-
12	2.0	1.60	0.40	32	6.0	2.60	1.40	52	10	-	-
13	2.2	1.65	0.45	33	6.2	2.65	1.45	53	12	-	-
14	2.4	1.70	0.50	34	6.4	2.70	1.50	54	14	-	-
15	2.6	1.75	0.55	35	6.6	2.75	1.55	55	16	-	-
16	2.8	1.80	0.60	36	6.8	2.80	1.60	56	18	-	-
17	3.0	1.85	0.65	37	7.0	-	1.65	57	20	-	-
18	3.2	1.90	0.70	38	7.2	-	1.70	58	25	-	-
19	3.4	1.95	0.75	39	7.4	-	1.75	59	30	-	-
20	3.6	2.00	0.80	40	7.6	-	1.80	60	40	-	-

Table 4.1. Size parameter ( $x$ ), real refractive index ( $n$ ), and imaginary refractive index ( $k$ ) bins used to generate the three-dimensional optical property input tables.

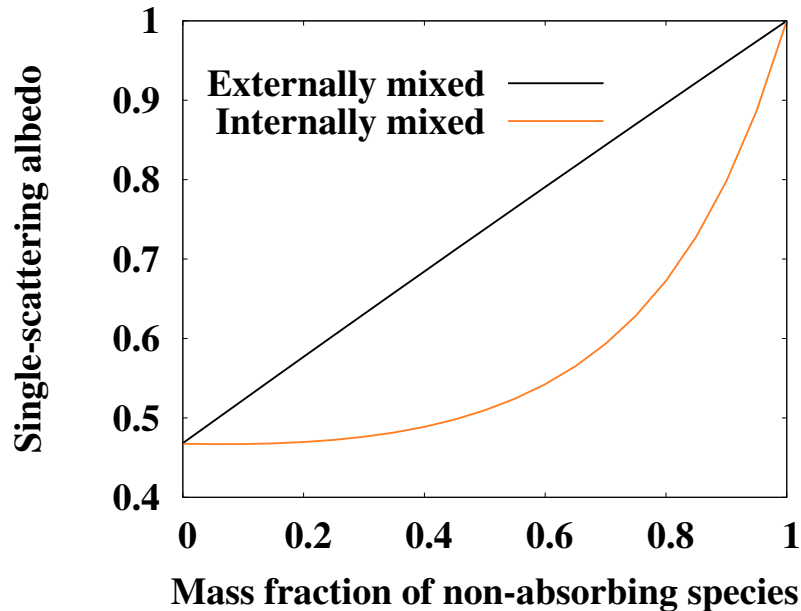


Figure 4.1. Single-scattering albedo of an internal aerosol mixture versus an external aerosol mixture. The mass fraction of aerosol is conserved between the two mixing states. Each mixture is composed of a strongly absorbing aerosol with refractive index  $n = 1.9 - 0.66i$  and a weakly absorbing aerosol with refractive index  $n = 1.53 - 10^{-5}i$ .

modes (modes 1 to 4) is different than the method to calculate the optical properties in the externally mixed modes (modes 5 to 7). The two methods are illustrated in the following sections.

#### 4.1.5 Internally mixed aerosols

Calculation of the aerosol optical properties in the internally mixed modes requires knowledge of the refractive index of each mode. Two methods are used: the volume fraction mixing method which is not computationally intensive and the Bruggeman mixing method which is more computationally intensive. The volume fraction mixing method tends to overestimate absorption when there is a strongly absorbing material, for example, black carbon solubly mixed with lesser absorbing material such as sulphate (Stier et al., 2007). The wavelength dependent refractive indices are listed in Table 4.2.

## Volume fraction mixing

Volume fraction mixing efficiently calculates the refractive index of the internally mixed aerosol modes. The volume fraction of each aerosol species  $j$  in each aerosol mode  $k$  is:

$$v_{j,k} = \frac{m_{j,k}/\rho_j}{m_k/\rho_k} \quad (4.1)$$

where  $m_{j,k}$  is the mass of aerosol species  $j$  in aerosol mode  $k$ ,  $\rho_j$  is the density of each aerosol species  $j$ , and  $m_k$  and  $\rho_k$  are the (total) mass and density, respectively, of the aerosols in mode  $k$ . The volume fraction weighted refractive index of modes  $k = 1, \dots, 4$  is then:

$$r_k = \sum_{j=1}^{N_k} v_{j,k} r_j \quad (4.2)$$

where a  $N_k$  is the number of aerosol species in mode  $k$  and  $r_j = n_j - ik_j$  is the complex refractive index of aerosol species  $j$  with  $n_j$  and  $k_j$  being the real and imaginary parts, respectively.

## Bruggeman mixing

The Bruggeman mixing method to estimate the aerosol refractive index of soluble modes is less efficient but more accurate than the volume mixing method. The importance of accuracy is highlighted in Yu and Zhang (2011) who show that the aerosol optical properties can be very sensitive to the refractive index. Stier et al. (2007) find that when a strongly absorbing aerosol is embedded with a lesser absorbing material, the volume fraction mixing method overestimates absorption and so recommend employing the Bruggeman mixing method.

In each soluble mode  $k$ , there is a total of  $N_k$  aerosol particles each having a volume fraction  $v_{j,k}$ , and complex dielectric constant  $\varepsilon_j = (n_j^2 - k_j^2) + i(2n_jk_j)$  where  $n_j$  and  $k_j$  are respectively the real and imaginary refractive indices of species  $j$ . If in modes  $k = 1, \dots, 4$ ,

these  $j$  types of aerosol are embedded in a host medium having a dielectric constant of  $\varepsilon_{0,k}$ , the general mixing rule is then:

$$\left( \frac{\varepsilon_{eff} - \varepsilon_0}{\varepsilon_{eff} + 2\varepsilon_0} \right)_k = \sum_{j=1}^{N_k} v_{j,k} \left( \frac{\varepsilon_j - \varepsilon_0}{\varepsilon_j + 2\varepsilon_0} \right)_k. \quad (4.3)$$

In the Bruggeman mixing scheme, there is assumed to be no host medium. All  $j$  aerosol species are assumed to be embedded in a medium having an effective dielectric constant  $\varepsilon_{eff}$ . The square root of this effective dielectric constant is the aerosol refractive index of the internally mixed aerosol modes. Following Stier et al. (2007) the general mixing rule becomes

$$f(\varepsilon_{j,k}) = \sum_{j=1}^{N_k} v_{j,k} \frac{\varepsilon_{j,k} - \varepsilon_{eff,k}}{\varepsilon_{j,k} + 2\varepsilon_{eff,k}} = 0 \quad (4.4)$$

in which its solution results from Newton iteration:

$$\varepsilon_{eff,k}^{\nu+1} = \varepsilon_{eff,k}^{\nu} - \frac{f(\varepsilon_{eff,k}^{\nu})}{f'(\varepsilon_{eff,k}^{\nu})} \quad (4.5)$$

where

$$f'(\varepsilon_{eff,k}) = \sum_{j=1}^{N_k} \frac{-3\varepsilon_{j,k}v_{j,k}}{(\varepsilon_{j,k} + 2\varepsilon_{eff,k})^2}. \quad (4.6)$$

The initialisation of the iteration in each mode  $k$  is  $\varepsilon_{eff,k}^0 = 1 + i$ . Convergence was reached at each global model gridpoint in Stier et al. (2007) after seven iterations and thus the maximum number of iterations is set as  $\nu_{max} = 7$ . In GEM-AC, the iteration stops if convergence is reached before  $\nu_{max}$ . The refractive index of modes  $k = 1, \dots, 4$  is  $r_k = \sqrt{\varepsilon_{eff,k}}$  upon convergence.

## Optical properties

The aerosol optical properties of each soluble mode is inferred from the look-up tables described in Section 4.1.3. Using the look-up table requires knowledge of the size parameter of each soluble mode. The effective size parameter is  $x = 2\pi r_k/\lambda$ , where  $r_k$  is the effective radius of mode  $k$ , and  $\lambda$  is a representative wavelength of the particular spectral band (see Table 4.2). After the refractive index of each of the four internally mixed modes is found using either the volume fraction or the Bruggeman mixing method, the aerosol extinction efficiency ( $Q_{ext}^k$ ), absorption efficiency ( $Q_{abs}^k$ ), and asymmetry parameter ( $g_k$ ) are inferred from the look-up tables. The optical depth of each mode containing  $N_k$  particles is then:

$$\tau_{ext,abs,sca}^k = \int_z^\infty Q_{ext,abs,sca}^k \pi r_k^2 N_k dz \quad (4.7)$$

### 4.1.6 Externally mixed aerosols

In the externally mixed aerosol modes ( $k = 5, 6, 7$ ), each aerosol particle is composed of one aerosol species and is assumed to have a radius equal to the effective radius of the mode. As in the internally mixed modes, the size parameter of each aerosol is constant over each aerosol mode:  $x = 2\pi r_k/\lambda$  with  $r_k$  being the effective radius of mode  $k$ . Knowing the refractive index of each species (Table 4.2), the aerosol extinction efficiency ( $Q_{ext}^{j,k}$ ), absorption efficiency ( $Q_{abs}^{j,k}$ ), and asymmetry parameter ( $g_{j,k}$ ) of each species  $j$  in each mode  $k$  are inferred from the look-up tables. The extinction and absorption optical depths of each species  $j$  in each mode  $k$  is:

$$\tau_{ext,abs}^{j,k} = \int_z^\infty Q_{ext,abs}^{j,k} \pi r_k^2 N_{j,k} dz \quad (4.8)$$

and the scattering optical depth is  $\tau_{sca}^{j,k} = \tau_{ext}^{j,k} - \tau_{abs}^{j,k}$ . The total number of aerosol particles of

species  $j$  in mode  $k$  is  $N_{j,k}$  and as mentioned above each aerosol particle in mode  $k$  is assumed to have a radius  $r_k$  equal to the effective radius which is input from the M7 distribution. The optical depth of each mode  $k$  is then just the sum over the optical depths of the species:

$$\tau_{ext,abs,sca}^k = \sum_{j=1}^{N_k} \tau_{ext,abs,sca}^{j,k} \quad (4.9)$$

where  $N_k$  is the total number of species in each mode  $k$ . The asymmetry parameter of mode  $k$  is a weighted mean using the scattering optical depth:

$$g_k = \frac{\sum_{j=1}^{N_k} g_{j,k} \tau_{sca}^{j,k}}{\tau_{sca}^k} \quad (4.10)$$

#### 4.1.7 Optical properties of the M7 distribution

The aerosol extinction, absorption, and scattering optical depths for the entire M7 distribution is the sum of each respective optical depth over the seven modes:

$$\tau_{ext,abs,sca} = \sum_{k=1}^7 \tau_{ext,abs,sca}^k \quad (4.11)$$

The aerosol single-scattering albedo of the distribution is the ratio of the scattering optical depth to the extinction optical depth:

$$\omega = \frac{\tau_{sca}}{\tau_{ext}} \quad (4.12)$$

and the aerosol asymmetry parameter is a weighted mean using the scattering optical depth:

$$g = \frac{\sum_{k=1}^7 g_k \tau_{sca}^k}{\tau_{sca}} \quad (4.13)$$

## **Caveat**

In this work,  $Q_{ext}^k$ ,  $Q_{abs}^k$ , and  $g$  are found from the look-up tables using only a single wavelength representing each spectral band. Taking a weighted averaged over the spectral band would increase accuracy in the optical properties, but also increase computational time. The sensitivity of the aerosol optical property calculation to the difference between the single-wavelength and spectrally averaged approach using the optical property look-up tables was not investigated in this research.

Wavelength Band ( $\mu\text{m}$ )	Aerosol Species							
	ADU	ABC	AOC	ASEA	ASO <sub>4</sub>	AH <sub>2</sub> O	ANH <sub>4</sub>	ANO <sub>3</sub>
0.2 to 0.689 $\lambda = 0.55$	$1.52 - 0.01i$	$1.95 - 0.79i$	$1.53 - 0.006i$	$1.5 - 10^{-8}i$	$1.54 - 10^{-7}i$	$1.333 - 1.96^{-8}i$	$1.54 - 10^{-7}i$	$1.56 - 10^{-9}i$
0.689 to 1.19 $\lambda = 0.86$	$1.5 - 0.008i$	$1.95 - 0.79i$	$1.52 - 0.01i$	$1.48 - 3 \times 10^{-6}i$	$1.52 - 10^{-7}i$	$1.328 - 4.86^{-7}i$	$1.52 - 10^{-7}i$	$1.55 - 10^{-9}i$
1.19 to 2.38 $\lambda = 2.0$	$1.48 - 0.008i$	$1.95 - 0.79i$	$1.42 - 0.08i$	$1.45 - 10^{-3}i$	$1.46 - 10^{-4}i$	$1.306 - 0.0011i$	$1.46 - 10^{-4}i$	$1.53 - 0.001i$
2.38 to 4.545 $\lambda = 3.5$	$1.5 - 0.055i$	$1.95 - 0.79i$	$1.8 - 0.4i$	$1.48 - 1.6 \times 10^{-3}i$	$1.6 - 0.1i$	$1.4 - 0.094i$	$1.6 - 0.1i$	$1.6 - 0.01i$
4.0 to 4.545 $\lambda = 4.5$	$1.52 - 0.05165i$	$2.3 - 0.79i$	$1.7 - 0.2i$	$1.49 - 1.4 \times 10^{-3}i$	$1.5 - 0.005i$	$1.332 - 0.0134i$	$1.5 - 0.005i$	$1.54 - 0.01i$
4.545 to 5.263 $\lambda = 5.0$	$1.555 - 0.056i$	$2.3 - 1.0i$	$1.5 - 0.1i$	$1.47 - 2.5 \times 10^{-3}i$	$1.46 - 0.004i$	$1.325 - 0.0124i$	$1.46 - 0.004i$	$1.54 - 0.01i$
5.263 to 7.142 $\lambda = 6.2$	$1.44 - 0.131i$	$2.3 - 1.0i$	$1.7 - 0.05i$	$1.6 - 2.2 \times 10^{-2}i$	$1.3 - 0.02i$	$1.363 - 0.088i$	$1.3 - 0.02i$	$1.6 - 0.032i$
7.142 to 9.09 $\lambda = 8.2$	$1.05 - 0.397i$	$2.3 - 1.0i$	$1.8 - 0.1i$	$1.42 - 0.02i$	$1.0 - 0.1i$	$1.286 - 0.0351i$	$1.0 - 0.1i$	$1.5 - 0.022i$
9.09 to 10.204 $\lambda = 9.5$	$2.6 - 0.616i$	$2.1 - 1.0i$	$1.4 - 0.05i$	$1.58 - 0.018i$	$2.85 - i$	$1.243 - 0.0444i$	$2.85 - i$	$1.45 - 0.028i$
10.204 to 12.5 $\lambda = 11.5$	$1.8 - 0.1i$	$2.1 - 1.0i$	$1.4 - 0.02i$	$1.48 - 0.014i$	$1.8 - 0.013i$	$1.12 - 0.114i$	$1.8 - 0.013i$	$1.3 - 0.1i$
12.5 to 18.518 $\lambda = 16.4$	$1.65 - 0.228i$	$2.0 - 1.0i$	$1.4 - 0.008i$	$1.56 - 0.09i$	$2.8 - i$	$1.346 - 0.427i$	$2.8 - i$	$1.6 - 0.87i$
18.518 to 29.411 $\lambda = 25.0$	$2.6 - 0.7i$	$2.0 - 1.0i$	$1.4 - 0.004i$	$1.76 - 0.205i$	$1.5 - 0.025i$	$1.531 - 0.356i$	$1.5 - 0.025i$	$1.75 - 0.87i$
29.411 to $\infty$ $\lambda = 35.0$	$2.3 - 0.65i$	$2.0 - 1.0i$	$1.4 - 0.003i$	$1.76 - 0.5i$	$1.5 - 0.1i$	$1.532 - 0.336i$	$1.5 - 0.1i$	$2.3 - 0.32i$

Table 4.2. Wavelength dependent refractive indices of the eight aerosol species used in the aerosol radiative computations in GEM-AC. The first four wavelengths bands are solar and the last nine are thermal. Computation of the size parameter in the refractive index routines requires a representative wavelength of each band; the representative wavelength that is used in the computations is provided below each band. ADU = dust, ABC = black carbon, AOC = organic carbon, and ASEA = sea-salt. The refractive indices of ADU are from Krekov (1993); AOC are from Stier et al. (2007); ASEA are from HITRAN; ASO<sub>4</sub>, ANH<sub>4</sub>, and ANO<sub>3</sub> are from GACP; AH<sub>2</sub>O are from D’Almeida et al. (1991). ABC refractive indices are from Bond and Bergstrom (2006) in the solar spectrum and from Stier et al. (2007) in the thermal spectrum. Note that the refractive indices of ANH<sub>4</sub> are assumed to equal those of ASO<sub>4</sub>.

## 4.2 Interactive Dust Aerosol Emissions

The dust emissions routine in GEM-AC was updated to include a choice between using the benchmark AeroCom dust emission dataset and a new interactive dust emission scheme. The **ldu** flag in *ac1\_chemexe1.ftn90* is **.true.** for interactive dust and **.false.** for AeroCom dust emissions. The interactive dust routine described in this section is incorporated into the *aerooptpro-m7.cdk* subroutine.

The interactive routine is presented in this section and is largely based on Zender et al. (2003). Mass emission fluxes of dust at each time step and in each grid cell are calculated using the model state variables in GEM-AC: the fractional coverages of ocean, lakes, swamps, snow, ice, and vegetation, the soil moisture, the minimum and maximum terrain heights of the surrounding grid cells, and the wind friction speed. The mass emission flux is:

$$F_j = A_1 \alpha B H S \sum_{k=1}^3 m_k M_{j,k} \quad (4.14)$$

where  $A_1 = 7 \times 10^{-4}$ ,  $\alpha$  is the sandblasting efficiency,  $B$  is the fraction of bare soil exposed in a grid cell,  $H$  is the horizontal mass flux,  $S$  is the source erodibility factor, and  $\sum_{k=1}^3 m_k M_{j,k}$  is the mass fraction in each transport mode.

Dust is assumed to be emitted from three log-normally distributed background source modes (D’Almeida, 1987) into eight transport modes and so the distribution that is used is the mass fraction overlap of each source mode  $k$  with each transport mode  $j$  (Schulz et al., 1998). The mass fraction of each transport mode  $i$  is a sum of error functions:

$$M_{j,k} = \frac{1}{2} \left[ \operatorname{erf} \left( \frac{\ln(D_{max,j}/\bar{D}_k)}{\sqrt{2} \ln \sigma_k} \right) - \operatorname{erf} \left( \frac{\ln(D_{min,j}/\bar{D}_k)}{\sqrt{2} \ln \sigma_k} \right) \right] \quad (4.15)$$

where  $m_k$ ,  $\sigma_k$ , and  $\bar{D}_k$  are listed in Table 4.3. The minimum and maximum diameter values of the eight transport bins,  $D_{min}$  and  $D_{max}$ , are listed in Table 4.4. Bins  $j = 1, 2, 3$  are

deposited into the M7 accumulation mode and bins  $j = 4, 5, 6, 7, 8$  are deposited into the M7 coarse mode.

$k$	$\bar{D}_k$ ( $\mu\text{m}$ )	$\sigma_k$	$m_k$
1	0.16	2.1	0.036
2	1.4	1.9	0.957
3	10	1.6	0.007

Table 4.3. Parameters of the three log-normally distributed source modes in D’Almeida (1987). The mass fraction is  $m$ ,  $\bar{D}_k$  is the number median diameter, and  $\sigma_k$  is the geometric standard deviation.

$j$	1	2	3	4	5	6	7	8
$D_{min,j}/D_{max,j}$	0.2/0.36	0.36/0.6	0.6/1.0	1.0/2.0	2.0/3.6	3.6/6.0	6.0/12.0	12.0-20.0

Table 4.4. The bounding diameters of the eight transport bins into which dust is initially emitted.

The sandblasting efficiency is  $\alpha = 10^{(13.4M_{clay}-6)}$  (Marticorena and Bergametti, 1995) with a fixed soil clay fraction of  $M_{clay} = 0.2$  (Zender et al., 2003).

The fraction of bare soil in GEM-AC is taken to be the maximally overlapped product of unvegetated ground under no water, snow or ice cover:

$$B = (1 - B_{water} - B_{lake} - B_{swamp})(1 - B_{snow} - B_{ice})(1 - B_{vegetation}) \quad (4.16)$$

where  $B_{water}$ ,  $B_{lake}$ ,  $B_{swamp}$ , and  $B_{ice}$  are the fractional coverage outputs from GEM-AC. The fractions of ground covered by vegetation and by snow in each grid cell is represented following the methods of Zender et al. (2003). The fraction of vegetation coverage on the ground in each grid cell is  $B_{vegetation} = \min[1.0, \min(LAI, 0.3 \text{ m}^2 \text{ m}^{-2})/0.3 \text{ m}^2 \text{ m}^{-2}]$  where  $LAI$  is the monthly leaf area index and the  $0.3 \text{ m}^2 \text{ m}^{-2}$  value is the threshold for complete suppression of dust emissions. The fraction of snow coverage on the ground in each grid cell

is  $B_{snow} = \min(h/0.05, 1.0)$  where  $h$  is the snow depth ( m) and the 0.05 m value is the snow thickness for 100% snow coverage (complete dust suppression).

The horizontal mass flux is from White (1979):

$$H = \frac{C\rho_{air}u_{\star}^3}{g} \left(1 - \frac{u_{\star t}^2}{u_{\star}^2}\right) \left(1 + \frac{u_{\star t}}{u_{\star}}\right) \quad (4.17)$$

where  $C = 2.61$  is a proportionality constant (Zender et al., 2003),  $g$  is the gravitational acceleration,  $\rho_{air}$  is the air density,  $u_{\star}$  is the GEM-AC wind friction speed and  $u_{\star t}$  is the threshold wind friction speed. Dust is emitted when the wind friction speed is larger than the threshold. The threshold wind friction speed is determined following Spyrou et al. (2010):

$$u_{\star t} = \begin{cases} \frac{0.129A}{(1.928Re_{HF}^{0.092}-1)^{0.5}} & 0.03 < Re_{HF} < 10 \\ 0.12A(1 - 0.0858e^{-0.0617(Re_{HF}-10)}) & Re_{HF} > 10 \end{cases}$$

where  $Re_{HF} = 1331D_0^{1.56} + 0.38$  (Marticorena et al., 1997) is the Reynolds number and  $A = \rho_{dust}gD_0/\rho_{air}$ . The optimal particle size when the threshold wind friction speed is a minimum (and hence when the horizontal mass flux is a maximum) is  $D_0$ . Spyrou et al. (2010) use  $D_0 = 60 \mu\text{m}$  and Iversen and White (1982) use  $D_0 = 75 \mu\text{m}$ . In the DUX1 case  $D_0 = 75 \mu\text{m}$ , and in the DUX2 case  $D_0 = 60 \mu\text{m}$ . The threshold friction velocity increases due to soil moisture. The threshold friction velocity is therefore adusted (Fécan et al., 1999) as:

$$u_{\star t} = \begin{cases} u_{\star t} & W \leq W_{max} \\ u_{\star t} \sqrt{1 + 1.21(W - W_{max})^{0.68}} & W > W_{max} \end{cases}$$

where  $W$  is the soil moisture output from GEM-AC and the maximum amount of moisture contained within the soil depends on the clay fraction:  $W_{max} = 0.14M_{clay}^2 + 0.17M_{clay}$ .

The topographic source erodibility factor ( $S$ ) accounts for dust accumulation in valleys

and basins. This work uses the Ginoux et al. (2001) parameterisation:

$$S = \left( \frac{h_{max} - h}{h_{max} - h_{min}} \right)^5 \quad (4.18)$$

where  $h$  is the height of the grid cell, and  $h_{min,max}$  are the minimum and maximum of the surrounding grid cell heights. Essentially,  $S$  is the probability that accumulated surface sediments are potential dust sediments lifted into a grid cell.

### 4.3 Significant Wave Height Dependent Sea-Salt Aerosol Emissions

The sea-salt emission routine in GEM-AC was updated with an option to use a sea-state dependent emissions parameterisation. The flag for the option (**lss** in *ac1\_chemexe1.f90*) is **.false.** for sea-state dependent emissions and is **.true.** for wind-only dependent emissions. The sea-state dependent sea salt emissions described in the section is incorporated into the *aerooptpro\_m7.cdk* subroutine.

Many global models use number and mass emission fluxes prescribed solely as a function of wind speed such as those by Monahan et al. (1986), Smith and Harrison (1998), Guelle et al. (2001), Gong (2003), and Mårtensson et al. (2003). Emission fluxes as a function of wind speed only can overestimate sea-salt production, particularly in winter with higher wind speeds (de Leeuw et al. (2011)). Ocean waves and strong winds are efficient sea spray emission mechanisms. Sea spray droplets containing sea salt particles and liquid water are torn from the tops of wave crests, are ejected from the splash of spilling wave crests, and ejected by bursting bubbles at the top of whitecapping ocean waves (Andreas et al., 1995). The new sea-salt emission module is based on the parameterisation by Ovadnevaite et al. (2014)

which encapsulates the wave state of the ocean surface and the sea surface temperature, and is used in the SSWV experiment (Section 5.1).

The wave state at the ocean surface can be represented by the significant wave height,  $H_S$ . Ideally, the coupling of a wave model to GEM-AC such as WAM, would provide  $H_S$ , but it can be represented empirically. The empirical relationship given in Mori et al. (2012):

$$H_S = A_2 u_{10}^2 + b \quad (4.19)$$

is used in this work where  $u_{10}$  is the 10-m wind,  $A_2$  is a tuning factor, and  $b$  is a correction for swell height. The wind wave part of the wave state generates the ocean whitecaps, and the bubbles bursting within the whitecaps emit sea-salt particles into the marine boundary layer. The swell part of the wave state is therefore unnecessary and  $b$  is neglected. The  $A_2$  factor is adjusted according to the magnitude of  $u_{10}$ , following (Mori et al., 2012):

$$A_2 = \begin{cases} 0.03 & 10 < u_{10}^2 < 60 \\ 0.0251 & 60 < u_{10}^2 < 120 \\ 0.02 & u_{10}^2 > 120 \end{cases}$$

and if  $u_{10} < 10 \text{ m s}^{-1}$  then the SWIN parameterisation is used.

The size dependent sea salt number density fluxes are listed in Table 4.5. Sea salt is emitted into five size bins and then repartitioned into the M7 size distribution as follows:  $i = 1, 2$  into the M7 Aitken mode,  $i = 3, 4$  into the accumulation mode, and  $i = 5$  into the coarse mode. The Reynolds number is given by

$$Re_{WH} = \frac{C_D^{1/2} u_{10} H_S}{\nu_W}$$

viscosity of sea-water is given by the parameterisation by Riisgård and Larsen (2007) which

is dependent upon the sea surface temperature (SST) output from GEM-AC:

$$SST = 14.332\nu_W^2 - 65.544\nu_W + 73.405.$$

It should be emphasised that the significant wave height parameterisation neglects fetch, which is the distance over which wind exerts stress on the water surface. Developing wind waves are fetch dependent and the parameterised significant wave height by Mori et al. (2012) essentially encompasses seas which are maximally developed for a given fetch, wind speed, and wind duration. Therefore, the new sea-salt emission routine should only be used for longer term model projections.

$i$	$F_i$ ( m <sup>-2</sup> s <sup>-1</sup> )
1	$104.5(Re_{HW} - 10^{-5})^{0.556}$
2	$0.0442(Re_{HW} - 10^{-5})^{1.08}$
3	$149.6(Re_{HW} - 10^{-5})^{0.545}$
4	$2.96(Re_{HW} - 10^{-5})^{0.79}$
5	$0.51(Re_{HW} - 2 \times 10^{-5})^{0.87}$

Table 4.5. Sea salt number density fluxes from Ovadnevaite et al. (2014) in five size bins.

# Chapter 5

## Modelling Scenarios and Discussions

### 5.1 Experiment Descriptions

Eight model experiments were performed to document the various new configurations of aerosol representation for the direct aerosol effect in GEM-AC. The experiments outlined in Table 5.1. Seven of the experiments (denoted as BASE, LONG, VOLF, DUCO, DUX1, DUX2, and SSWV) account for the aerosol direct effect and the remaining experiment (denoted as NOAH) does not. The control experiment is denoted as BASE, which calls the aerosol optical property subroutine (Section 4.1) and subsequently feeds the aerosol optical properties to the CCCma radiative transfer subroutine (Section 3.2). The remaining six experiments (LONG, VOLF, DUCO, DUX1, DUX2, and SSWV) have a single characteristic different from the BASE case.

The modal partitioning of the emitted and transported aerosols in the BASE experiment are shown in Table 3.1 and Table 3.2, and is described in Section 3.3. In the BASE experiment, aerosols are assumed to be solubly mixed via the Bruggeman method (Section 4.1.5), and the soluble and insoluble aerosol optical properties are calculated in four shortwave and one longwave spectral bands as described in Section 4.1.

The other six experiments which call the aerosol optical property subroutine are: LONG, VOLF, DUCO, DUX1, DUX2, and SSWV. These six experiments are identical to the BASE case but with one particular characteristic in the configuration changed. In LONG, the aerosol optical properties are calculated in all nine longwave spectral bands that are defined in GEM-AC (Table 4.2) and are used as input into the CCCma radiation routine (Section 3.2). In VOLF, mixing of the aerosol species in the four soluble aerosol modes is determined using the volume fraction mixing method (Section 4.1.5). In DUCO, dust emissions are given by the AeroCom dataset with 1.4% of the emissions are given to the nonsoluble accumulation mode and 98.6% are given to the nonsoluble coarse mode. In DUX1 and DUX2, the interactive dust subroutine described in Section 4.2 is called instead of the AeroCom emissions. The optimal dust size for saltation mass flux ( $D_0$ ) is set to 75  $\mu\text{m}$  and 60  $\mu\text{m}$  in DUX1 and DUX2, respectively, based on Spyrou et al. (2010) and Iversen and White (1982). In SSWV, sea salt emissions are parameterised with the interactive and sea-state dependent subroutine described in Section 4.3.

Experiment	Description
BASE	Bruggeman mixing; 4 SW + 1 LW spectral bands; AeroCom dust emission with 10%/90% partition, M7 sea salt emission
NOAH	As in BASE but with no aerosol heating effects
LONG	As in BASE but for 9 LW spectral bands
VOLF	As in BASE but for volume fraction mixing method
DUCO	As in BASE but for 1.4%/98.6% partition in dust emission
DUX1	As in BASE but for interactive dust (Section 4.2)
DUX2	As in DUX1 but for $D_0 = 60 \mu\text{m}$
SSWV	As in BASE but for sea-state dependent sea salt emissions (Section 4.3)

Table 5.1. List of experiments. Radiative transfer of solar radiation is in the shortwave bands (SW) and of terrestrial radiation is in the longwave bands (LW) (spectral bands are provided in Table 4.2).

## 5.2 Aerosol Optical Property Distributions

### 5.2.1 Aerosol Extinction Optical Depth

The 10 m distribution of aerosol extinction optical depth is shown in Figure 5.1. Aerosol radiative effects are not calculated in the NOAH case and so do not exist in the figure. Large optical depths are captured over northern Africa, the Middle East, China, eastern North Atlantic and the North Sea, eastern North America, and over the Antarctic Circumpolar current.

The placement of the GEM-AC aerosol optical depth over North Africa is more centered over the continent compared to Stier et al. (2005), Rotstayn et al. (2009), Pringle et al. (2010), and Wang et al. (2011). For example, in Stier et al. (2005) and Rotstayn et al. (2009), the larger aerosol optical depth swath extends from roughly 10W to 40W over the Atlantic Ocean from western Africa. This is also apparent in the comparison of the GEM-AC aerosol optical properties with two AERONET sites in western Africa (Section 5.2.5).

With respect to the BASE experiment, larger optical depths are observed in the LONG experiment over central China and north of Lake Chad in central North Africa. The annual mean column burden of dust is largest over northern Africa, while the column burden of black carbon is largest over China (Pringle et al., 2010). Dust aerosol has a relatively large imaginary refractive index in most of the longwave spectral bands (Table 4.2) which makes it a good absorber of longwave radiation. Likewise, the imaginary refractive index of black carbon aerosol is mostly 1.0 in the longwave. Since dust and black carbon are good absorbers at longer wavelengths, the LONG case captures this extra attenuation in the total aerosol extinction optical depth which is neglected in the other cases.

The zonal average of the aerosol optical depth is provided in Figure 5.2. The zonal average of the aerosol optical depth is generally higher in the SSWV case in the 20°N to 50°N latitudes. Figure 5.1 shows that the new sea-salt emission routine in the SSWV experiment

produces a larger optical depth over the eastern North Atlantic around the British Isles, and over the North Pacific around the Aleutian Islands. The reason for this increase in aerosol optical depth is unclear. In the southern hemisphere between 50°S to 60°S, the zonal average in SSWV is comparable to that in BASE. In fact, the zonal average in DUCO and DUX1 are higher than that in SSWV. This may be the result of the Ovadnevaite et al. (2014) parameterisation modulating the sea spray emission over the Antarctic Circumpolar current which may be overestimated by the SWIN parameterisation in the BASE case due to the consistently high wind speeds (Allison et al., 2010). Sea salt is emitted in the SWIN parameterisation as a function of wind speed only and has been shown to overpredict sea salt emission (de Leeuw et al., 2011) in high wind speeds.

The aerosol optical depths in GEM-AC are comparable to other global models. The spatial placement of the peak in the aerosol optical depth just north of Lake Chad in GEM-AC output is also shown in Liao et al. (2004), Pringle et al. (2010), Peng et al. (2012) and Pozzer et al. (2012). The magnitude of the GEM-AC aerosol optical depth is however 0.5 less than that in Pringle et al. (2010) and 0.3 less than that in Pozzer et al. (2012). Both in Stier et al. (2005) and Rotstayn et al. (2009), the peak aerosol optical depth in northern Africa occurs in the west and extends off the coast and over the Atlantic. As another example, over the eastern United States the GEM-AC aerosol optical depth ranges between 0.08 and 0.1 while Rotstayn et al. (2009) shows that the Australian climate model, CSIRO, gives a range between 0.16 to 0.32 which they show compares well with observations based on AERONET and AeroCom. One region that GEM-AC fails to adequately simulate aerosol optical depth is over India, indicating that at a regional level, aerosol microphysics and emissions need to be further investigated and improved in GEM-AC.

Pringle et al. (2010) and Pozzer et al. (2012) both use the EMAC model with GMXe microphysics, but in one instance results in an overprediction of aerosol optical depth compared to observations and in the other instance, an under prediction. For example, over China the

average aerosol optical depth in Pozzer et al. (2012) during 2005 to 2008 is mostly between 0.5 to 0.8 which is  $\sim 0.4$  larger than the optical depth by MISR and MODIS. Meanwhile, Pringle et al. (2010) underestimate the average aerosol optical depth in 2001: the model optical depth is roughly between 0.2 to 0.4 which is less than  $\sim 0.5$  optical depth given by MODIS. The GISS GCM II' in Liao et al. (2004) simulates aerosol optical depth over China in the range 0.3 to 0.5 although does not provide the simulation time period. The GEM-AC average aerosol optical depth over China is about 0.1 during 2012. Further contrasting the abilities between models, the CAM5 model does not distinguish China as a large aerosol optical depth hotspot (Liu et al., 2012) while the ECHAM5-HAM model simulation by Stier et al. (2005) shows close agreement with observations (MODIS+MISR) over China.

Overall, GEM-AC tends to underestimate aerosol optical depth compared to other global models but does distinguish regions of larger aerosol optical depths.

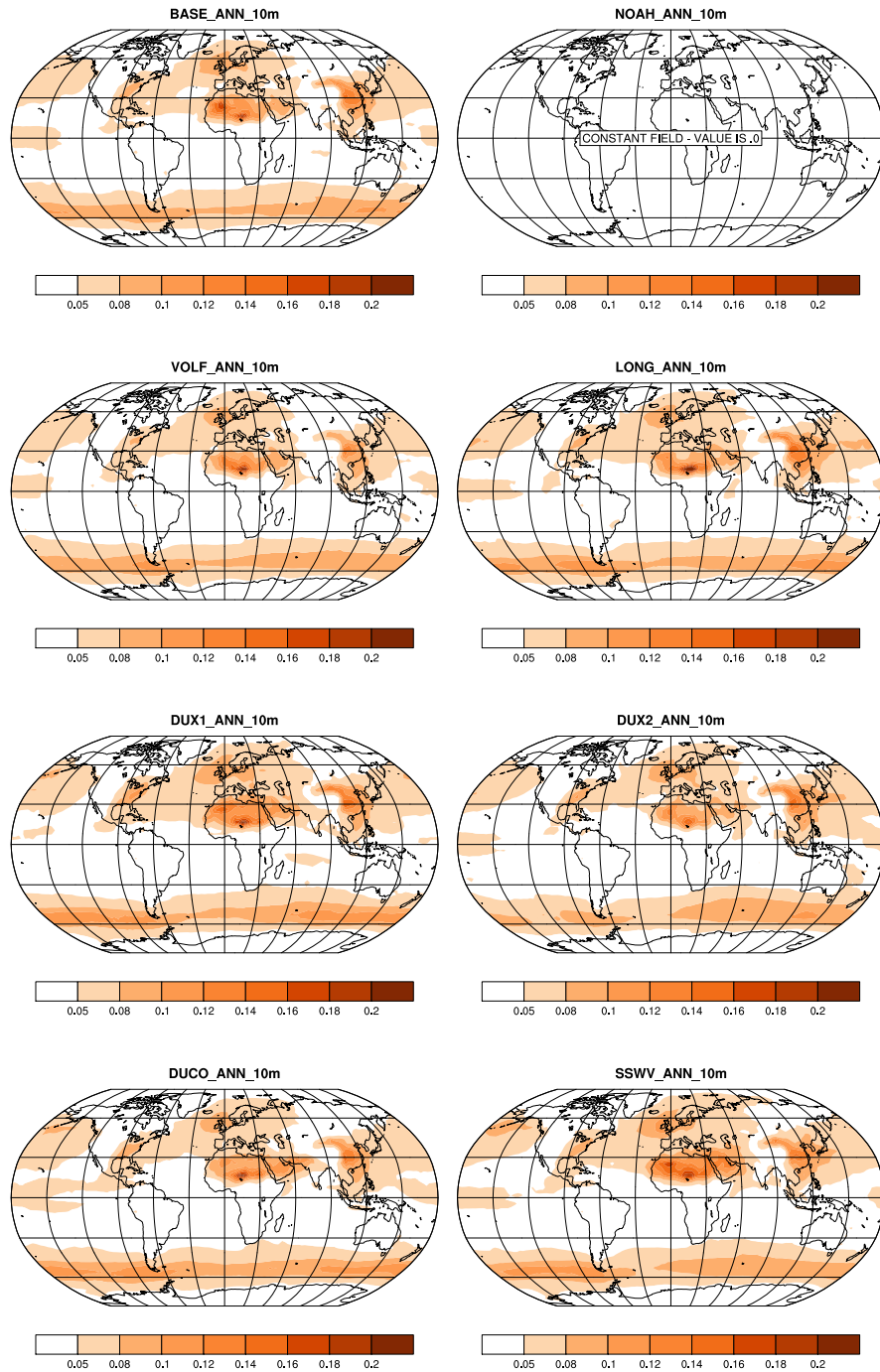


Figure 5.1. 10 m aerosol optical depth averaged over 2012 for BASE, NOAH, VOLF, LONG, DUX1, DUX2, DUCO, and SSWV experiments.

## 5.2.2 Aerosol Absorption Optical Depth

The 10 m aerosol absorption optical depth is shown in Figure 5.3 and the zonal average is shown in Figure 5.4. Aerosol absorption optical depth north of Lake Chad in northern Africa increased roughly 80% in the LONG experiment with respect to the BASE experiment, since dust is a good absorber in most of the longwave spectral bands and is the primary aerosol over this region. Overall, the aerosol absorption optical depth is slightly larger in the northern hemisphere in the SSWV compared to the other seven experiments. The SSWV zonal average of the absorption optical depth in the northern hemisphere is comparable to that in the LONG experiment, however, only 1 longwave spectral band is used in the SSWV experiment. Sea salt has a small imaginary refractive index in the shortwave spectral bands and is not a good absorber (Table 4.2). The solubility of sea salt allows it to easily mix with other aerosol species such as sulphate, ammonium, nitrate, black carbon, organic carbon, and dust which could increase absorption of solar radiation. Black carbon in particular is an efficient absorber in the shortwave and can mix with sea salt in the soluble modes.

In some general regions, the GEM-AC aerosol absorption optical depth is similar to the ECHAM5-HAM aerosol absorption optical depth presented in Stier et al. (2005). In southern China, the aerosol absorption optical depth is about 0.005 to 0.01 in ECHAM5-HAM and in GEM-AC it is about 0.003 to 0.005. In northern China, ECHAM5-HAM absorption optical depth peaks at 0.05 and GEM-AC peaks at 0.01. Similarly in northern Africa, GEM-AC simulates an aerosol absorption optical depth of about 0.01 to 0.02 while in ECHAM5-HAM it is about 0.001 to 0.01. The peak absorption over the African continent in ECHAM5-HAM occurs over the central coast, whereas in GEM-AC the peak coincides with the peak extinction optical depth to the north of Lake Chad.

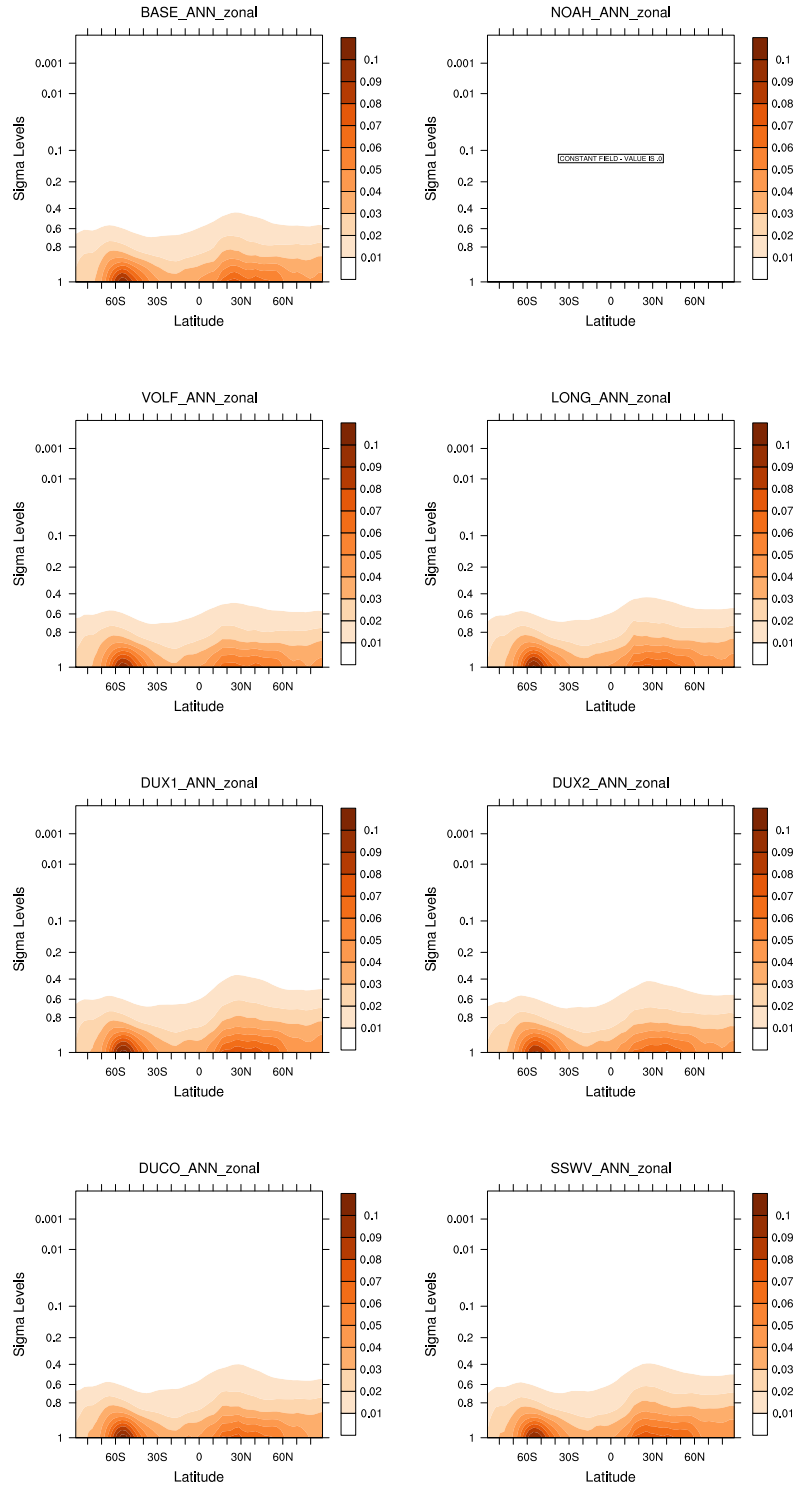


Figure 5.2. 2012 zonally averaged aerosol optical depth for BASE, NOAH, VOLF, LONG, DUX1, DUX2, DUCO, and SSWV experiments.

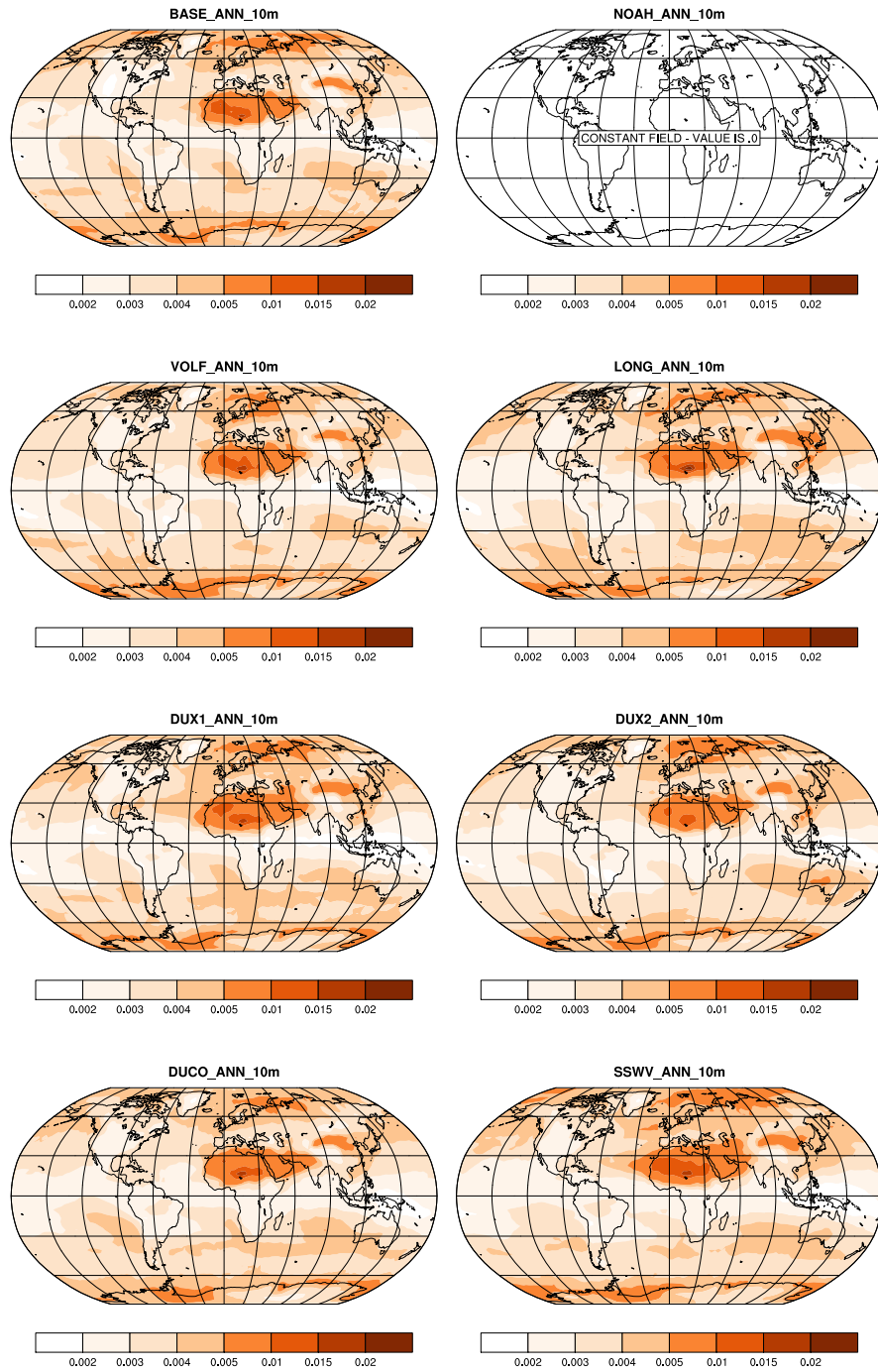


Figure 5.3. 10 m aerosol absorption optical depth averaged over 2012 for BASE, NOAH, VOLF, LONG, DUX1, DUX2, DUCO, and SSWV experiments.

### 5.2.3 Single-scattering Albedo

The 10 m aerosol single-scattering albedo is shown in Figure 5.5 for each of the eight experiments. Zonal averages are provided in Figure 5.6. The GISS GCM II' in (Liao et al., 2004) and the CAM-CCC AGCM III in Ayash et al. (2008) both simulate a similar single-scattering distribution to those produced by GEM-AC.

### 5.2.4 Asymmetry Parameter

Figure 5.7 shows the 10 m distribution of the aerosol asymmetry parameter. The distributions show that smaller variability exists among the eight experiments than among the distributions of the other optical properties. Ayash et al. (2008) shows global distributions over the seasons, where the asymmetry parameter is generally at a minimum of about 0.55 to 0.65 over South America, southern Africa and Australia with higher values generally ranging between 0.65 to 0.75 over the oceans. The GEM-AC asymmetry parameter agrees well with the distributions in Ayash et al. (2008).

The zonal averages of the aerosol asymmetry parameter in Figure 5.8 show the vertical profiles. Forward scattering by aerosols decreases and approaches isotropy at higher model levels.

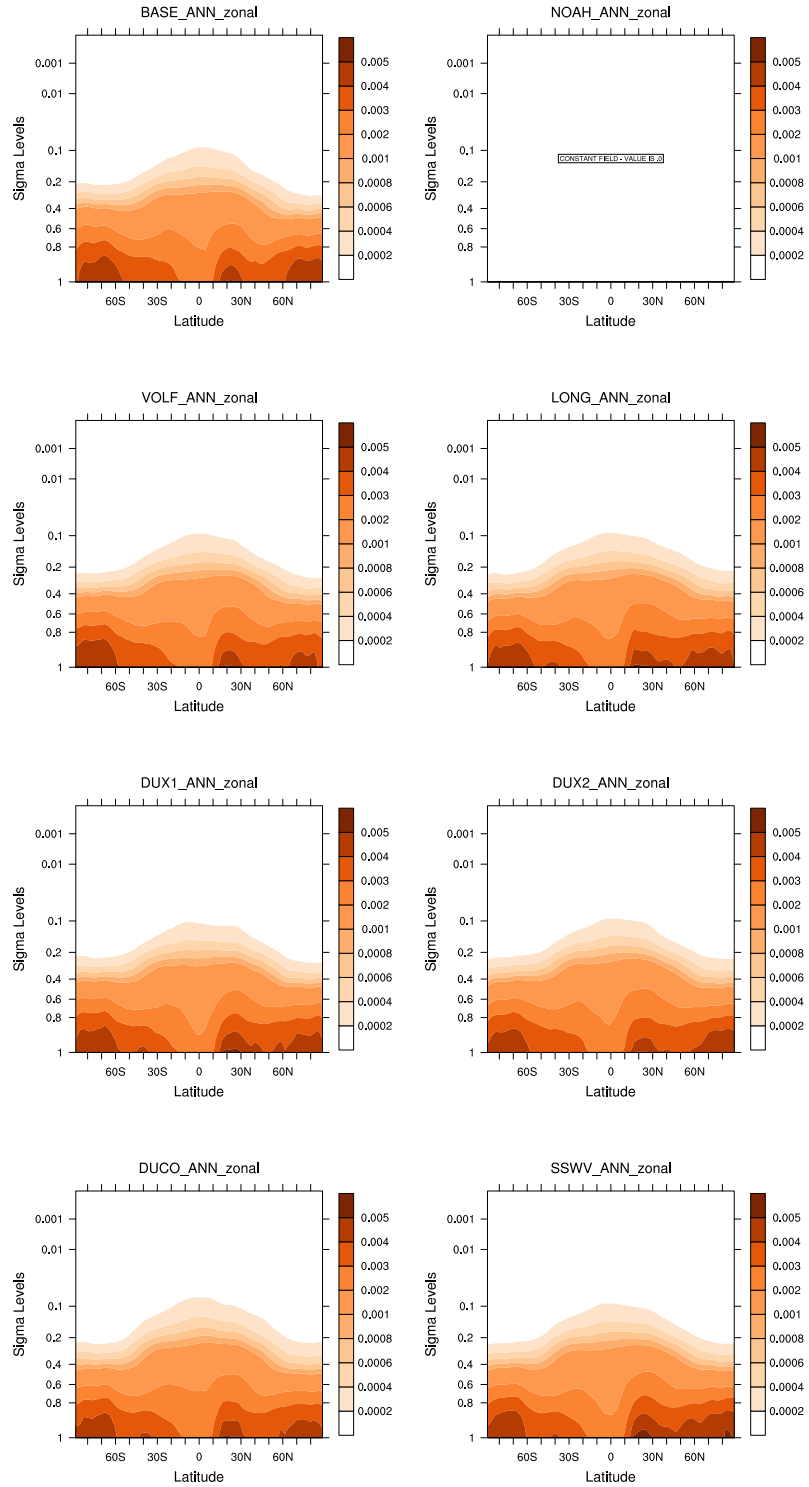


Figure 5.4. 2012 zonally averaged aerosol absorption optical depth for BASE, NOAH, VOLF, LONG, DUX1, DUX2, DUCO, and SSWV experiments.

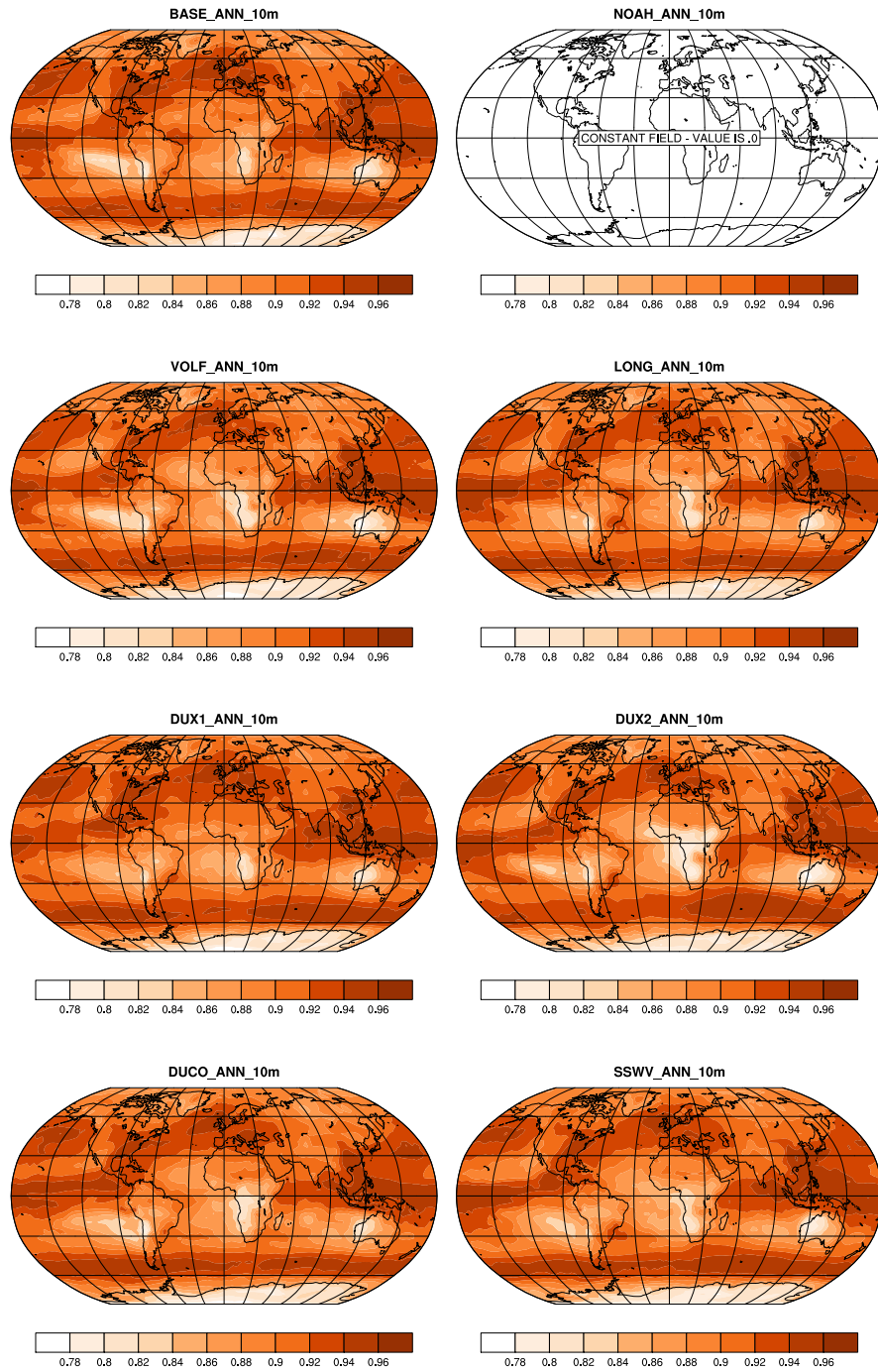


Figure 5.5. 10 m aerosol single-scattering albedo averaged over 2012 for BASE, NOAH, VOLF, LONG, DUX1, DUX2, DUCO, and SSWV experiments.

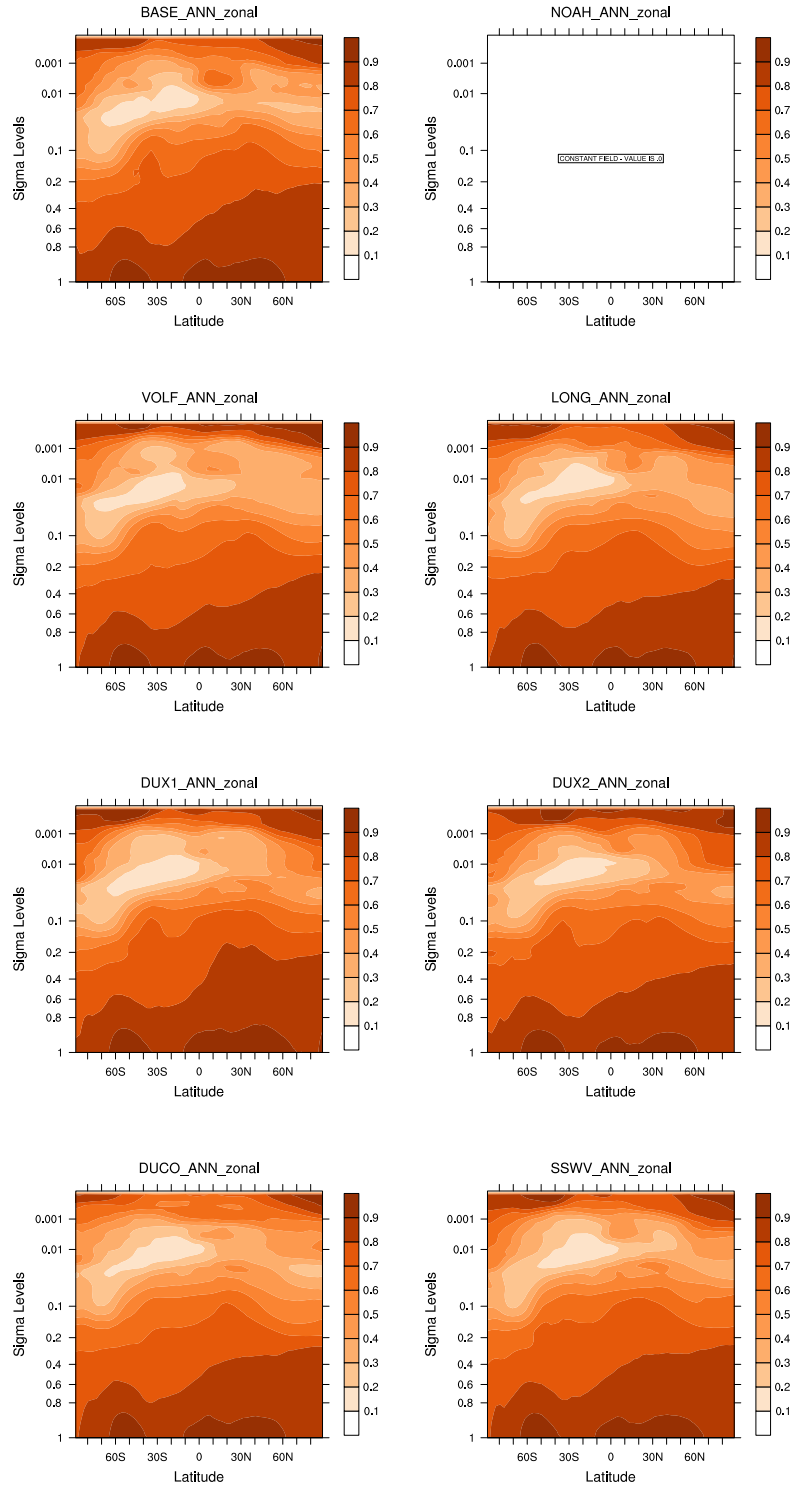


Figure 5.6. 2012 zonally averaged aerosol single-scattering albedo for BASE, NOAH, VOLF, LONG, DUX1, DUX2, DUCO, and SSWV experiments.

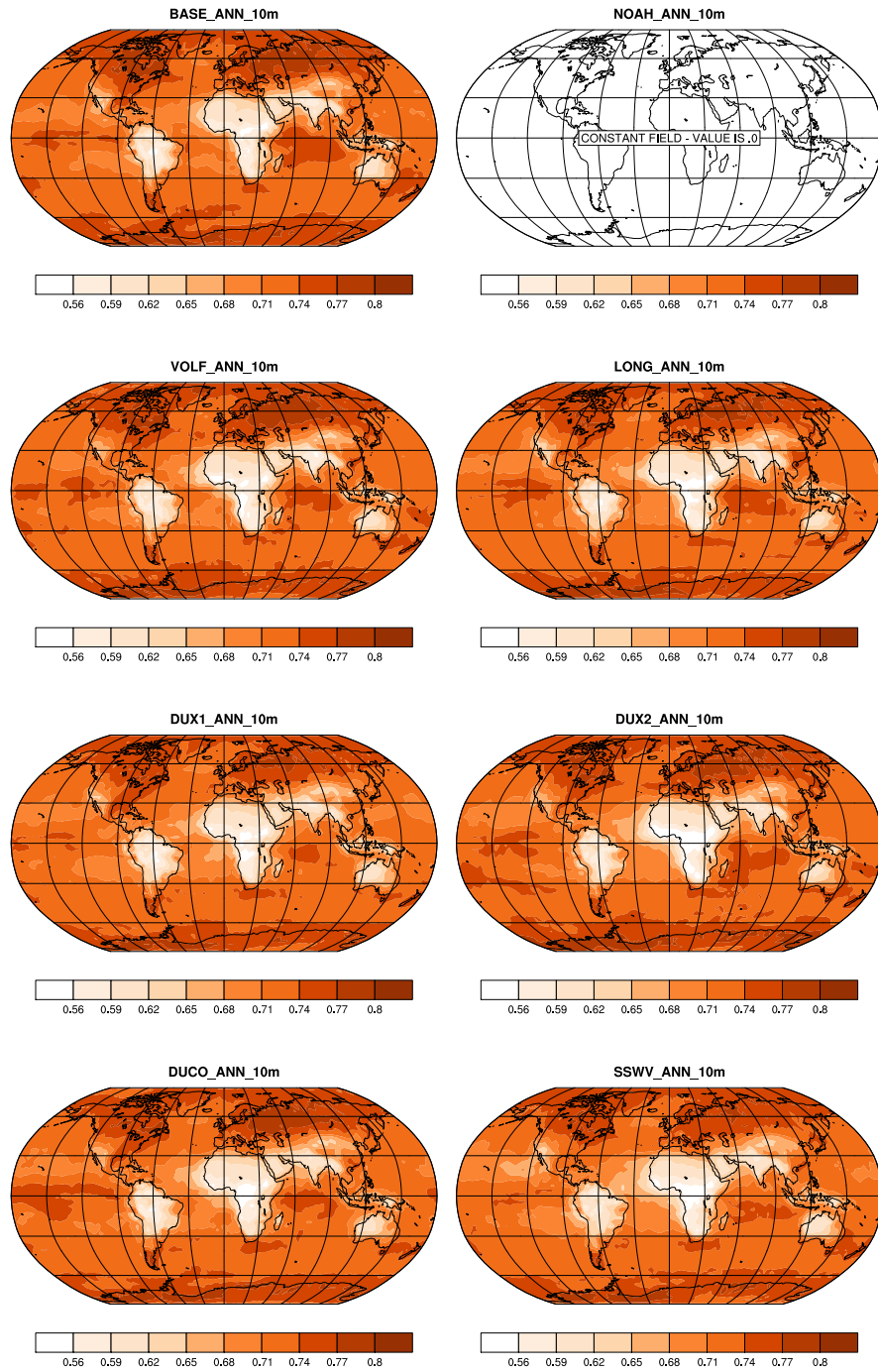


Figure 5.7. 10 m aerosol asymmetry parameter averaged over 2012 for BASE, NOAH, VOLF, LONG, DUX1, DUX2, DUCO, and SSWV experiments.

AERONET Site	Location	Time Period
Calhau, Cape Verde	16.864N, 24.867W	December, 2012
Dakar, Senegal	14.394N, 16.959W	July & December, 2012
Ispra, Italy	45.803N, 8.627W	July, 2012

Table 5.2. 2012 selected AERONET observation sites and the corresponding time periods used for comparison with GEM-AC

## 5.2.5 Comparisons to AERONET observations

### Selected AERONET Sites and Data

Aerosol optical property data at three AERONET observation sites are compared to the GEM-AC optical properties. The AERONET site locations and the associated time period are listed in Table 5.2. AERONET extinction optical depth, absorption optical depth, single-scattering albedo, and asymmetry parameter at  $0.439 \mu\text{m}$  and  $0.675 \mu\text{m}$  are used in the comparison to the GEM-AC extinction optical depth, absorption optical depth, single-scattering albedo, and asymmetry parameter of the model’s first shortwave spectral band defined in Table 4.2. Specifically, the respective optical properties in the first wavelength band of GEM-AC ( $0.2 \mu\text{m}$  to  $0.689 \mu\text{m}$ ) are compared to the average of the  $0.439 \mu\text{m}$  and  $0.675 \mu\text{m}$  AERONET optical properties.

### Temporal Collocation

AERONET observations are not periodic and are at different times compared to periodic GEM-AC output every three hours. It is desirable to have temporal sampling of the model output at the times of the observations. Schutgens et al. (2016) highlight this importance. In the GEM-AC and AERONET comparison, the GEM-AC output is temporally collocated to the respective AERONET observations: only GEM-AC output files that are closest to the observation time at each AERONET site are selected and used in the comparison.

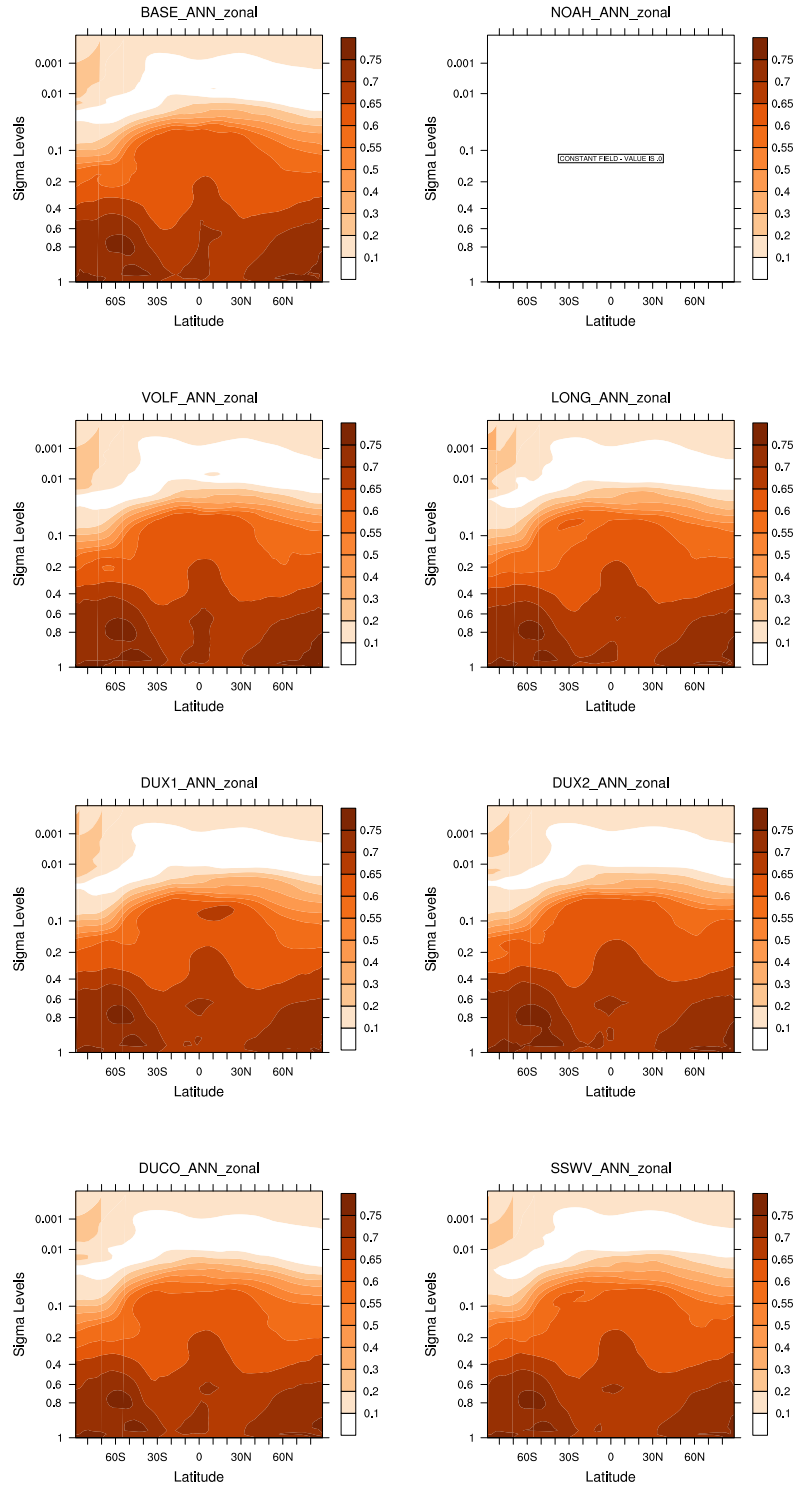


Figure 5.8. 2012 zonally averaged aerosol asymmetry parameter for BASE, NOAH, VOLF, LONG, DUX1, DUX2, DUCO, and SSWV experiments.

## Spatial Interpolation

After temporally collocating the model to the observations, the GEM-AC output is spatially interpolated to the location of the AERONET site. The NCL NCAR function `csa2l` fits a surface to two-dimensional data using a cubic spline interpolation. The `csa2l` function is used on the temporally selected GEM-AC output files to determine the GEM-AC value at the location of the respective AERONET observation sites listed in Table 5.2.

## Discussion

In general, GEM-AC under predicts aerosol optical depth with respect to other global models (Section 5.2.1). With respect to the AERONET observation sites, GEM-AC can also under predict aerosol optical depth, aerosol absorption optical depth, single-scattering albedo, and asymmetry parameter depending upon the region. During the time periods considered, GEM-AC under predicts at the two sites in North Africa, however, at the European site at Ispra, GEM-AC does well with prediction of the aerosol optical depth and tends to overpredict the aerosol asymmetry parameter.

The two sites at which GEM-AC under predicts aerosol optical properties are Dakar and Calhau located at the coast and offshore from western North Africa, respectively. Figure 5.1 shows that GEM-AC does not capture the placement of the large optical depths over northern Africa well compared to other global models. Other global models position the larger optical depths further west over the continent and extending offshore and also further south towards the Gulf of Guinea (Stier et al., 2005; Rotstayn et al., 2009; Pringle et al., 2010; Wang et al., 2011). In Stier et al. (2005) and Rotstayn et al. (2009) the large optical depth swath is directly over the Dakar and Calhau AERONET sites.

At Calhau, GEM-AC under predicts larger optical depths and adequately predicts the lowest optical depths (Figure 5.9a) and the aerosol asymmetry parameter tends to be off by

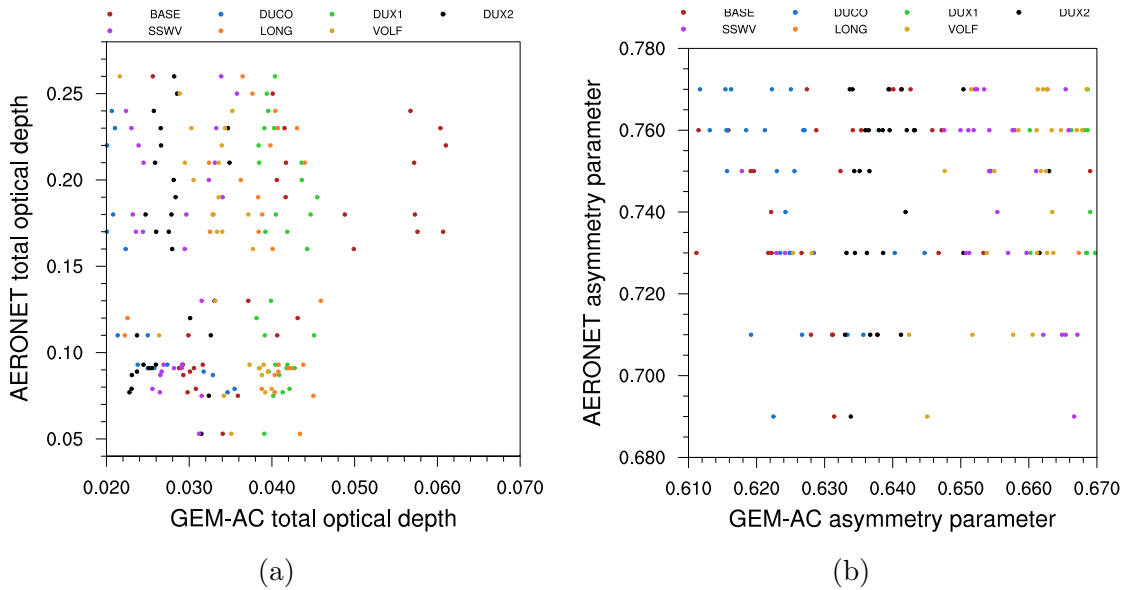


Figure 5.9. (a) GEM-AC aerosol optical depth versus AERONET aerosol optical depth, and (b) GEM-AC aerosol asymmetry parameter versus AERONET aerosol asymmetry parameter during December 2012 at Calhau, Cape Verde (16.864N, 24.867W).

about 0.1 (Figure 5.9b). At Dakar, GEM-AC does not capture the aerosol optical depth during July or December which tend to be large (Figures 5.10a, 5.10b and 5.11a). The GEM-AC aerosol single-scattering albedo and asymmetry parameter tend to be slightly lower than the observations (Figure 5.10c, 5.10d, and 5.11b).

GEM-AC seems to perform better at the Ispra AERONET site during July 2012. Figure 5.12a shows that the GEM-AC aerosol optical depths tend to agree with the AERONET optical depth at both lower and higher values. However, GEM-AC also has difficulty with the highest aerosol optical depths at this site too. The highest AERONET optical depths near 0.25 only correspond to GEM-AC values typically between 0.05 to 0.09. In contrast to the under prediction of the asymmetry parameter at Calhau and Dakar by about 0.1, at Ispra, GEM-AC tend to overpredictate the aysymmetry parameter by about 0.1 (Figure 5.12b).

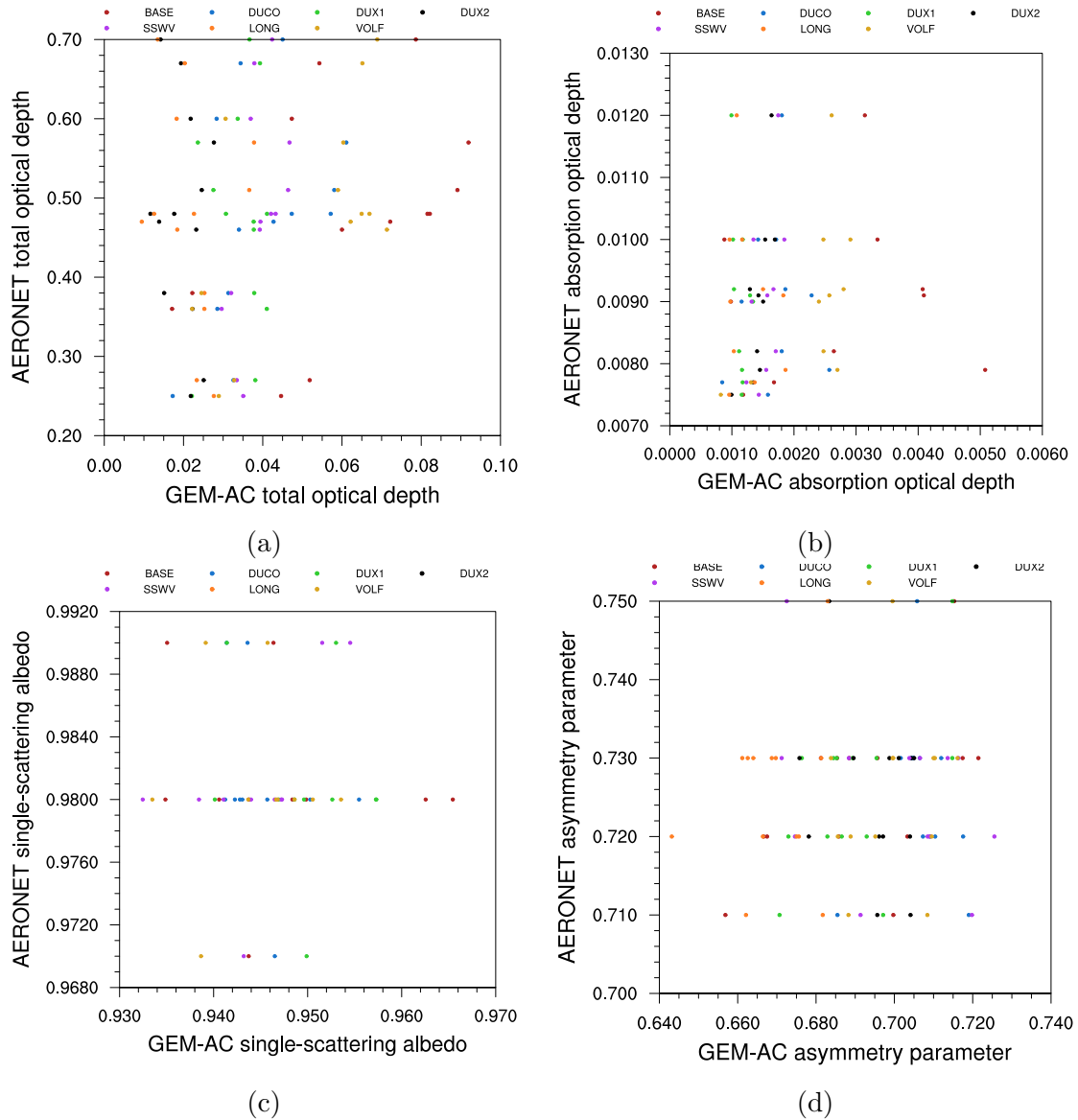


Figure 5.10. (a) GEM-AC aerosol optical depth versus AERONET aerosol optical depth, (b) GEM-AC aerosol absorption optical depth versus AERONET aerosol absorption optical depth, (c) GEM-AC aerosol single-scattering albedo versus AERONET aerosol single-scattering albedo, and (d) GEM-AC aerosol asymmetry parameter versus AERONET aerosol asymmetry parameter during July 2012 at Dakar, Senegal (14.394N, 16.959W).

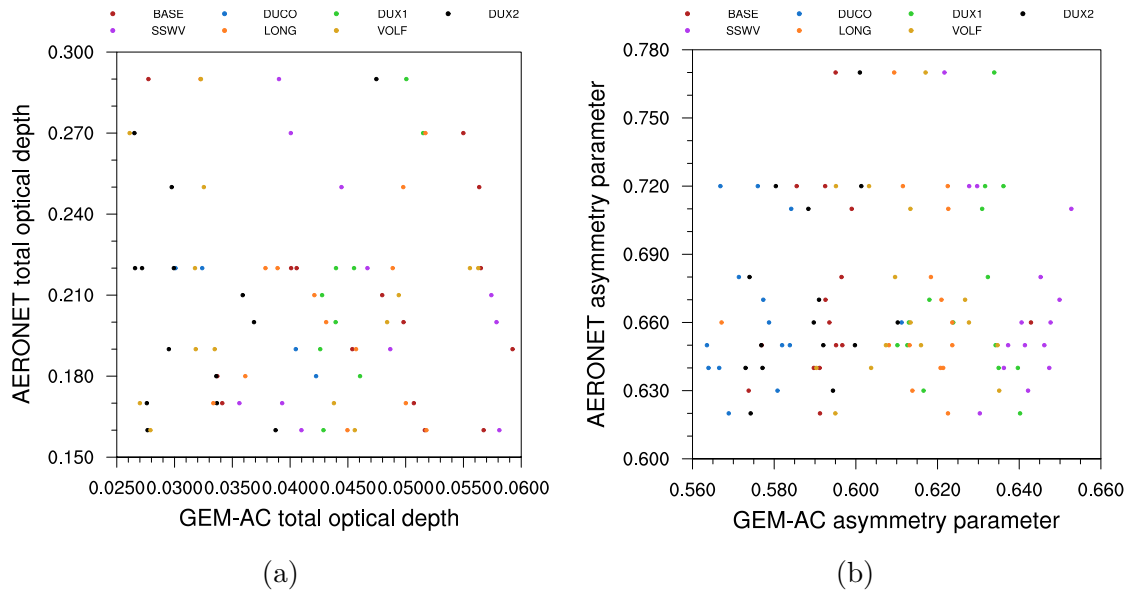


Figure 5.11. (a) GEM-AC aerosol optical depth versus AERONET aerosol optical depth, and (b) GEM-AC aerosol asymmetry parameter versus AERONET aerosol asymmetry parameter during December 2012 at Dakar, Senegal (14.394N, 16.959W).

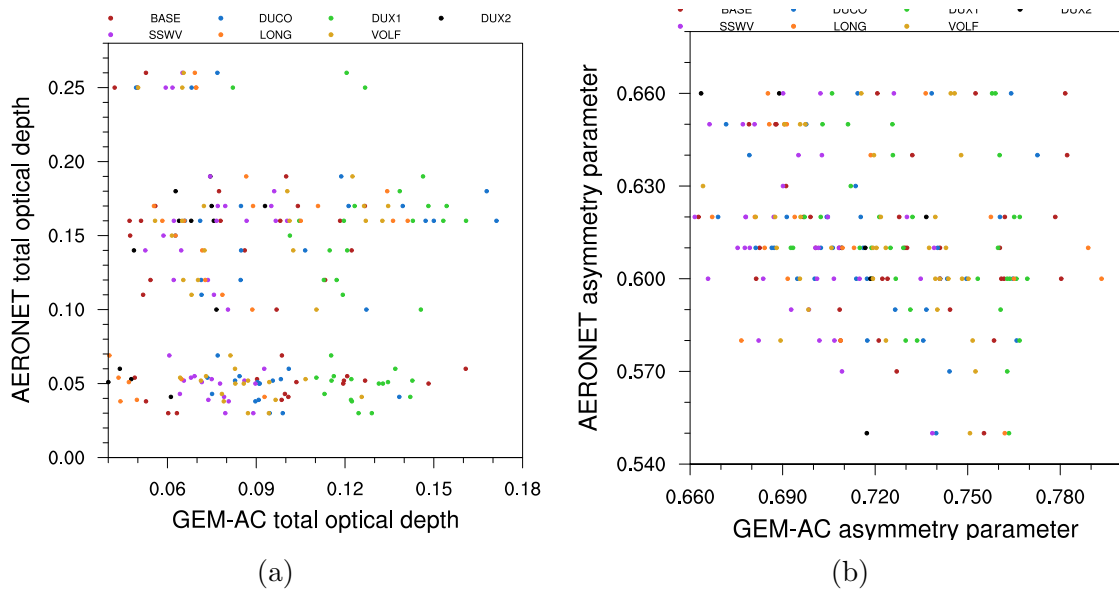


Figure 5.12. (a) GEM-AC aerosol optical depth versus AERONET aerosol optical depth, and (b) GEM-AC aerosol asymmetry parameter versus AERONET aerosol asymmetry parameter during July 2012 at Ispra, Italy (45.803N, 8.627E).

## 5.2.6 Air Temperature Distributions

Incorporating the aerosol direct effect into GEM-AC impacted the atmospheric temperature. The change in temperature is apparent in the 10 m temperature distribution in Figure 5.13 and in the zonal average in Figure 5.14. There is a 3.8°C increase in the annual average 10 m temperature between the NOAH and the BASE experiments (Table 5.3). This 3.8°C temperature change is not due to a difference between industrial and pre-industrial aerosols within the model, since the NOAH case contains no aerosols (aerosol optical depth is on the order of  $\sim 10^{-10}$ ). Allen and Sherwood (2011) show seasonal JJA and DJF differences between the atmospheric temperature changes due to natural and anthropogenic aerosol (natural + anthropogenic = total aerosol). In that work, the changes range from  $-3^{\circ}\text{C}$  to  $3^{\circ}\text{C}$  through the vertical structure of the atmosphere, but are mostly on the order of  $0.1^{\circ}\text{C}$  to  $0.3^{\circ}\text{C}$ . Within dust layers, Davidi et al. (2012) shows that dust can exhibit radiative heating between  $2^{\circ}\text{C}$  to  $4^{\circ}\text{C}$  within the layer. Within the vertical structure of the Community Atmosphere Model, Allen and Sherwood (2011) show that anthropogenic and natural (total) aerosols primarily heat the lower atmosphere when sea surface temperatures are fixed compared to overall cooling of the lower atmosphere when sea surface temperatures are not fixed and instead vary with a slab ocean model. In GEM-AC, sea surface temperatures are fixed and the number density tends to be underestimated by roughly a factor of 10 in most regions compared to other models (Section 5.3.1) which are probably contributing factors to the relatively large atmospheric heating at the 10 m level.

Compared to the difference between the BASE and NOAH zonal averages in Figure 5.14, there is relatively small variability between the BASE case and the six other experiments. Variability between the BASE, VOLF, LONG, DUX1, DUX2, DUCO, and SSWV cases is better observed in the 10 m annual distributions in Figure 5.13. Among the experiments, the most obvious difference in the 10 m distribution is over the central Atlantic Ocean, extend-

ing from the Cental African Republic and west towards Brazil, where the air temperature is simulated to be the highest in the DUX2 and SSWV experiments. However, the global average 10 m temperature is highest in the DUX1 and DUX2 case experiments (Table 5.3).

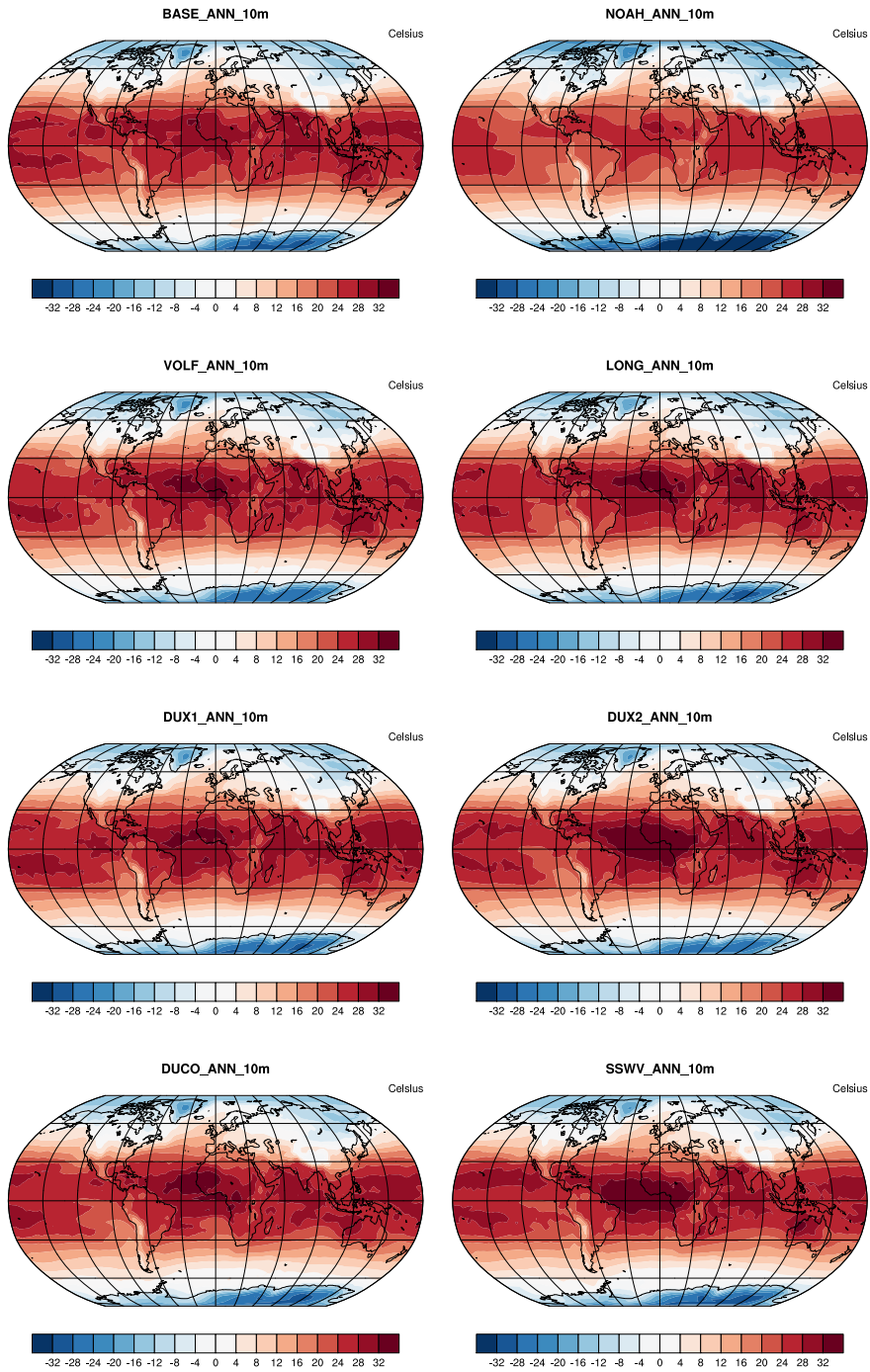


Figure 5.13. 10 m air temperature ( $^{\circ}\text{C}$ ) averaged over 2012 for BASE, NOAH, VOLF, LONG, DUX1, DUX2, DUCO, and SSWV experiments.

Season	CASE							
	BASE	NOAH	VOLF	LONG	DUX1	DUX2	DUCO	SSWV
Annual	8.3	4.5	8.3	8.4	8.7	8.8	8.4	8.6
DJF	8.5	4.5	8.5	8.8	8.9	8.9	8.6	8.7
MAM	7.4	3.8	7.4	7.3	7.6	8.1	7.4	7.7
JJA	10	6.0	9.9	10	11	10	10	11
SON	9.1	5.1	9.0	9.2	9.6	9.4	9.3	9.4

Table 5.3. 2012 global averages of the 10 m atmospheric temperature ( $^{\circ}\text{C}$ ) in the eight experiments.

## 5.3 Aerosol Mode and Species Distributions

### 5.3.1 Modes

The literature presents the aerosol number density at a standard atmospheric pressure and temperature (1013.25 hPa, 273.15 K). The aerosol number densities calculated in the aerosol optical property routine are presented here and are the level-dependent atmospheric pressure and temperature in the model:

$$N_k = \frac{1000p_k N_A m_k}{\mu R_d T_{air} (1 + 0.6w)} \quad (5.1)$$

where at each model level,  $N_k$  is the aerosol number density,  $N_A$  is Avogadro's number,  $p_k$  is the atmospheric pressure at level  $k$ ,  $m_k$  is the species or mode (mol/mol) mixing ratio at level  $k$ ,  $\mu$  is the average (gram) molar mass of air,  $R_d$  is the gas constant for dry air,  $T_{air}$  is the air temperature, and  $w$  is the volume mixing ratio of water vapour. In the four internally mixed modes, the number density of each mode is found using the mixing ratio of each mode. For the 3 externally mixed modes, the number density of each species in each mode is found using the mixing ratio of each species in each mode, and subsequently, the number density of each externally mixed mode is the sum of the species number densities. It is not possible to make an exact comparison between the literature presentations of the aerosol number densities and

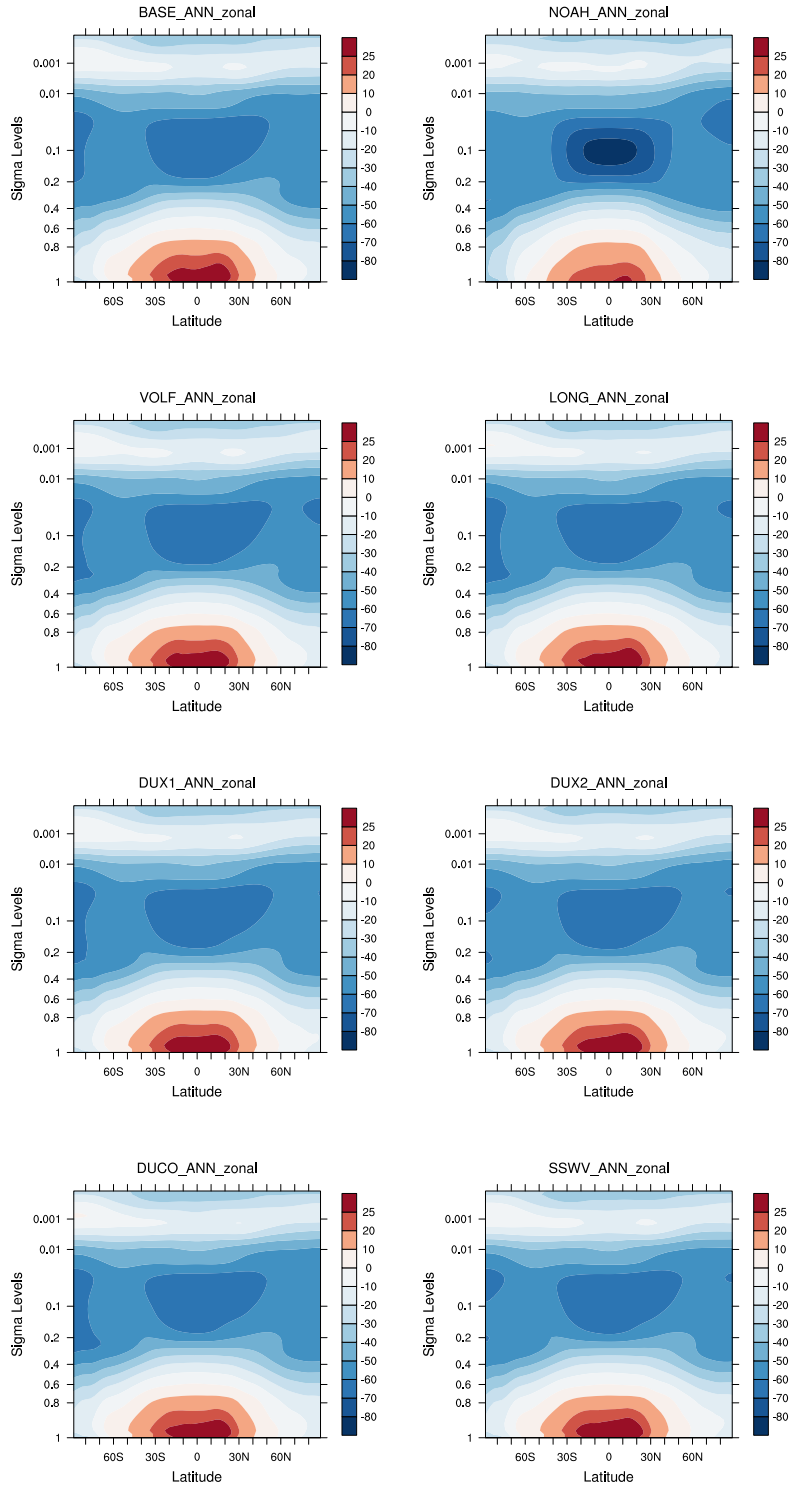


Figure 5.14. 2012 zonally averaged air temperature ( $^{\circ}\text{C}$ ) for BASE, NOAH, VOLF, LONG, DUX1, DUX2, DUCO, and SSWV experiments.

those in Figures D.1 through E.6, because the literature presents aerosol number density at the standard atmospheric pressure and temperature.

Aerosol number densities are not produced in the NOAA experiment. The aerosol number calculation is located in the aerosol optical property routine which is not called in the NOAA case. Aerosol number densities in the four soluble modes (Modes 1 to 4) are provided in Figures D.1 to D.8. Aerosol number densities in the three insoluble modes (Modes 5 to 7) are provided in Figures E.1 to E.6.

In general, there are some agreements and some disagreements between the GEM-AC 10 m and zonal average of the insoluble aerosol number densities and those in Zhang et al. (2010) (ECHAM5-HAM model) and Mann et al. (2010) (GLOMAP-mode model). Overall, the insoluble aerosol number densities in GEM-AC are most similar to those from Mann et al. (2010) which uses the GLOMAP-mode model while there tends to be more dissimilarities with Zhang et al. (2010) which uses the ECHAM5-HAM model. Comparing to Mann et al. (2010), GEM-AC tends to under predict the Aitken insoluble mode and overpredict the accumulation soluble mode, while there seems to be remarkable agreement with the coarse insoluble mode number density, including the zonal average.

Comparing the GEM-AC soluble mode aerosol concentrations to those presented in Mann et al. (2010) and Zhang et al. (2010) indicates that further investigation into the aerosol process parameterisations in GEM-AC needs to be performed. The aerosol microphysics module M7 treats the soluble aerosol processes: equilibrium with water vapour, condensation, nucleation, coagulation, and number/mass transfer among the modes, while wet deposition is represented using the Comprehensive Air-quality Model with eXtension (CAMx; CAMx (2011)) parameterisation. The soluble aerosol number density in the nucleation mode, Aitken mode, nucleation mode, and coarse mode all tend to be under predicted by GEM-AC. In fact, the 10 m soluble Aitken and accumulation number density are very similar to the insoluble Aitken number density which should not be the case.

Aerosol Mode	CASE							
	BASE	NOAH	VOLF	LONG	DUX1	DUX2	DUCO	SSWV
1	9.6	-	13.0	10.2	12.9	13.9	12.3	12.0
2	8.4	-	8.6	8.3	8.4	8.8	8.4	8.5
3	6.1	-	6.0	6.2	6.2	5.9	6.1	6.3
4	0.63	-	0.57	0.59	0.59	0.58	0.60	0.60
5	2.7	-	2.7	2.7	2.7	2.6	2.5	2.9
6	3.5	-	3.3	4.3	4.1	3.8	3.9	4.2
7	0.025	-	0.024	0.030	0.030	0.027	0.028	0.030

Table 5.4. 2012 global averages of the aerosol number density ( $\times 10^6 \text{ m}^{-3}$ ) in the seven M7 aerosol modes and eight experiments.

Yu and Zhang (2011) show that aerosol optical properties are very sensitive to the aerosol size distribution (a simplified example of how the aerosol heating rates respond to changes in size distribution is also shown in Appendix C). Specifically, Yu and Zhang (2011) show that the asymmetry factor, and extinction and scattering coefficients can vary by a factor of over  $\sim 300$  from changes in the aerosol distribution’s geometric standard deviation and geometric mean radius. In addition, they show variations in the the optical properites of up to 50% from changes in the aerosol real and imaginary refractive indices. The aerosol size distribution is controlled by numerous aerosol processes: emission, in situ formation, gas-to-particle conversion, nucleation, coagulation, gravitational settling, dry deposition, and wet deposition. An investigation into the sensitivity of the aerosol size distribution (and hence of the aerosol optical properties) on the aerosol processes within GEM-AC is warranted, but is beyond the objective of this dissertation.

### 5.3.2 Species

The 10 m and zonal averages of the molar volume mixing ratio of the eight aerosol species are shown in Appendix F. The aerosol water and sea salt volume mixing ratios are largest

over the Antarctic Circumpolar current. Strong westerlies drive the Antarctic Circumpolar current (Allison et al., 2010). Ocean waves and strong winds and are efficient sea spray emission mechanisms (Section 4.3). Over the arid continental regions, the dust mass volume mixing ratio is largest since dust emission from Earth's surface is strongest in these regions (Section 4.2). High concentrations reach the tropopause ( $\sim 0.1$  sigma level) between about 10N to 30N mostly by strong vertical transport near the Himilayas and are transported around the tropopause and southward (Fadnavis et al. (2013)).

Annual global load averages of the eight aerosol species are provided in Table 5.5 and the seasonal averages are provided Table G.5 to G.8. Only the SSWV, DUX1, and DUX2 experiments result in a lower  $\text{ANO}_3$  global average volume mixing ratio than the BASE experiment. These three experiments also show the largest increase in 10 m global average temperature from the BASE experiment (Table 5.3). Nitrate aerosol has significant consequences for regional air quality due to its solubility and radiative effects (Morgan et al., 2015). Wang et al. (2010) show that nitrate decreases surface air temperature through both the direct, indirect, and combined aerosol effects. This would explain the apparent connection between the global annual temperature increase and nitrate decrease in the SSWV, DUX1, and DUX2 experiments compared to the BASE experiment, however, investigating this in GEM-AC is beyond the scope of this dissertation. Overall, SSWV results in the most number of aerosol specie volume mixing ratios to increase relative to the BASE experiment compared to the other experiments: the volume mixing ratio of every aerosol species except aerosol nitrate increases in SSWV, and the aerosol sulphate volume mixing ratio essentially does not change.

Variable	CASE							
	BASE	NOAH	VOLF	LONG	DUX1	DUX2	DUCO	SSWV
ASO <sub>4</sub>	1.41	1.24	1.40	1.39	1.42	1.46	1.43	1.41
ANH <sub>4</sub>	0.0734	0.0743	0.0703	0.0716	0.0704	0.0705	0.0715	0.0739
ANO <sub>3</sub>	1.93	1.82	1.91	2.00	1.91	1.82	1.94	1.89
AH <sub>2</sub> O	56.5	85.6	55.5	57.0	57.4	55.1	58.0	57.0
AOC	0.925	0.515	0.833	0.889	0.918	0.807	0.884	0.930
ABC	0.111	0.0630	0.101	0.111	0.117	0.102	0.108	0.118
ADU	7.23	5.38	6.86	8.65	8.47	7.63	8.08	8.70
ASEA	13.4	19.3	13.1	13.4	13.5	12.9	13.5	13.6
NO <sub>2</sub>	18.9	18.4	18.8	18.8	18.8	18.7	18.5	18.7
NO <sub>3</sub>	0.121	0.108	0.123	0.118	0.123	0.114	0.116	0.109
N <sub>2</sub> O <sub>5</sub>	0.0252	0.0305	0.0249	0.0252	0.0234	0.0247	0.0242	0.0250
HNO <sub>3</sub>	36.7	34.6	36.3	36.1	36.2	36.2	36.6	35.7
O <sub>3</sub>	18100	17700	18100	18000	18000	18000	18100	18000
OH	0.672	0.671	0.672	0.672	0.672	0.672	0.672	0.671

Table 5.5. Annual global load averages ( $\times 10^{-10}$  mol mol<sup>-1</sup>) of aerosol sulphate (ASO<sub>4</sub>), aerosol ammonium (ANH<sub>4</sub>), aerosol nitrate (ANO<sub>3</sub>), aerosol water (AH<sub>2</sub>O), aerosol organic carbon (AOC), aerosol black carbon (ABC), aerosol dust (ADU), aerosol sea salt (ASEA), NO<sub>2</sub>, NO<sub>3</sub>, N<sub>2</sub>O<sub>5</sub>, HNO<sub>3</sub>, O<sub>3</sub>, and OH.

## 5.4 Example of an Implication for Atmospheric Chemistry

Chemical reaction rates in the atmosphere can be controlled by the environmental temperature through the frequency at which collisions between atmospheric molecules occur. Gas phase molecules can collide with aerosol particles and induce a heterogeneous chemical reaction on the surface of the aerosol. The reaction efficiency of an aerosol particle with a gas molecule generally depends upon the chemical composition of the aerosol and the environmental temperature. One of the most important heterogeneous reactions in both the troposphere and the stratosphere is  $\text{N}_2\text{O}_5$  hydrolysis and results from the eight model experiments on the chemical species involved in the reaction are presented in this section.

### 5.4.1 Heterogeneous Hydrolysis of $\text{N}_2\text{O}_5$

One of the most important tropospheric and stratospheric chemical reactions is the hydrolysis of  $\text{N}_2\text{O}_5$  (Dentener and Crutzen, 1993). Due to the importance of the reaction variant that occurs on the surface of aerosols, some general results are described here. The hydrolysis of  $\text{N}_2\text{O}_5$  with water vapour in the gas phase is slow, however, the hydrolysis on the surface of aerosol particles has been shown to be much faster (Tuazon et al., 1983; Dentener and Crutzen, 1993). The aerosol uptake of  $\text{N}_2\text{O}_5$  is an important sink of the nitrate radical,  $\text{NO}_3$ , and a major source of aerosol nitrate.

The uptake of  $\text{N}_2\text{O}_5$  on atmospheric aerosols can efficiently and indirectly remove  $\text{NO}_3$  from the gas phase, which significantly impacts both tropospheric and stratospheric chemistry. In the stratosphere, the formation of  $\text{HNO}_3$  from  $\text{N}_2\text{O}_5$  hydrolysis is important since  $\text{HNO}_3$  is a reservoir of  $\text{NO}_x$ . The  $\text{N}_2\text{O}_5$  hydrolysis is represented in GEM-AC by the treatment in the Comprehensive Air-quality Model with eXtension (CAMx; CAMx (2011)). Com-

paring the BASE experiment which has the direct aerosol effect to the NOAH experiment which does not have the direct aerosol effect, Figure 5.16 shows that by introducing the aerosol direct effect into GEM-AC, the amount of  $\text{N}_2\text{O}_5$  in the Arctic stratosphere decreases and the amount in the south pole stratosphere increases. In tropospheric chemistry,  $\text{N}_2\text{O}_5$  hydrolysis has a major impact on the  $\text{NO}_x$  cycle. The rate of  $\text{O}_3$  and aerosol production under high (low)  $\text{NO}_x$  conditions increases (decreases) due to the hydrolysis of  $\text{N}_2\text{O}_5$  (Riemer et al., 2003). The aerosol direct effect in GEM-AC, raises the global average of  $\text{NO}_2$  and  $\text{NO}_3$ , and  $\text{O}_3$  (Table 5.5).

A major product of  $\text{N}_2\text{O}_5$  hydrolysis is  $\text{HNO}_3$ . Riemer et al. (2003) showed that  $\text{HNO}_3$  is potentially a major source of nitrate aerosol. The introduction of aerosol radiative heating increased the global average of  $\text{HNO}_3$  by 1 to 2  $\text{mol mol}^{-1}$  and increased the global average of  $\text{ANO}_3$  in all cases except DUX2 (Table 5.5). In northwestern Europe in summertime, Morgan et al. (2015) showed that in high concentration areas, ammonium nitrate was found to suppress  $\text{N}_2\text{O}_5$  hydrolysis. Aerosol nitrate in the form of ammonium nitrate predominates submicron modes at continental sites (Putaud et al., 2004). In all eight experiments, the surface distribution of aerosol nitrate is shown in Figure F.5 and the surface distribution of the aerosol number density in the soluble nucleation, Aitken, and accumulation modes in Figures D.1 to D.5. The aerosol direct effect increased the 10 m concentration of  $\text{N}_2\text{O}_5$  in Europe and eastern North America (Figure 5.15), however, the global average decreased (Table 5.5).

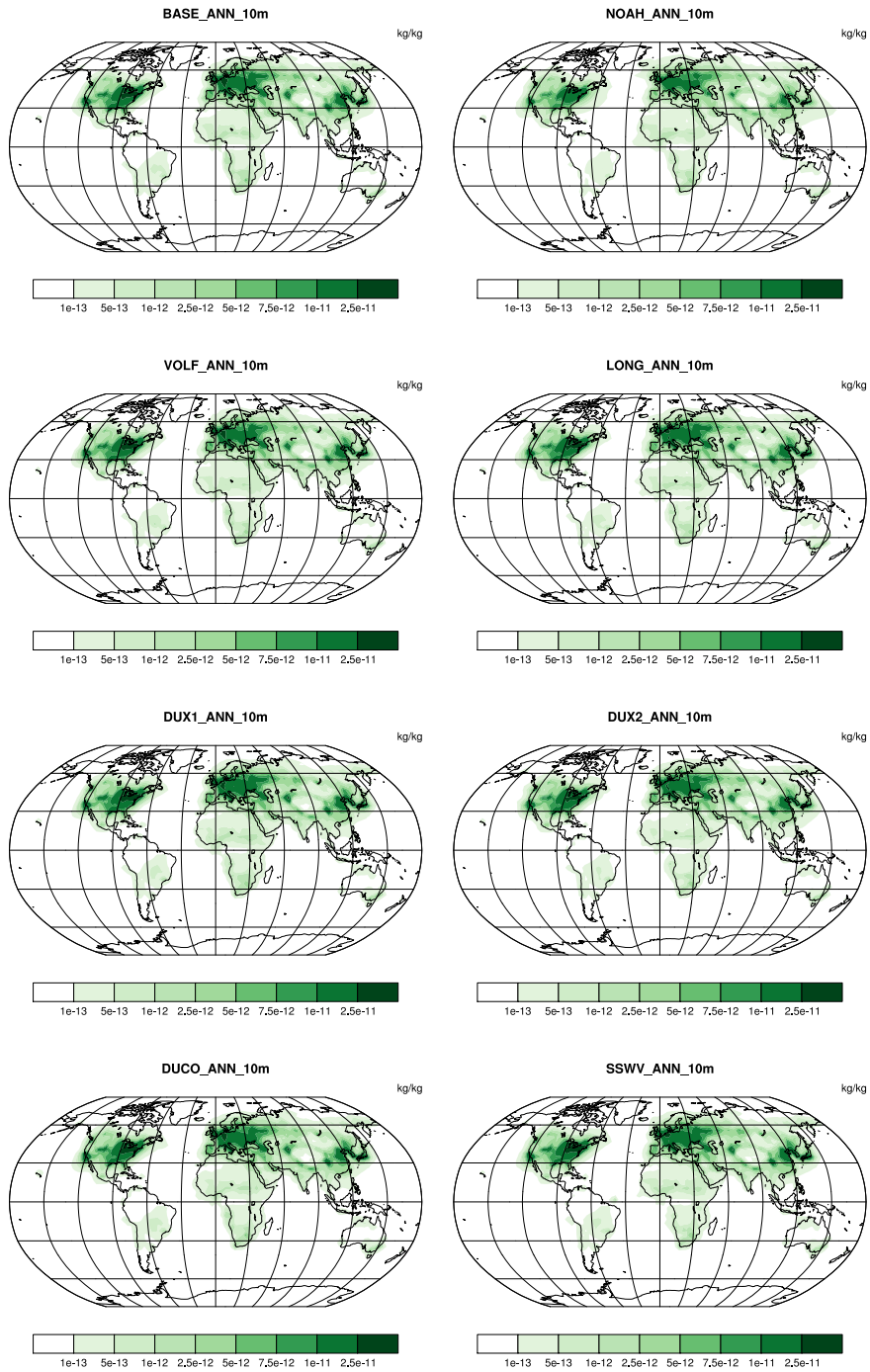


Figure 5.15. 10 m N<sub>2</sub>O<sub>5</sub> volume mixing ratio averaged over 2012 for BASE, NOAH, VOLF, LONG, DUX1, DUX2, DUCO, and SSWV experiments.

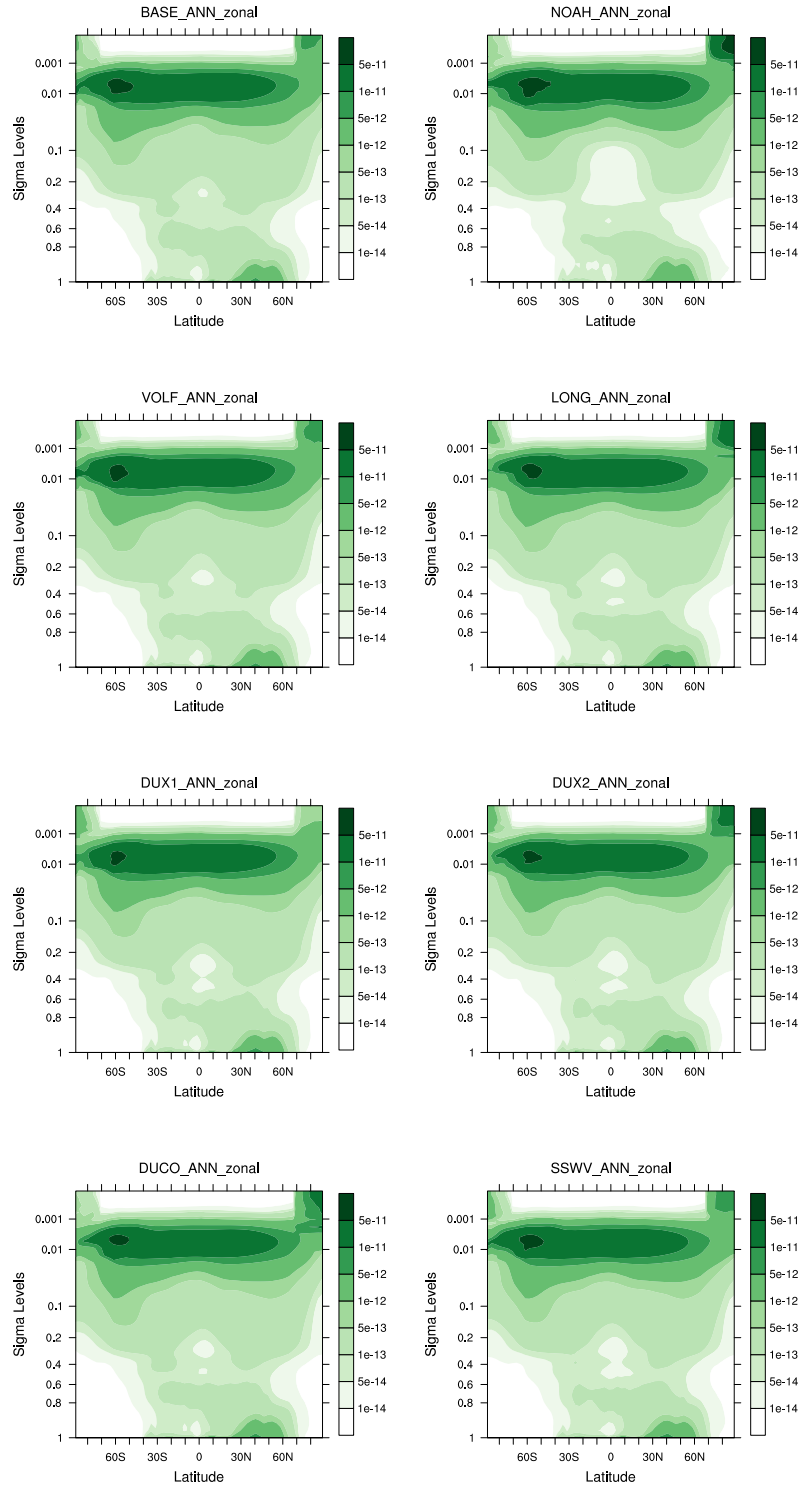


Figure 5.16. 2012 zonally averaged  $N_2O_5$  volume mixing ratio for BASE, NOAH, VOLF, LONG, DUX1, DUX2, DUCO, and SSWV experiments.

# Chapter 6

## Conclusion

### 6.1 Contributional Objective

Atmospheric aerosols directly and indirectly impact the global climate system, and thus their radiative effects must be included in global atmospheric chemistry and climate models. It has been shown in the literature that dust aerosol contributes the most out of all other aerosol species to the global mean aerosol optical depth since it is a strong scatterer and absorber of both solar and planetary radiation. Moreover, roughly two thirds of earth's surface is covered by ocean that emits sea salt particles which can interact solubly with atmospheric gases and aerosol water, sulphate, nitrate, ammonium, black carbon, organic carbon, and dust. It is these three reasons that the objectives of this thesis, ordered by importance, are:

- Equip GEM-AC with the aerosol direct effect.
- Equip GEM-AC with a dust emission routine that relies on the model meteorology.
- Equip GEM-AC with a new sea salt emission routine that encapsulates ocean wave state as a function of wind speed and sea surface temperature.

## 6.2 Contributional Results

I have implemented the aerosol direct effect in GEM-AC along with several new options for aerosol representation. I have shown that by not feeding aerosol optical properties into the model's radiative transfer routine, the model can underpredict air temperature throughout the atmosphere even if the aerosol optical properties themselves are underpredicted in the model. Within the aerosol optical property calculation, I provide two mixing state options for the soluble modes: volume fraction mixing and Bruggeman mixing. Another option I have added allows the user to activate aerosol radiative transfer at more than one longwave spectral band. For the two most abundant aerosol species, I have provided more realistic emission parameterisations; dust emission can now be interactive and sea salt emission can now be modulated by sea-state.

## 6.3 Limitations of this Research

This dissertation shows the necessity of including direct aerosol radiative effects in GEM-AC. Furthermore, this dissertation provides new options in GEM-AC with the installation of recent interactive dust and sea salt emission routines which have resulted in improved simulations in other models.

This dissertation does not claim a superior method in the representation of dust and sea salt aerosol in GEM-AC. Nor does this dissertation investigate the sensitivity of the aerosol size distribution to the model microphysics; specifically, the underlying underprediction of the aerosol number density is not investigated.

## 6.4 Recommendations for Future Work

The aerosol optical depth, absorption optical depth, single-scattering albedo, and asymmetry parameter are underpredicted by GEM-AC. The tendency for underprediction likely stems from the inability of GEM-AC to correctly simulate the aerosol number concentration. The aerosol size distribution is subject to numerous microphysical processes. Aerosol emission, in situ formation, and atmospheric processing such as gas-to-particle conversion, coagulation, gravitational settling, dry deposition, and wet deposition all act to characterise the aerosol size distribution. The differences in the size distribution of the soluble aerosol modes in GEM-AC compared to other models needs to be addressed, since the aerosol optical properties are size dependent. A natural direction stemming from this dissertation would be a sensitivity analysis of the various microphysical processes on the aerosol radiative properties in GEM-AC. Following a sensitivity analysis, improvement in the microphysical processes within GEM-AC could be made. Subsequently, exploring the best configuration of the newly implemented dust and sea salt routines in GEM-AC could be explored.

## 6.5 Final Remark

GEM-AC now has a functioning representation of the aerosol direct radiative effect and is now equipped with several updated dust and sea salt emission parameterisations, mixing state schemes and an option for aerosol radiative treatment in more longwave spectral bands. The use of size dependent aerosol optical properties in the radiative transfer scheme allows for more accurate chemistry and climate simulations in GEM-AC applications. Dust emission dependent on model meteorology is now an option, as opposed to the AeroCom benchmark emission dataset. Another implemented option is wave-encapsulated wind and sea surface temperature dependent emission of sea salt, as opposed to emission which depends only on

wind speed. With a wider range of options now available in GEM-AC, there is a wider range of applicable scenarios in which it can be used.

# Appendices

# Appendix A

## Motivation and Background of Atmospheric Dust Modelling on Mars

Dust is the major aerosol species in the Martian atmosphere, playing an important role in Mars' radiation budget and influencing the radiative flux at all wavelengths. Dust absorbs and scatters in both the visible and infrared while simultaneously emitting thermal infrared energy. Dust affects both the incoming solar energy and outgoing thermal infrared energy, and plays a major role in the atmospheric circulation of Mars by inducing temperature changes which alter pressure gradients. Implementation of the dust cycle, complete with lifting, a size distribution, transport, interaction with the water cycle and heating is an important goal for Mars Global Climate Models (GCMs). In order to completely account for the effect of dust on GCM temperatures, the optical properties of radiatively active dust must be calculated based on the size distribution. The 3D physical processes listed above impacting dust induce spatial variations of the size distribution which may impact the heating rates. It is therefore pertinent to examine fundamentally how dust heating changes with the dust size model parameters.

Beginning with the first major numerical papers on dust storms, Gierasch and Goody

(1973) and Haberle et al. (1982), the basic dynamic response to radiatively active dust during dust storm conditions is well-known by chain causality: dust absorbs solar energy, temperature increases, pressure decreases, intensification of vertical ascent through convective and diffusive processes, and dust transportation to higher latitudes by the meridional circulation. The major climate modeling studies on dust transport and storms in recent years include those by Basu et al. (2004), Basu et al. (2006), Kahre et al. (2006), Kahre et al. (2008), Madeleine et al. (2011), and Newman et al. (2005). Rafkin et al. (2011) provide insight into the positive radiative and dynamic feedback of dust during all stages of a dust storm, adding to the earlier work in Rafkin (2009) on Wind Enhanced Interaction of Radiation and Dust. Dust is initially lifted by wind into the atmosphere where solar energy absorption by dust locally increases the atmospheric temperature. The increase in low-level temperature reduces the pressure and amplifies the pressure gradient. The accelerated surface wind injects more dust into the atmosphere, enhancing the initial dust lifting. Rafkin et al. (2011) additionally find that during the initial and mature stages of a dust storm, large dust concentrations can be contained in the lowest layers even with cumulative optical depths as large as  $\tau \sim 5$ . The large dust concentration causes an increased intensity of solar energy absorption, which increases temperature and enhances the thermal infrared energy emission. The lower the vertical extent of the large dust concentration, the more intense the solar absorption and thermal infrared emission.

Measurements by imagers and infrared sounders indicate that dust is not always distributed uniformly throughout the atmospheric column and varies with space and time. Dust can be confined to the lower atmosphere, or its concentration can be vertically extensive reaching up to 75 km in equatorial regions during dust storms (Jaquin et al., 1986; Cantor, 2007). In polar regions, dust tends to reside in the lower layers. McCleese et al. (2010) observe equinoctial and solstitial modes in the latitudinal vertical distribution. At equinox, dust reaches high altitudes over the tropics as a result of a Hadley-like circulation with decreasing

altitude-penetration toward the poles, while at solstice, high-altitude dust is also observed over the tropics with much less dust in the atmosphere at mid- (to perhaps polar-) latitudes in the winter hemisphere and moderate altitude-penetration near the summer pole. Simple vertical dust distributions based on the original profile of the dust mass mixing ratio of Conrath (1975) have typically been used in most Mars GCMs (e.g., *Forget et al.*, 1999; *Moudden and McConnell*, 2005) to account for the vertical variation of dust. As noted above, however, the size distribution and vertical distribution of dust on Mars is expected to be temporally and spatially variable, and they are thus critical sources of uncertainty in many Mars GCMs.

There are few papers to date which are dedicated solely to the topic of atmospheric dust heating on Mars. General aspects of dust radiative heating, from quantitative temperature responses to impacts on the local and meridional circulation, can be inferred from the numerous papers on retrievals, parameterizations, and GCM modeling of the optical properties, distribution, and transport of dust, but the non-trivial nature of radiative dust heating promotes in-depth and basic study of its own. Two of the first Martian dust heating papers are by Zurek (1978) who used the  $\delta$ -Eddington approximation, and by Davies (1979) who used Monte Carlo multiple-scattering, for heating simulations in the short wavelength bands, but these papers did not consider radiative transfer in the long wavelength bands. With thermal emission spectra Santee and Crisp (1993) developed a technique to simultaneously estimate atmospheric dust loading and surface and atmospheric temperatures, providing the first self-consistent global view of dust optical depths and temperature profiles. Fuerstenau (2006) looked at the dynamic link between dust devils and solar absorption, and suggested that the additional buoyancy provided by the absorption of solar radiation within a plume is an explanation for the prevalence of large-scale dust devils. Dust radiative heating in GCM studies generally assumes that dust is well-mixed and in thermal equilibrium with the background atmosphere so that the remaining solar energy not attenuated by dust is attenuated by atmospheric gases such as CO<sub>2</sub>. Decoupling of the dust and gas temperatures at higher

altitudes occurs at a given pressure, dependent upon dust particle size, and will affect the heating by all atmospheric constituents (Goldenson et al., 2008).

Development of interactive dust modelling has recently begun in Mars GCMs (Basu et al., 2004, 2006; Kahre et al., 2006, 2008; Madeleine et al., 2011; Newman et al., 2002a,b; Wilson et al., 2008) to account for the spatial and temporal distribution, building upon the earlier modelling studies which incorporated uniform atmospheric dust (Haberle et al., 1982, 1993). Dust transport simulations performed by Basu et al. (2006), Kahre et al. (2008), Newman et al. (2002b), and Wilson et al. (2008) had revealed the possibility of upper-level dust layers. The most recent observations from the Mars Climate Sounder (MCS) aboard the Mars Reconnaissance Orbiter (MRO) have shown that the vertical distribution of dust can have upper-level dust maximums (ULDMs) (McCleese et al., 2010; Heavens et al., 2011a,b). Heavens et al. (2011b) provide an analysis of retrieved dust opacity profiles from the MCS revealing high-altitude maximums in the dust mass mixing ratio over the tropics during most of northern spring and summer. In the southern spring and summer, their observations indicate dust concentration decreasing with altitude. These new insights into the vertical distribution of dust and the persisting, critical uncertainty in the spatial variation of the size distribution, lead to the question of how the dust heating rates respond to the size and vertical distributions of dust.

# Appendix B

## Simple Column Model of Dust in the Mars Atmosphere

### B.1 The Size and vertical distribution

Analytic size distributions of dust in the Martian atmosphere are often represented as modified-gamma or log-normal with the first two moments, the effective radius ( $R_{eff}$ ) and the effective variance ( $\nu_{eff}$ ), characterizing the distribution. Based upon the characteristics of Brownian coagulation and sandblasting Montmessin et al. (2002) suggest that dust modelling in Mars GCMs is better represented by a log-normal size distribution. Regarding dust aerosol on Earth, Kok (2011) finds that the measured dust aerosol distribution is scale invariant and in better agreement with a distribution describing fragmentation of brittle materials than with a log-normal distribution. In this study involving Mars dust aerosol, dust particles with radii  $r = 0.1 - 5.0 \mu\text{m}$  are considered and a log-normal size distribution is employed, viz.,

$$\frac{dN}{d \ln(r/r_0)} = \frac{N_t(z)}{\sqrt{2\pi} \ln \sigma_\nu} \exp \left[ - \frac{(\ln(r/r_0) - \ln(\bar{r}/r_0))^2}{2(\ln \sigma_\nu)^2} \right] \quad (\text{B.1})$$

where  $N_t(z)$  is the total number of dust particles per unit volume at height  $z$ ,  $r$  is the dust particle radius,  $r_0$  is an arbitrary reference radius taken to be  $1 \mu\text{m}$ ,  $\bar{r}$  is the median radius, and  $\sigma_r$  is the geometric standard deviation. As input to the distribution, the effective radius and effective variance are the first two moments of the distribution and are related to the median radius and geometric standard deviation as  $\nu_{eff} = e^{(\ln \sigma_r)^2} - 1$ , and  $R_{eff} = \bar{r}(1 + \nu_{eff})^{5/2}$ . Most of the presented analysis assumes that the effective radius and effective variance are constant with height, however, the impact that a linearly decreasing  $R_{eff}$  and  $\nu_{eff}$  with height have on the heating rates is discussed in Section C.4. A remaining input parameter is the dust mass mixing ratio at the surface,  $q_t(z=0)$ , from which the vertical profile of the dust is extended via a scaling factor ( $\alpha$ ):  $q_t(z) = \alpha(z)q_t(0)$ .

The mixing ratio profiles that are considered here (Figure B.1(a)) are intended to reflect the mixing ratio profiles of Newman et al. (2002b), Heavens et al. (2011a), and Heavens et al. (2011b). One classic dust profile, the Conrath profile (Conrath, 1975), is included in the comparison. The mixing ratio profiles converted to total dust number density are shown in B.1(b).

## B.2 Optical Properties

### B.2.1 Mie scattering

Particle interaction with radiation either scatters or absorbs some fraction of the incident energy impinging on the particle. The *total* extinction from scattering and absorption of the incident radiation per cross-sectional area of the particle is called the extinction efficiency:

$$Q_e = Q_s + Q_a, \tag{B.2}$$

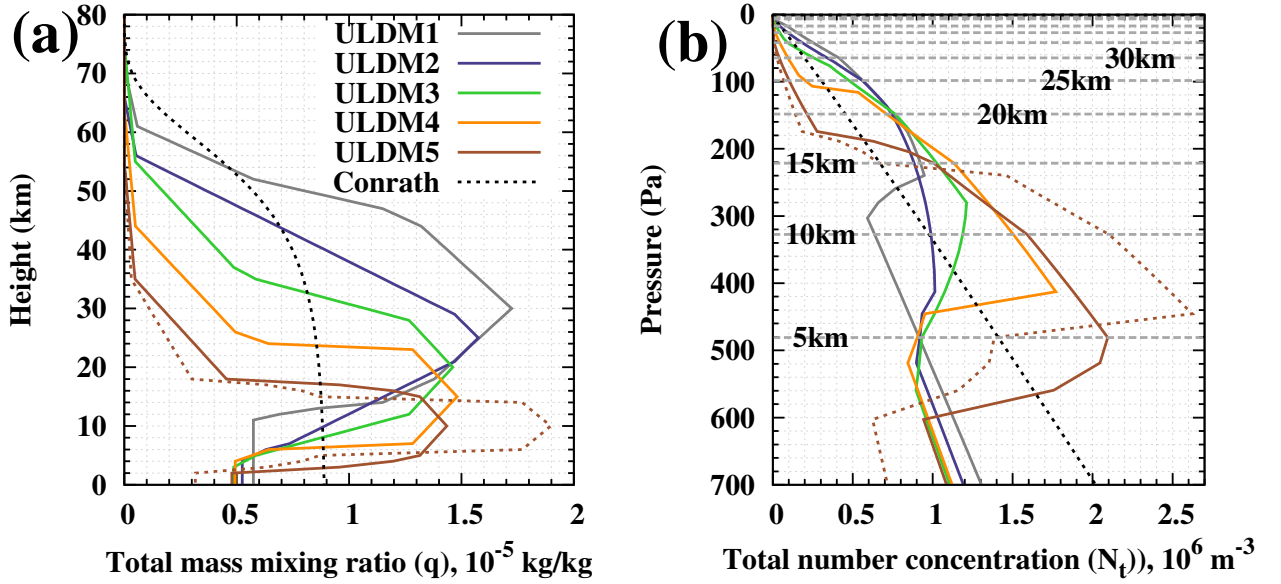


Figure B.1. Profiles of the (a) dust mass mixing ratio and (b) total dust number concentration, for the dust scenarios ULDM1-ULDM5 having dust maxima at 30 km, 25 km, 20 km, 15 km, and 10 km, respectively, which are  $3\times$  the surface mass mixing ratio ( $3q_t(0)$ ). The ULDM5 profile is also extended to have a mass mixing ratio maximum of  $6q_t(0)$  (brown dashed curve). The Conrath profile is described by  $q_t(z) = q_t(0) \exp(0.007[1 - p(0)/p])$ , where in our case  $p(0) = 700$  mb.  $R_{eff} = 1.7 \mu\text{m}$ ,  $\nu_{eff} = 0.3$ ,  $\varepsilon = 0.9$ ,  $T_G = 260$  K, and the cumulative dust optical depth at the surface is unity. Note that the number concentrations in (b) are shown as a function of altitude with 5-km incremental height levels shown.

where  $Q_s$  and  $Q_a$  are likewise the extinction efficiencies from scattering and absorption, respectively. The basis of Mie theory allows for the exact calculation of the extinction and scattering efficiencies for spherical particles which interact elastically with radiation:

$$Q_e(r, \lambda) = \frac{2}{\alpha^2} \sum_{k=1}^{\infty} (2k+1) \operatorname{Re}(a_k + b_k) \quad (\text{B.3})$$

$$Q_s(r, \lambda) = \frac{2}{\alpha^2} \sum_{k=1}^{\infty} (2k+1) (|a_k|^2 + |b_k|^2). \quad (\text{B.4})$$

The Mie scattering coefficients,  $a_k$  and  $b_k$ , are functions of the size parameter ( $\alpha = 2\pi r/\lambda$ ) and the refractive index of dust ( $n = n_r - n_i$ ), and are computed recursively in Mie scattering code adopted from Wiscombe (1979) which has downward and upward recursive conditions. The code also takes into account the small-particle limit ( $|n|\alpha \leq 0.1$ ) and no absorption limit ( $n_i \rightarrow 0$ ). The real and imaginary dust refractive indices are from Wolff and Clancy (2003) for wavelengths 0.2 to 0.6  $\mu\text{m}$  and 3.0 to 200.0  $\mu\text{m}$ , and from Wolff et al. (2009) for wavelengths 0.6 to 3.0  $\mu\text{m}$ . Figure B.2 shows  $n_r$  and  $n_i$  as a function of wavelength. The Mie scattering code exists as a subroutine within the column model looping over 50 dust radius sizes ranging from  $r = 0.1$  to 5.0  $\mu\text{m}$  in increments of 0.1  $\mu\text{m}$  and 126 wavelengths within the range 0.2 to 200.0  $\mu\text{m}$ .

## B.2.2 Optical depth

The dust optical depth is the attenuation of radiation by a factor of e due to the scattering and absorption by dust aerosols through the vertical column. For a given wavelength and dust size the dust optical depth is

$$\bar{\tau}(r, \lambda, z) = \int_z^{\infty} \sigma_e(r, \lambda) n(r, z) dz \quad (\text{B.5})$$

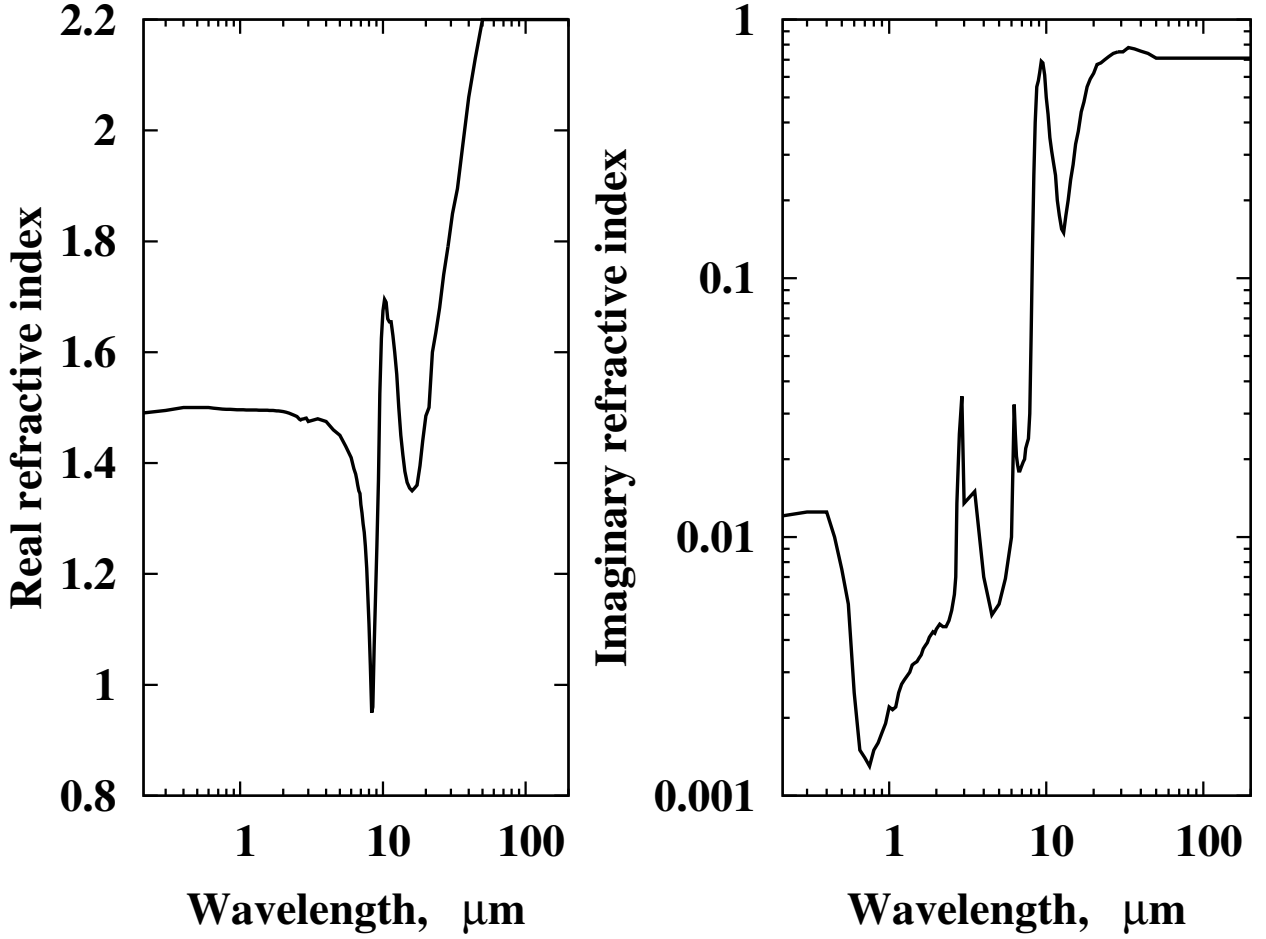


Figure B.2. Real and imaginary refractive indices of Mars dust.

where  $\sigma_e(r, \lambda) = \pi r^2 Q_e(r, \lambda)$  is the extinction cross-section and  $n(r, z)$  is the number of dust particles per unit volume (Eq. B.1).

The radiative transfer calculation is carried out over two shortwave bands,  $\lambda_1 = 0.2$  to  $0.5 \mu\text{m}$  and  $\lambda_2 = 0.5$  to  $5.0 \mu\text{m}$ , and over three longwave bands,  $\lambda_3 = 5.0$  to  $11.5 \mu\text{m}$ ,  $\lambda_4 = 11.5$  to  $20.0 \mu\text{m}$ , and  $\lambda_5 = 20.0$  to  $200.0 \mu\text{m}$ , and the size distribution of dust radii  $r = 0.1$  to  $5.0 \mu\text{m}$ . Thus, an extinction cross-section representative of each wavelength band is required for the distribution. Following Forget (1998) the extinction and scattering efficiencies of each dust size are averaged over each of the 5 wavelength bands as

$$\bar{Q}_{e,s}(r, \lambda) = \frac{\int_{\lambda_a}^{\lambda_b} B(\lambda) Q_{e,s}(r, \lambda) d\lambda}{\int_{\lambda_a}^{\lambda_b} B(\lambda) d\lambda} \quad (\text{B.6})$$

where in the shortwave bands  $B(\lambda)$  represents the solar radiance ( $T = 6000$  K) and in the longwave bands  $B(\lambda)$  represents Mars' blackbody intensity at the surface ( $T = 215$  K), and  $\lambda_a$  and  $\lambda_b$  are the limits of the given wavelength band, i.e.,  $\lambda_a = 0.21 \mu\text{m}$  and  $\lambda_b = 0.5 \mu\text{m}$  for the  $\lambda_1$  band. Then, weighting the extinction cross-section and scattering efficiency over the size distribution gives the required properties:

$$\bar{\sigma}_e(R_P, \lambda, z) = \frac{\sum_{r=r_a}^{r_b} n(r, z) \pi r^2 \bar{\sigma}_e(r, \lambda)}{\sum_{r=r_a}^{r_b} n(r, z) \pi r^2} \quad \text{and} \quad (\text{B.7})$$

$$\bar{Q}_s(R_P, \lambda, z) = \frac{\sum_{r=r_a}^{r_b} n(r, z) \pi r^2 \bar{Q}_s(r, \lambda)}{\sum_{r=r_a}^{r_b} n(r, z) \pi r^2}, \quad (\text{B.8})$$

where  $r_a$  and  $r_b$  are the lower and upper bounds of the size distribution, i.e.,  $r_a = 0.1 \mu\text{m}$  and  $r_b = 5.0 \mu\text{m}$ . The dust optical depth of the distribution in each wavelength band is then

$$\tau(R_P, \lambda, z) = \int_z^\infty \bar{\sigma}_e(R_P, \lambda, z) \sum_{r=r_a}^{r_b} n(r, z) dz. \quad (\text{B.9})$$

### B.2.3 Single-scattering albedo

The fraction of extinction by scattering of incident radiation impinging on a particle is the single-scattering albedo:

$$\omega(r, \lambda) = \frac{Q_s(r, \lambda)}{Q_e(r, \lambda)}. \quad (\text{B.10})$$

The single-scattering albedo as a function of dust radius ( $r$ ) and wavelength ( $\lambda$ ) is shown in Fig. B.3a. At wavelengths 0.5 to 5.0  $\mu\text{m}$  there is generally strong scattering and weak absorption corresponding to the relatively low values of the imaginary refractive index (Fig. B.2), except at about 3  $\mu\text{m}$  where a spike in  $n_i$  means more radiative absorption by a dust particle. And of course, smaller dust particles are more efficient at scattering radiation with a wavelength comparable to the dust radius. Fig. B.3c shows the band-averaged single-scattering albedo (Forget, 1998) for each dust radius size:

$$\bar{\omega}(r, \lambda) = \frac{\int_{\lambda_a}^{\lambda_b} B(\lambda) Q_e(r, \lambda) \omega(r, \lambda) d\lambda}{\int_{\lambda_a}^{\lambda_b} B(\lambda) Q_e(r, \lambda) d\lambda}, \quad (\text{B.11})$$

however, the band-averaged single-scattering albedo of the size distribution is found using the typical relation, the fraction of the total extinction due to scattering:

$$\bar{\omega}(R_P, \lambda, z) = \frac{\sum_{r=r_a}^{r_b} n(r, z) \pi r^2 \bar{Q}_s(r, \lambda)}{\sum_{r=r_a}^{r_b} n(r, z) \pi r^2 \bar{Q}_e(r, \lambda)} \quad (\text{B.12})$$

where  $n(r, z)$  is the size distribution (Eq. B.1), and  $\bar{Q}_e(r, \lambda)$  and  $\bar{Q}_s(r, \lambda)$  are the band-averaged extinction and scattering efficiencies in Eq. B.6. The single-scattering albedo of the distribution for each wavelength band and configuration of the size distribution is shown in Table B.1.

## B.2.4 Asymmetry parameter

The asymmetry parameter ( $g$ ) is the first moment of the angular distribution of scattered energy (the phase function,  $P(\Phi)$ ). It represents the relative direction of scattering by a particle: strong-forward scattering as  $g \rightarrow 1$ , strong backward scattering as  $g \rightarrow -1$ , and

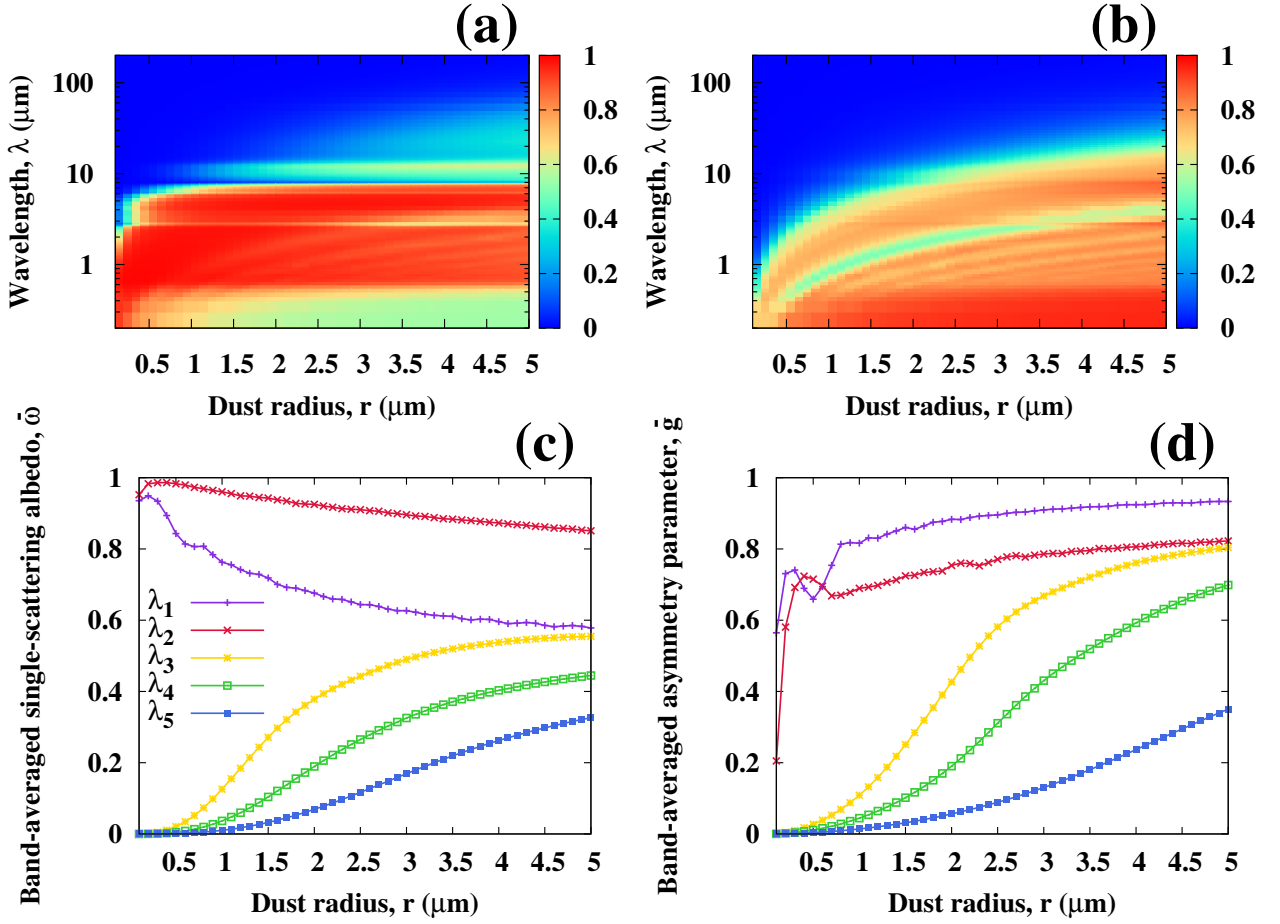


Figure B.3. (a) Single-scattering albedo ( $\omega(r, \lambda)$ ), and (b) asymmetry parameter ( $g(r, \lambda)$ ) at each of the 50 dust radii and 113 wavelengths, and (c) band-averaged single-scattering albedo  $\bar{\omega}(r, \lambda)$ , and (d) band-averaged asymmetry parameter ( $\bar{g}(r, \lambda)$ ) for wavelength bands  $\lambda_1 = 0.21$  to  $0.5 \mu\text{m}$ ,  $\lambda_2 = 0.5$  to  $5.0 \mu\text{m}$ ,  $\lambda_3 = 5.0$  to  $11.5 \mu\text{m}$ ,  $\lambda_4 = 11.5$  to  $20.0 \mu\text{m}$ , and  $\lambda_5 = 20.0$  to  $200.0 \mu\text{m}$ .

isotropic scattering for  $g = 0$ . In terms of the Mie scattering coefficients (Wiscombe, 1979),

$$g = \frac{4}{Q_s \alpha^2} \sum_{k=1}^{\infty} \left[ \frac{k(k+2)}{k+1} \text{Re}(a_k a_{k+1}^* + b_k b_{k+1}^*) + \frac{2k+1}{k(k+1)} \text{Re}(a_k b_k^*) \right] \quad (\text{B.13})$$

and is shown in Fig. B.3b as a function of  $r$  and  $\lambda$ . The strongest forward scattering is observed at wavelengths  $0.21$  to  $0.5 \mu\text{m}$  and  $g$  tends to increase with increasing dust radius.

As with the other optical properties, the asymmetry parameter is band-averaged as

$$\bar{g}(r, \lambda) = \frac{\int_{\lambda_a}^{\lambda_b} B(\lambda) Q_e(r, \lambda) \omega(r, \lambda) g(r, \lambda) d\lambda}{\int_{\lambda_a}^{\lambda_b} B(\lambda) Q_e(r, \lambda) \omega(r, \lambda) d\lambda} \quad (\text{B.14})$$

and shown in Fig. B.3d. The weighted mean of  $\bar{g}$  over the size distribution is

$$\bar{g}(R_P, \lambda, z) = \frac{\sum_{r=r_a}^{r_b} n(r, z) \pi r^2 \bar{g}(r, \lambda)}{\sum_{r=r_a}^{r_b} n(r, z) \pi r^2} \quad (\text{B.15})$$

where  $n(r, z)$  is the size distribution (Eq. B.1), and  $\bar{g}(r, \lambda)$  is the band-averaged asymmetry parameter in Eq. B.14. The resulting asymmetry factor for each wavelength band and size distribution configuration are shown in Table B.1.

### B.3 Radiative transfer parameterization

Interaction of dust particles with the sources of radiation are different in shortwave and longwave spectra and so calculation of radiative transfer requires that different methods be used at short and long wavelengths. In the shortwave, solar radiation is scattered and absorbed by dust. Depending upon the dust size and wavelength, attenuation of solar radiation is mostly by scattering. Within the second shortwave band,  $\lambda_2$ ,  $\omega$  is largest (Fig. B.3a,c) and is larger for the smaller dust particles. A distribution with a smaller effective radius will have a larger number of smaller dust sizes, and so the distribution's single-scattering albedo will also be larger within  $\lambda_1$  and  $\lambda_2$  (Table B.1). While less absorption takes place in the  $\lambda_2$  band, absorption can be important in the  $\lambda_1$  band, where  $\omega < 0.6$  for  $r > 1.0 \mu\text{m}$  and in particular, the single-scattering albedo of the  $R_{eff} = 1.7 \mu\text{m}$  and  $2.0 \mu\text{m}$  dust distributions are  $\sim 0.58$ . Dust particles are also greybodies, emitting energy in the thermal infrared and

	$\lambda_1$	$\lambda_2$	$\lambda_3$	$\lambda_4$	$\lambda_5$
$R_{eff} = 1.4 \mu\text{m}, \nu_{eff} = 0.3$					
$\omega$	0.7106	0.9364	0.3626	0.2193	0.1081
$g$	0.8539	0.7300	0.3276	0.1728	0.0554
$R_{eff} = 1.7 \mu\text{m}, \nu_{eff} = 0.3$					
$\omega$	0.6882	0.9265	0.4023	0.2574	0.1360
$g$	0.8699	0.7431	0.4053	0.2285	0.0753
$R_{eff} = 2.0 \mu\text{m}, \nu_{eff} = 0.3$					
$\omega$	0.6711	0.9181	0.4303	0.2859	0.1585
$g$	0.8811	0.7541	0.4688	0.2788	0.0945
$R_{eff} = 1.7 \mu\text{m}, \nu_{eff} = 0.2$					
$\omega$	0.6891	0.9277	0.3889	0.2375	0.1176
$g$	0.8703	0.7400	0.3931	0.2109	0.0671
$R_{eff} = 1.7 \mu\text{m}, \nu_{eff} = 0.4$					
$\omega$	0.6884	0.9259	0.4100	0.2689	0.1469
$g$	0.8689	0.7443	0.4115	0.2387	0.0804

Table B.1. The single-scattering albedo ( $\omega$ ) and asymmetry factor ( $g$ ) of each size distribution configuration within each wavelength band:  $\lambda_1 = 0.2$  to  $0.5 \mu\text{m}$ ,  $\lambda_2 = 0.5$  to  $5.0 \mu\text{m}$ ,  $\lambda_3 = 5.0 - 11.5 \mu\text{m}$ ,  $\lambda_4 = 11.5$  to  $20.0 \mu\text{m}$ , and  $\lambda_5 = 20.0$  to  $200.0 \mu\text{m}$ . For clarity the optical properties for the linearly decreasing  $R_{eff}$  and  $\nu_{eff}$  cases are not shown since they are height dependent (see Sections B.3.1 and C.4).

simultaneously absorbing emitted thermal infrared radiation from the planet’s surface. At infrared wavelengths radiative scattering by dust tends to be small (Fig. B.3a) and isotropic (Fig. B.3b). Multiple-scattering, however, can also be important in the longwave bands, particularly for larger dust sizes where  $\omega$  can be as large as 0.6 (Fig. B.3c) and scattering is less isotropic (Fig. B.3d). Two parameterizations are used in this research which both account for multiple-scattering in an atmosphere composed of a series of homogeneous dust layers: two-stream quadrature for solar radiation and a combined two- and four- stream solution for thermal infrared radiation. Both solutions are extended to an inhomogeneous atmosphere using the tri-diagonal method.

### B.3.1 The dust layers

The configuration of the dust layers along with the upward and downward source and emergent fluxes are shown in Figure 2.1. The dust column is a series of 80 homogenous, 1 km thick dust layers. The air temperature is given a linear lapse rate, decreasing from 260 K at the surface to 175 K at 80 km.

The optical properties of each size bin can be layer-dependent since they are a function of the dust distribution. When  $R_{eff}$  and  $\nu_{eff}$  are constant with height, the size distribution in Eq. B.1 does not vary with height (except for the scaling by  $N_t(z)$ ) and the optical properties are therefore constant with height. On the other hand, when  $R_{eff}$  and  $\nu_{eff}$  vary with height, the single-scattering albedo ( $\omega_n$ ) and asymmetry parameter ( $g_n$ ) will be different for each  $n$  (Eq. B.1, Eq. B.12 and Eq. B.15).

### B.3.2 The similarity principle

Scattering by dust can be strongly peaked in the forward direction which can lead to inaccurate fluxes from a layer when there is significant absorption by dust (Liou, 2002). Since multiple scattering is not neglected in this research, the fraction of scattered energy in the forward peak must be removed from the optical properties. Doing so essentially adjusts for the first-order approximation of the phase function which can be inadequate with large  $g$ . The adjustment of  $\omega$ ,  $g$ , and  $\tau$  incorporates the second moment of the phase function which (i) is the fraction of scattered energy in the forward peak and (ii) is neglected in the expansion in the first-order expansion of the phase function. For simplicity, and although the Henyey-Greenstein phase function is not explicitly used, the second-moment of the phase function is assumed to be  $g^2$  so that the adjusted asymmetry parameter can be simply represented as  $g' = g/(1+g)$ . Additionally, the adjusted single-scattering albedo is  $\omega' = [\omega(1-g^2)]/(1-\omega g^2)$  and the adjusted optical thickness is  $\tau' = \tau(1 - \omega g^2)$ .

### B.3.3 Two-Stream Quadrature

Solar radiative transfer is computed using two-stream quadrature. The method in Toon et al. (1989) extends the two-stream quadrature solution of a homogeneous layer to a series of homogeneous layers using the tridiagonal solution technique. The algorithm used in this research to compute the shortwave fluxes is presented in detail in Toon et al. (1989) and will not be re-presented here.

### B.3.4 Two- and Four- Stream Combination Solution

The two- and four- stream combination approximation in Fu et al. (1997) is used to calculate thermal infrared radiative transfer in which multiple-scattering is not neglected. The method uses the two-stream quadrature scheme to solve the source function allowing

calculation at each level interface of the upward and downward intensities for 4 streams, and then applying double Gauss quadrature for the radiative fluxes. Since their paper does not explicitly detail the method for an inhomogeneous atmosphere, the fundamentals of the tridiagonal two- and four- stream combination solution is presented in this section.

For each homogeneous layer the solution of the source function using two-stream quadrature is given in Fu et al. (1997). Thus, for a given stream  $\mu$ , the upward intensity at the top of layer  $n$  ( $\tau = 0$ ) is

$$I_n(0, \mu) = I_n(\tau_n, \mu)e^{-\tau_n/\mu} + \frac{G_n}{k_n\mu - 1} \left( e^{-\tau_n/\mu} - e^{-k_n\tau_n} \right) \quad (\text{B.16})$$

$$+ \frac{H_n}{k_n\mu + 1} \left[ 1 - e^{-\tau_n(k_n+1/\mu)} \right] + \frac{\zeta_n}{1 - \mu\beta_n} \left[ B(0) - B(\tau_n)e^{-\tau_n/\mu} \right],$$

and the downward intensity at the bottom of layer  $n$  ( $\tau = \tau_n$ ) is

$$I_n(\tau_n, -\mu) = I_n(0, -\mu)e^{-\tau_n/\mu} + \frac{J_n}{k_n\mu + 1} \left[ 1 - e^{-\tau_n(k_n+1/\mu)} \right] \quad (\text{B.17})$$

$$+ \frac{K_n}{k_n\mu - 1} \left( e^{-\tau_n/\mu} - e^{-\tau_n k_n} \right) + \frac{\eta_n}{1 + \mu\beta_n} \left[ B(\tau_n) - B(0)e^{-\tau_n/\mu} \right],$$

where the  $k$ ,  $G$ ,  $H$ ,  $J$ ,  $K$ ,  $\zeta$ , and  $\eta$  parameters are listed in Table B.2, and the Planck function is approximated exponentially with  $B(\tau) = B(0)e^{\beta\tau}$ ,  $\beta = (1/\tau_n) \ln[B(\tau_n)/B(0)]$ . The coefficients  $Y_{1n}$  and  $Y_{2n}$  are determined by applying boundary conditions and applying the tridiagonal solution technique to the system of general two-stream radiative transfer solutions (of each layer):

Parameter	Expression
$\gamma_{1n}$	$D \left[ 1 - \frac{\omega_n}{2} (1 + g_n) \right]$
$\gamma_{2n}$	$\frac{D\omega_n}{2} (1 - g_n)$
$k_n$	$(\gamma_{1n}^2 - \gamma_{2n}^2)^{1/2}$
$\Gamma_n$	$\frac{\gamma_{1n} - k_n}{\gamma_{1n}}$
$G_n$	$\frac{Y_{1n} + Y_{2n}}{\pi} \left( 1 - \frac{k_n}{D} \right)$
$H_n$	$\frac{\Gamma_n (Y_{1n} - Y_{2n})}{\pi} \left( 1 + \frac{k_n}{D} \right)$
$J_n$	$\frac{\Gamma_n (Y_{1n} + Y_{2n})}{\pi} \left( 1 + \frac{k_n}{D} \right)$
$K_n$	$\frac{Y_{1n} - Y_{2n}}{\pi} \left( 1 - \frac{k_n}{D} \right)$
$\zeta_n$	$(1 - \omega_n) \left( 1 + \frac{(D\omega_n)(\gamma_{1n} + \gamma_{2n} + g_n \beta_n)}{k_n^2 - \beta_n^2} \right)$
$\eta_n$	$(1 - \omega_n) \left( 1 + \frac{(D\omega_n)(\gamma_{1n} + \gamma_{2n} - g_n \beta_n)}{k_n^2 - \beta_n^2} \right)$

Table B.2. Parameters used in the Two- and Four- Stream Combination parameterization with  $D = 2$  as the diffusivity factor.

$$F_n^+(\tau) = Y_{1n} \left[ e^{-k_n(\tau_n - \tau)} + \Gamma_n e^{-k_n \tau} \right] + Y_{2n} \left[ e^{-k_n(\tau_n - \tau)} - \Gamma_n e^{-k_n \tau} \right] \quad (\text{B.18a})$$

$$+ \frac{D(1 - \omega) \pi B(\tau_n)}{k_n^2 - \beta_n^2} (\gamma_{1n} + \gamma_{2n} + \beta_n)$$

$$F_n^-(\tau) = Y_{1n} \left[ \Gamma_n e^{-k_n(\tau_n - \tau)} - e^{-k_n \tau} \right] + Y_{2n} \left[ \Gamma_n e^{-k_n(\tau_n - \tau)} - e^{-k_n \tau} \right] \quad (\text{B.18b})$$

$$+ \frac{D(1 - \omega) \pi B(\tau_n)}{k_n^2 - \beta_n^2} (\gamma_{1n} + \gamma_{2n} - \beta_n)$$

with the boundary conditions:

$$F_1^-(0) = 0 \tag{B.19}$$

$$F_N^+(\tau_N) = \sigma F_N^-(\tau_N) + \epsilon \pi B(\tau_N)$$

$$F_n^+(\tau_n) = F_{n+1}^+(0)$$

$$F_n^-(\tau_n) = F_{n+1}^-(0),$$

where  $\sigma$  is the surface albedo and  $\epsilon = 1 - \sigma$  is the surface emissivity. The algorithm for the explicit determination of the set of  $Y_{1n}$  and  $Y_{2n}$  is given in Toon et al. (1989).

The upward and downward intensities in each layer (Eq. B.16 and B.17) are calculated with the streams  $\mu_1 = 0.2113248$  and  $\mu_2 = 0.7886752$ , and the weights  $a_1 = a_2 = 0.5$ . By employing double Gauss quadrature, the upward and downward fluxes at each  $\tau$  level are

$$F^\pm(\tau) = \pi \left[ \mu_1 I(\tau, \pm\mu_1) + \mu_2 I(\tau, \pm\mu_2) \right]. \tag{B.20}$$

### B.3.5 Interpretation of the results

The heating and cooling of the Martian atmosphere due to dust is a complex process involving lifting processes, gravitational sedimentation, ice formation, size-dependent solar absorption and scattering, and size-dependent thermal infrared absorption, scattering, and emission. This study helps clarify some of the impacts not always addressed by GCM studies. The calculations explore and anticipate possible heating processes that may be encountered in developing 3-D interactive dust models. As such, dust is the only constituent considered in the atmospheric column; if the column were dust-free, the shortwave and longwave radiative fluxes would be constant throughout the atmospheric column and the heating rates would be zero at each level.

The context in which the heating of the atmospheric column is explored must be noted. To first order the ground acts as an external energy source within the longwave spectral bands and the sun as an external energy source within the shortwave spectral bands. The heating rate responses to dust in a perturbed atmospheric column which is fixed in time and has not adjusted to thermal equilibrium are presented. Provision of the convectively-adjusted radiative equilibrium column temperatures does not clarify the results since the objective here is to compare and contrast the instantaneous heating effects. The heating rates should thus be regarded as tendencies in the heating responses to dust and not as resultant heating.

The shortwave, longwave, and net heating rates are presented in Sections C.1 to C.5 but note that at night only the longwave heating and cooling will occur. Given that the ground and atmospheric temperatures can be much cooler at night, Section C.6 is included which discusses the results for nighttime ground temperatures with a linear decrease in atmospheric temperature from 105 K at 80 km to 190 K at 0 km. The magnitude of the thermal infrared cooling will be smaller under nighttime conditions, however, I will show that in both dust profiles the impacts of the nighttime ground temperature on the heating rates tend to be larger in magnitude than the daytime impacts.

# Appendix C

## Radiative Heating and Cooling of Mars Dust Aerosol

Each differential dust layer  $(\delta z)_n = z_{n-1} - z_n$  has an associated heating rate from the interaction of dust aerosol with radiation:

$$\left(\frac{\partial T}{\partial t}\right)_n = -\frac{1}{\rho_n C_P} \frac{(\delta F)_n}{(\delta z)_n} \quad (\text{C.1})$$

where  $\rho_n$  is the density of the atmospheric layer and  $C_P = 860 \text{ m}^2\text{s}^{-2}\text{K}^{-1}$  (Leovy, 2001) is the Mars atmosphere specific heat at constant pressure. The net flux density divergence of each layer is

$$-\frac{(\delta F)_n}{(\delta z)_n} = -\frac{(F_n^- - F_n^+) - (F_{n-1}^- - F_{n-1}^+)}{(\delta z)_n} \quad (\text{C.2})$$

with  $F_n^- - F_n^+$  being the net flux of layer  $n$ . The emergent radiative fluxes from the defined layers are depicted in Fig. 2.1.

Dust heating and cooling can be discussed in terms of the magnitude. In this work, maximum cooling refers to the maximum cooling rate, that is, the lowest negative heating

rate value. Likewise, a maximum heating refers to the highest positive heating rate value. Moreover, cooling refers to a negative heating rate and heating refers to a positive heating rate such that a decrease in cooling refers to change from a more negative heating rate to a less negative heating rate, and a decrease in heating refers to change from a more positive heating rate to a less positive heating rate.

## C.1 Heating rates of upper-level dust maximum scenarios

Vertical distributions of the total mass mixing ratio and dust number concentration containing upper level dust maximums (ULDMs) are shown in Figure B.1. The mass mixing ratio profiles ULDM1-ULDM5 contain a peak mixing ratio which is  $3\times$  the surface mass mixing ratio. The Conrath profile is also considered and as noted earlier is historically the common form used in past GCM modelling studies. All of the profiles shown yield a unit optical depth at the surface. The shortwave, longwave, and net (shortwave + longwave) heating rates of each dust profile are provided in the top panel of Figure C.1.

The respective shortwave, longwave, and net flux density divergence profiles are shown in the bottom panel of Figure C.1. Figures C.1(d,e) show that maximum absorption of solar energy and maximum absorption of thermal infrared energy occur at roughly the same height at which the total number concentration is a maximum. While the net thermal infrared emission offsets the net solar absorption, the maxima in the net flux density divergence (that is, the level at which the energy gain is a maximum within the respective dust profile) occur near the level at which there is a maximum in the dust number density within the column. The heating maxima roughly correspond to the divergence maxima in the lower layers, but in the upper layers the heating maxima result from the decrease of the background atmospheric

density with increasing height:

$$(\partial T/\partial t)_n = (1/\rho C_P)(-\partial F_n^{net}/\partial z_n), \quad (\text{C.3})$$

where the subscript  $n$  represents each layer.

Increasing the amount of atmospheric dust increases the amount of attenuation of the incident solar and thermal infrared fluxes and the amount of thermal infrared emission by dust. Figure C.2 shows shortwave, longwave, and net (shortwave + longwave) heating rates for the UDLM1 and Conrath dust profiles for total optical depths at the surface of 1.0, 2.0, and 5.0. In the Conrath profile the height of maximum deposition of solar energy,  $\tau_M$ , is controlled to first order by  $\tau_M \sim \cos(\theta_0)$ , where  $\theta_0$  is the solar zenith angle. A larger optical depth increases both the amount of solar energy absorption and the height of maximum deposition since under larger dust loading conditions,  $\tau_M \sim \cos(\theta_0)$  will occur at higher altitudes. *Within* the ULDMs, however, the maximum deposition of solar energy generally occurs at the dust number density maximum (Figure B.1(b) and Figure C.1(d)) under all optical depths (not shown). Thermal infrared emission by dust also increases with dust opacity, offsetting the absorption of solar energy in each dust profile, but absorption of solar energy is stronger than the thermal infrared emission and so there is increased net heating with increased column opacity.

The amount of dust in the upper atmospheric layers can have a profound impact on the radiative heating in the upper layers. As shown in Figure C.1, the higher a dust layer, the larger the heating because of the background atmospheric density. Increasing the dust number density in the upper layers in the ULDM profile, while keeping the total vertical optical depth constant, can also dramatically increase the upper layer heating. Increasing the mass mixing ratio at 10 km from  $1.43 \times 10^{-5}$  kg/kg to  $1.90 \times 10^{-5}$  kg/kg increases the maximum net heating rate (which occurs at 6 km) from 12.7 K/sol to 26.1 K/sol (Figure C.1(c)). Hence, a

dust layer in the upper atmosphere from either dust storm activity, boundary layer circulation, topographical influences, or scavenging processes (Heavens et al., 2011a) can potentially produce significant heating in the atmosphere. Mars GCMs that do not have an interactive dust scheme are likely to neglect the upper-layer heating which can be dynamically important. The circulations induced by dust heating can feed back and drive the atmospheric dust transport.

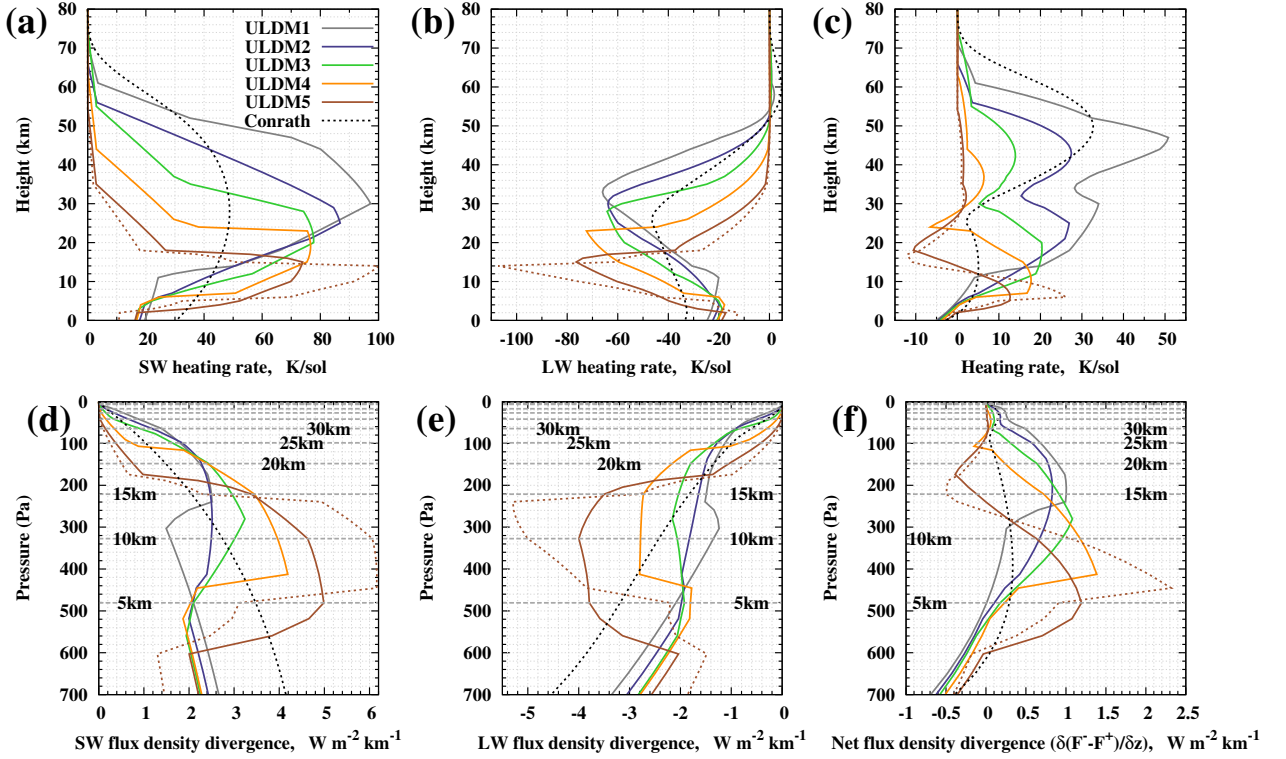


Figure C.1. Profiles of the (a) shortwave heating rate, (b) longwave heating rate, (c) net heating rate, (d) shortwave flux density divergence, (e) longwave flux density divergence, and (f) net flux density divergence, for the dust scenarios described in Figure B.1.  $R_{eff} = 1.7 \mu\text{m}$ ,  $\nu_{eff} = 0.3$ ,  $\varepsilon = 0.9$ ,  $T_G = 260 \text{ K}$ , and the cumulative dust optical depth at the surface is unity. For clarity, the divergences in the lower panel are shown as a function of pressure with 5-km incremental height levels shown.

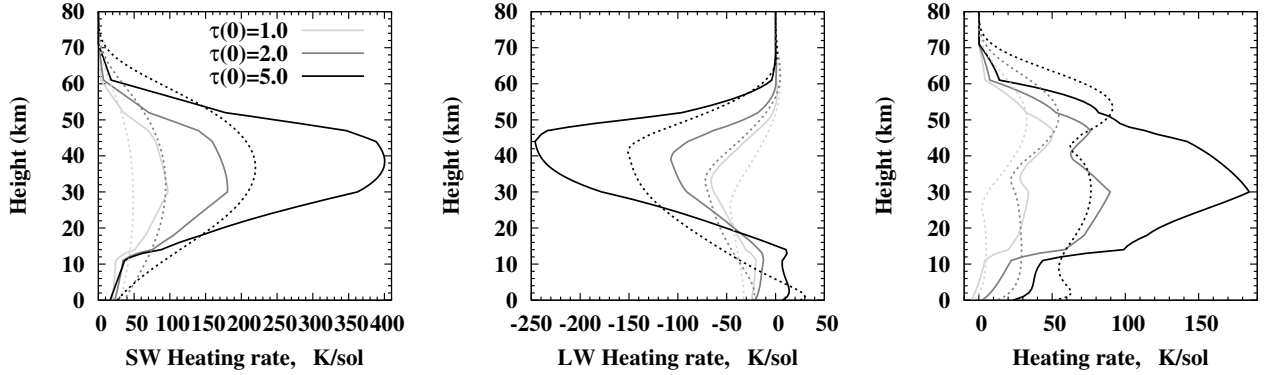


Figure C.2. a) Shortwave, (b) longwave, and (c) net heating rates of the ULDM1 (solid) and the Conrath (dashed) dust profiles for a total vertical optical depth at the surface of 1.0, 2.0 and 5.0.  $R_{eff} = 1.7 \mu\text{m}$ ,  $\nu_{eff} = 0.3$ ,  $\varepsilon = 0.9$ ,  $T_G = 260 \text{ K}$ .

## C.2 Sensitivities to the ground temperature and surface emissivity

In the context of this work, the relationship between the upward thermal infrared flux and the ground temperature ( $T_G$ ) and infrared surface emissivity ( $\varepsilon$ ) is relatively straightforward. Decreasing either the ground temperature or the emissivity decreases the energy in the atmosphere originating from the planet, resulting in a larger loss of energy through thermal emission by dust. The impact that an upper-level dust layer could have on the heating rates caused by these two parameters is presented here.

Dust transport changes the local and columnar optical thickness; either increasing or decreasing the amount of solar radiation reaching the surface, and thus either increasing or decreasing the ground temperature. Smith (2004) shows that a decrease in the globally averaged daytime surface temperature occurs during dust storms and a similar but smaller increase in the globally averaged nighttime surface temperature. The ground is usually warmer during daytime and cooler during nighttime than the atmospheric surface temperature. As stated in Section B.3.1 the temperature profile is fixed and has a surface temperature of 260 K. In this section, the ground temperatures is chosen to be below, at, and above the

atmospheric surface temperature which can be very loosely representative of nighttime, early morning, and afternoon conditions, respectively. Dust heating effects for nighttime ground and atmospheric temperatures are discussed in Section C.6.

Longwave heating rates resulting from  $T_G = 240$  K,  $T_G = 260$  K, and  $T_G = 280$  K are shown Figure C.3(a) for both the ULDM1 and Conrath profiles and the heating rate differences are given in Figure C.3(b); of course shortwave heating rates are unaffected. In the Conrath profile, the maximum difference between the  $T_G = 240$  K and  $T_G = 280$  K heating rates is at the surface level with a 73 K/sol difference where 1 sol is one 1 day on Mars. At the surface in the ULDM1 profile, the difference in heating is less with a difference of 48 K/sol. The large upward thermal infrared energy flux from a surface with  $T_G = 280$  K, causes an energy gain within the surface layers in both profiles through the absorption of thermal infrared energy (from the surface) by dust, resulting in surface layer atmospheric heating of 2 K/sol (ULDM1) and 7 K/sol (Conrath). On the other hand, the smaller thermal infrared energy flux from a surface with  $T_G = 240$  K, causes an energy loss at all levels in both profiles through stronger thermal infrared emission by dust and less absorption of thermal ground emission by dust. In the mid-layers, the difference between the  $T_G = 240$  K and  $T_G = 280$  K heating rates is larger in the ULDM1 profile than in the Conrath profile, and is comparable in magnitude to the ULDM1 surface heating difference with a maximum difference of 52 K/sol.

The effect of the ULDM is clearly observed: a dust layer at mid-levels (at 30 km in this case) increases the thermal infrared atmospheric cooling at mid-levels and decreases the cooling at lower levels compared to the classic dust profile. The mid-level thermal infrared cooling is further enhanced by lowering the ground temperature: lower ground temperatures provide less thermal infrared energy emitted from the ground to the atmosphere thereby decreasing the amount of thermal infrared energy gained via absorption by dust at all levels and particularly within the ULDM. In each  $T_G$  scenario, the ULDM1 heating rates are more negative at mid-levels and less negative at lower-levels than the Conrath heating rates. Thus,

atmospheric heating from ULDMs can be significantly different from atmospheric heating resulting from an assumption of well-mixed dust.

The surface redistribution of dust and the surface composition could impact the surface emissivity in the thermal infrared. Surface emissivities usually range from 0.9 to 1.0 in GCMs, but Hansen (1999) has shown that the surface infrared emissivity can be lower than 0.9 or 1.0 in the 20 – 50  $\mu\text{m}$  band in the southern and northern seasonal polar caps (composed primarily of  $\text{CO}_2$  ice). Therefore to observe any effect that this would have on the heating rates,  $\varepsilon_3$  is defined as the case with  $\varepsilon = 1.0$  in all longwave bands but with  $\varepsilon = 0.7$  in the 20 – 50  $\mu\text{m}$  band. The other two infrared emissivities are:  $\varepsilon_1 = 0.9$  and  $\varepsilon_2 = 1.0$  at all infrared wavelengths.

The longwave heating rates resulting from the three different emissivity scenarios and two different dust profiles are shown in Figure C.3(c) with the heating rate differences in Figure C.3(d). The difference between the  $\varepsilon_1$  and  $\varepsilon_2$  heating rates is larger than the difference between the  $\varepsilon_2$  and  $\varepsilon_3$  heating rates, however, the two differences are very similar and less than 5 K/sol. The difference between the  $\varepsilon_1$  and  $\varepsilon_3$  heating rates are on the order of 0.5 K/sol in both the Conrath and ULDM1 profiles. This means that a surface emissivity of 0.9 at all wavelengths affects that atmospheric heating rates similar to a surface emissivity of 1.0 with  $\varepsilon$  lowered to 0.7 in the 20 – 50  $\mu\text{m}$  band. Lowering the surface emissivity to 0.9 at all wavelengths or lowering the surface emissivity at the 20 – 50  $\mu\text{m}$  wavelengths ( $\varepsilon_3$ ) reduces the upward energy flux within the wavelength band(s), and therefore less energy is available for absorption by dust within all dust layers. Accounting for solid  $\text{CO}_2$  ice at the seasonal polar caps using lower emissivities at the 20 – 50  $\mu\text{m}$  wavelengths could affect the atmospheric heating in both profiles, however, the effects are small for our example.

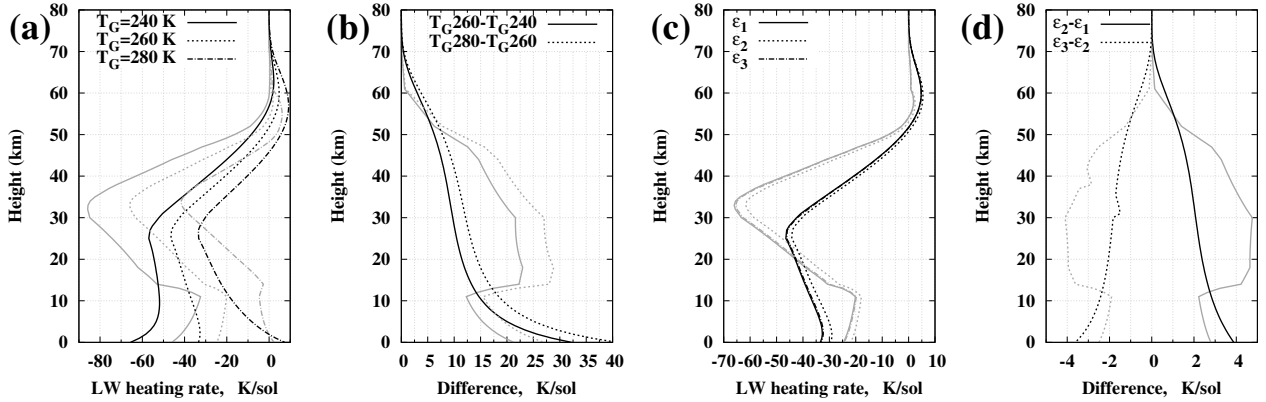


Figure C.3. Heating rate and difference profiles for the ULDM1 profile (grey) and Conrath profile (black). (a) longwave heating rates for different ground temperatures ( $T_G$ ); (b) the difference between the heating rates in (a); (c) longwave heating rates for different surface infrared emissivities:  $\epsilon_1 = 0.9$  in each longwave band,  $\epsilon_2 = 1.0$  in each longwave band, and  $\epsilon_3 = 1.0$  in each longwave band but with an emissivity of 0.7 within  $\lambda = 20 - 50 \mu\text{m}$ ; (d) the difference between the heating rates in (c).  $R_{eff} = 1.7 \mu\text{m}$ ,  $\nu_{eff} = 0.3$ , and the cumulative dust optical depth at the surface is unity.

### C.3 Sensitivities to the effective radius and effective variance

Altering the size distribution of dust, even while keeping the total vertical optical depth at the surface constant, may change the dust radiative heating. The effective radius of a size distribution is an area-weighted measure of the distribution’s mean arithmetic radius. Thus, from Equation B.1 the number of smaller dust particles increases as the effective radius *decreases*, and the number of larger dust particles increases as the effective radius increases. On the other hand, an increase of the effective variance, measuring the width of the distribution, would increase the number of both smaller and larger particles in the distribution while reducing the number at the median radius. A vertically-dependent size distribution in which the size-distribution’s first two moments decrease with height would additionally affect the heating rates, and is discussed in Section C.4.

Elteto and Toon (2010) find an annual, zonally averaged, global mean effective radius of

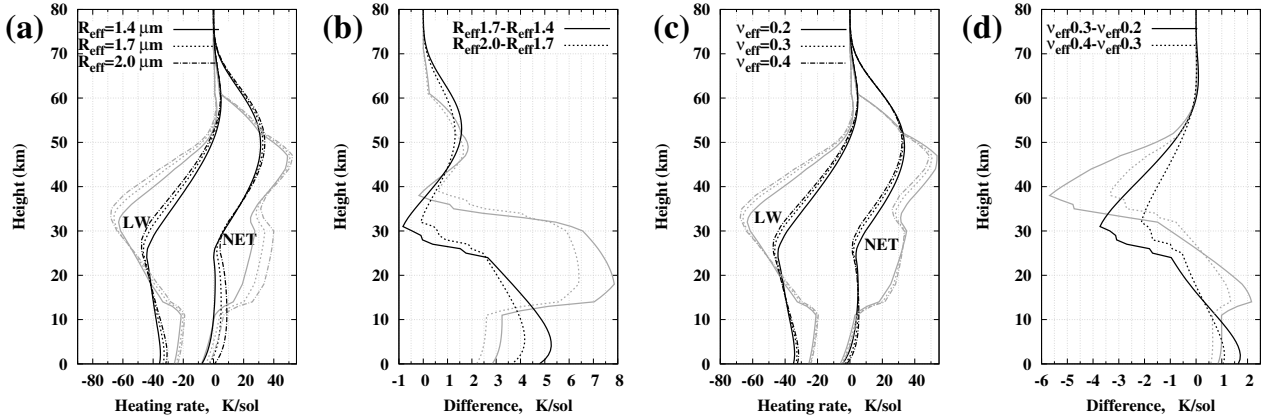


Figure C.4. Longwave (LW) and net (NET=LW+SW) heating rate and difference profiles for the ULDM1 profile (grey) and Conrath profile (black). (a) LW and NET heating rates for different effective radii ( $R_{eff}$ ); (b) the difference between the *net* heating in (a); (c) LW and NET heating rates for difference effective variances ( $\nu_{eff}$ ); (d) the difference between the *net* heating in (c).  $\varepsilon = 0.9$ ,  $T_G = 260$  K, and the cumulative dust optical depth at the surface is unity.

1.7  $\mu\text{m}$  (nearly that of the  $R_{eff} = 1.71 (+0.29/-0.26)$   $\mu\text{m}$  in Markiewicz et al. (1999)). From Thermal Emission Spectrometer observations taken during the 2001A global dust storm, they infer the dust effective radii to be as large as  $\sim 3$   $\mu\text{m}$  and as small as  $\sim 1$   $\mu\text{m}$ .

Figure C.4(a) shows the dust heating sensitivity to the effective radius of the distribution in both the net (NET) and longwave (LW) heating rates. The differences in the heating rates are given in Figure C.4(b). As in the different  $T_G$  and  $\varepsilon$  scenarios, the largest differences in the ULDM1 net heating rates occur roughly where the dust is most abundant in terms of dust number concentration. In Figure C.1(d), the maximum in the shortwave flux density divergence in the ULDM1 profile tends to be a secondary maximum at 15 – 20 km corresponding to the secondary maximum of dust number density (Figure B.1(b)). Whereas in the Conrath profile, the largest differences in the net heating rates occur near the height of maximum deposition of solar energy (in our case at  $\tau_M \sim 0.5$  neglecting scattering). The maximum differences between the  $R_{eff} = 1.7$   $\mu\text{m}$  and  $R_{eff} = 1.4$   $\mu\text{m}$  net heating rates are 5.3 K/sol (at 5 km; Conrath) and 7.9 K/sol (at 18 km; ULDM1), and between the  $R_{eff} = 2.0$   $\mu\text{m}$  and

$R_{eff} = 1.7 \mu\text{m}$  net heating rates the maximum differences are 4.2 K/sol (at 5 km; Conrath) and 6.4 K/sol (at 18 km; ULDM1).

More *smaller* dust particles exist in the distribution when the effective radius is  $R_{eff} = 1.4 \mu\text{m}$ , which can decrease the daytime atmospheric heating with a decrease in the SW heating rates (not shown) and a decrease (increase) in the lower (upper) atmosphere LW heating rates. In the ULDM1 and Conrath profiles, the maximum difference in net heating is mostly due to the shortwave heating rate differences. On a unit basis, smaller dust particles are less efficient absorbers of solar energy than larger dust particles. For example, in the  $0.55 - 5.0 \mu\text{m}$  band the absorption efficiencies are 6.4% for  $R_{eff} = 1.4 \mu\text{m}$  and 7.3% for  $R_{eff} = 1.7 \mu\text{m}$ . Thus, within the ULDM in the ULDM1 profile and in the lower layers in the Conrath profile, lowering  $R_{eff} = 1.7 \mu\text{m}$  to  $R_{eff} = 1.4 \mu\text{m}$ , decreases the amount of absorption of solar energy and decreases the shortwave heating rate.

Following Wolff and Clancy (2003) a dust effective variance is typically set between  $\nu_{eff} = 0.2$  (Tomasko et al., 1999) and  $\nu_{eff} = 0.4$  (Clancy et al., 1995), and in general agreement, Markiewicz et al. (1999) find a dust effective variance  $\nu_{eff} = 0.25 (+0.05/-0.1)$ . A standard upper limit of the effective variance is  $\nu_{eff}=0.3$  (Markiewicz et al., 1999; Wolff and Clancy, 2003). Comparative to the effective radius cases, Figures C.4(c) and C.4(d) show the LW and NET heating rates, and the net heating rate differences from the three effective variance values of 0.2, 0.3, and 0.4. Differences between the longwave heating rates mostly contribute to the differences in the net heating rates; for the  $\nu_{eff} = 0.2$  and  $\nu_{eff} = 0.4$  *net* heating rates, the maximum difference tends to occur near the maximum difference between the *longwave* cooling rates in the upper dust layers, the maximum heating rate differences between the  $\nu_{eff} = 0.2$  and  $\nu_{eff} = 0.4$  cases being 9 K/sol at 38 km (ULM1) and 6 K/sol at 31 km (Conrath).

The reason for the affected longwave heating and (somewhat) unaffected shortwave heating is not obvious. The longwave absorption efficiencies of a  $\nu_{eff} = 0.2$  distribution are

slightly larger than those of a  $\nu_{eff} = 0.4$  distribution: 61% (5.0 – 11.5  $\mu\text{m}$ ), 76% (11.5 – 20.0  $\mu\text{m}$ ), and 88% (20.0 – 200.0  $\mu\text{m}$ ) for  $\nu_{eff} = 0.2$  compared to 59% (5.0 – 11.5  $\mu\text{m}$ ), 73% (11.5  $\mu\text{m}$ ), and 85% (20.0–200.0  $\mu\text{m}$ ) for  $\nu_{eff} = 0.4$ . However, in the lower layers and in both dust profiles, more thermal infrared cooling is observed for smaller  $\nu_{eff}$ , which means that there is less absorption and more emission by dust in this case. The total number density of dust is larger for a  $\nu_{eff} = 0.2$  distribution having a unit surface optical depth. Atmospheric dust is itself emitting in the thermal infrared along with the surface, so in the lower layers emission is slightly stronger than absorption in the  $\nu_{eff} = 0.2$  case. For both the  $\nu_{eff} = 0.2$  and  $\nu_{eff} = 0.4$  distributions, there is a smaller amount of dust in the upper layers than in the lower layers in both dust profiles (Figure B.1(b)). This means less dust emission in the upper layers and emitted energy from below is more readily absorbed; the  $\nu_{eff} = 0.2$  distribution being a stronger absorber in the thermal infrared than the  $\nu_{eff} = 0.4$  distribution.

Clearly,  $\nu_{eff}$  has smaller impact on shortwave heating. Only a 0.1% – 0.2% difference between the shortwave absorption efficiencies of each distribution exists: 31.1% (0.1 – 0.55  $\mu\text{m}$ ) and 7.2% (0.55 – 5.0  $\mu\text{m}$ ) for the  $\nu_{eff} = 0.2$  distribution, and 31.2% (0.1 – 0.55  $\mu\text{m}$ ) and 7.4% (0.55 – 5.0  $\mu\text{m}$ ) for the  $\nu_{eff} = 0.4$  distribution. As the effective variance is a measure of the distribution’s width, it appears that increased absorption by larger particles compensates for the reduced absorption by smaller particles in the shortwave. As a result, most of the impact of  $\nu_{eff}$  on the net heating occurs in the longwave.

## C.4 Effects of linearly decreasing $R_{eff}$ and $\nu_{eff}$

Smaller dust particles have smaller mass and smaller sedimentation velocities, and are susceptible to transport by the resolved winds. Thus, smaller dust particles can be more readily lofted to higher altitudes in the Martian atmosphere compared to larger particles. Dust particles can also act as nuclei for ice formation, and the gravitational sedimentation

of both free dust particles and dust-core ice particles could cause the effective radius and effective variance of size-distributed dust to decrease with height. This raises the question: how would the heating rates be affected if the first two moments of the size distribution are altitude dependent? The optical depth would be strongly affected. Not only would the extinction coefficient of the size distribution become non-constant with height, but at higher altitudes, assuming that the effective radius would decrease with the height, the number of small particles could dramatically increase. For simplicity, the  $R_{eff}$  and  $\nu_{eff}$  are assumed to linearly decrease with height from  $R_{eff}(0) = 1.7 \mu\text{m}$  and  $\nu_{eff}(0) = 0.3$  to  $R_{eff}(80 \text{ km}) = 0.1 \mu\text{m}$  and  $\nu_{eff}(80 \text{ km}) = 0.001$ .

Figure C.5 shows the (a) ULDM1 and (b) Conrath heating rate profiles for the four combinations of  $R_{eff}(z)$  and  $\nu_{eff}(z)$ . The cases are distinguished as: (C1) the baseline with both  $R_{eff}$  and  $\nu_{eff}$  constant with height, (C2) both  $R_{eff}$  and  $\nu_{eff}$  linearly decrease with height, (C3)  $R_{eff}$  linearly decreases with height while  $\nu_{eff}$  is constant, and (C4)  $\nu_{eff}$  linearly decreases with height while  $R_{eff}$  is constant. The heating rate differences between the baseline and height-dependent case are shown in Figure C.5(c) for the ULDM1 profile and Figure C.5(d) for the Conrath profile.

The C4 heating rates differ only slightly to the C1 heating rates and the C3 heating rates differ only slightly from the C2 heating rates. This means that for both the ULDM and Conrath dust profiles, the decrease of the effective radius with height can have a large impact on the atmospheric heating, whereas the change of the effective variance with height has much less impact for our parameter space. The difference between the C1 and C3 heating rates can be as large as  $\sim 27 \text{ K/sol}$  (Conrath) and  $\sim 37 \text{ K/sol}$  (ULDM1) above 30 km, and the difference between the C1 and C4 heating rates are much smaller in comparison, as can be seen in Figure C.5(c,d). Considering the  $R_{eff}$  and  $\nu_{eff}$  sensitivities discussed in Section C.3 these differences are not surprising;  $R_{eff}$  affects both the longwave and shortwave heating via absorption, but  $\nu_{eff}$  mostly affects absorption in the longwave. Linearly decreasing the

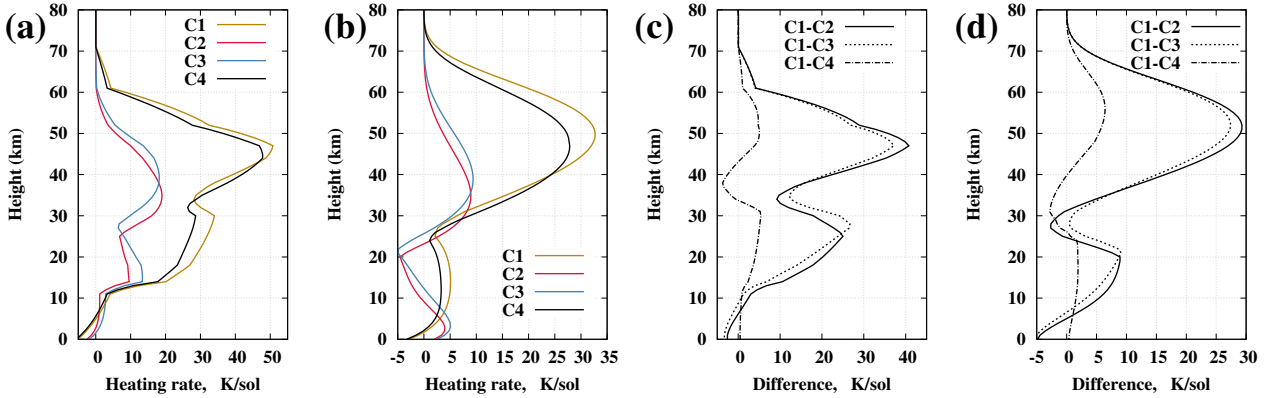


Figure C.5. The net heating rates of  $R_{eff}$  and  $\nu_{eff}$  linearly decreasing with height (respectively from  $R_{eff} = 1.7 \mu\text{m}$  and  $\nu_{eff} = 0.3$  at  $z = 0$  km to  $R_{eff} = 0.1 \mu\text{m}$  and  $\nu_{eff} = 0.001$  at 80 km) using the (a) ULDM1 profile, and the (b) Conrath profile. The difference between the altitude-dependent  $R_{eff}$  and  $\nu_{eff}$  cases are shown for the (c) ULDM1 and (d) Conrath profiles. C1:  $R_{eff}$ ,  $\nu_{eff}$  constant with height; C2:  $R_{eff}$ ,  $\nu_{eff}$  linearly decrease with height; C3:  $R_{eff}$  linearly decreases with height while  $\nu_{eff}$  is constant; C4:  $\nu_{eff}$  linearly decreases with height while  $R_{eff}$  is constant.  $\varepsilon = 0.9$ ,  $T_G = 260$  K, and the cumulative dust optical depth at the surface is unity.

effective radius with height effectively controls the vertical distribution of the dust size optical depth to contain fewer larger dust particles, and since larger dust particles are stronger absorbers of solar energy compared to smaller dust particles, the upper layer heating is decreased in the C2 and C3 cases. And in the lowest dust layers, the C1 heating rates are  $\sim 2.5$  K/sol (ULDM1) and  $\sim 5$  K/sol (Conrath) lower than the C2 heating rates, because of more absorption of solar energy in the upper layers in the C1 case.

## C.5 A single dust size versus a size distribution

GCMs lacked interactive dust schemes in the past, often using a single dust particle size to account for dust radiative heating. Obviously using a single dust size ignores the heating effects of both smaller and larger dust particles by not taking into account the differing optical properties which are inherently size dependent, but it was implicitly assumed that the effects will cancel or at least be negligible. Basu et al. (2004, 2006) took dust size representation in

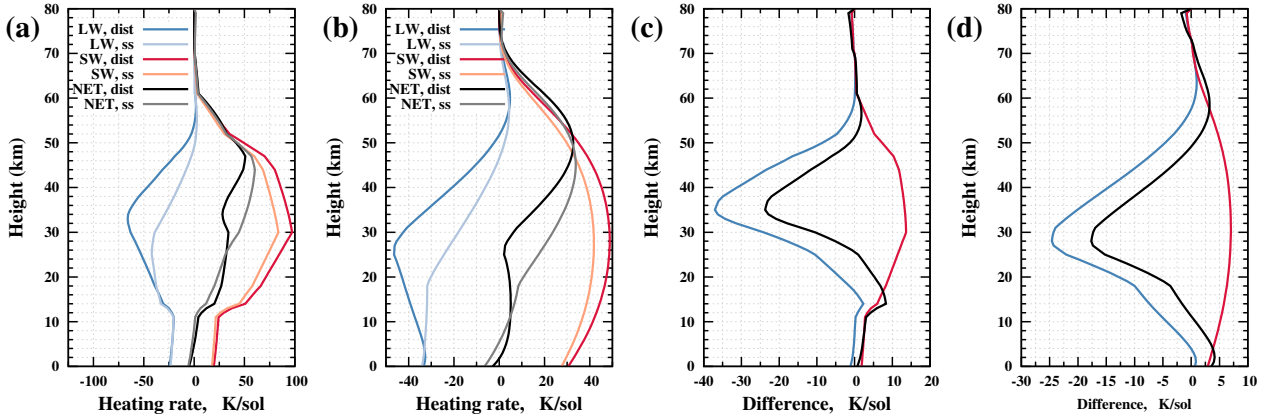


Figure C.6. Comparison between the single dust size (ss) and dust distribution (dist) heating rates using the (a) ULDM1 profile and (b) Conrath profile. The dust radius size bin from the log-normal distribution spans  $0.1 - 5.0 \mu\text{m}$  and the radius of the dust particle in the single-size case equals the effective radius ( $R_{eff} = 1.7 \mu\text{m}$ ) of the log-normal distribution. Net longwave heating (LW) is blue, net shortwave heating (SW) is red, and net heating (NET=LW+SW) is black. The difference between the longwave (blue), shortwave (red), and net (black) heating rates are shown in (c) for the ULDM4 and in (d) for the ULDM7 profiles.  $\varepsilon = 0.9$ ,  $T_G = 260 \text{ K}$ , and the cumulative dust optical depth at the surface is unity.

GCM modeling one step further, using two dust particle sizes to represent small and large dust, but use constant, size-independent optical properties for both sizes. The NASA Ames GCM has implemented interactive dust (Kahre et al., 2006), and addressed the evolution of dust particle sizes using 10 dust size bins in Kahre et al. (2008). And most recently, Madeleine et al. (2011) have implemented a semi-interactive dust scheme in the LMD GCM which predicts the vertical distribution and dust particle size, thereby allowing size-dependent calculation of the optical properties. While current GCMs have evolved from the practice of using a single dust size to using a dust distribution, it is still relevant to provide the differences in the heating impact, particularly between two dissimilar vertical dust profiles, to remain aware of the potential biases in single-size dust representation. In this section the potential differences in atmospheric heating by single-size and size-distributed dust are presented.

Figures C.6(a) and C.6(b) give the ULDM1 and Conrath longwave, shortwave, and net

heating rate profiles, respectively, of a single  $1.7 \mu\text{m}$  dust radius size and of a size distribution with an effective radius of  $R_{eff} = 1.7 \mu\text{m}$ . In both the ULDM1 and Conrath profiles, the single dust size overestimates (underestimates) net heating in the upper (lower) dust layers. Shortwave heating is underestimated in all dust layers when a single-size is used, whereas longwave cooling roughly follows the same pattern as the net heating with the longwave cooling being underestimated in the upper layers and nearly similar to longwave size-distributed cooling in the lowest dust layers. The differences between the longwave, shortwave, and net heating rates are given in Figures C.6(c) and C.6(d) for the ULDM1 and Conrath profiles, respectively. Only the longwave heating will apply for nighttime conditions and it is clear that the size-difference impact is larger in the longwave.

Both the vertical distribution and optical properties ultimately account for the difference between the single-size and size-distribution heating rates. Dust is vertically distributed the same way for both the single-size and size distribution cases, but in both cases imposing a unitary cumulative optical depth (at  $0.6 \mu\text{m}$ ) requires a different number density at the surface. In other words, since the extinction coefficients of the single-size and size-distribution differ, the mass mixing ratio is adjusted at the surface (and hence so is the number density) in both cases in order to maintain a unit cumulative optical depth. At a wavelength of  $0.6 \mu\text{m}$ , the extinction cross-section of the size distribution is  $3.66 \times 10^{-11} \text{ m}^2$  which is larger than the single-size ( $1.7 \mu\text{m}$ ) extinction cross-section of  $2.32 \times 10^{-11} \text{ m}^2$ . Thus, the number density of the single-size dust is greater than the number density of the size distribution at all levels. Moreover, within all dust layers there are more  $1.7 \mu\text{m}$  size particles in the single-size case, but there are also more particles larger than  $1.7 \mu\text{m}$  in the size distribution case. Dust particles larger than  $1.7 \mu\text{m}$  are stronger absorbers of solar energy and stronger scatterers of thermal infrared energy compared to  $1.7 \mu\text{m}$  sized particles. For example, in the  $0.55 - 5.0 \mu\text{m}$  shortwave band absorption efficiencies are 6.6% ( $r = 1.7 \mu\text{m}$ ) and 11.6% ( $r = 3.5 \mu\text{m}$ ), and in the  $11.5 - 20.0 \mu\text{m}$  band scattering efficiencies are 1.4% ( $1.7 \mu\text{m}$ ) and

37% ( $3.5 \mu\text{m}$ ). Thus, the absorption efficiencies of the size distribution are larger in the shortwave and smaller in the longwave than those of the single-size dust: 31% ( $\lambda_1$ ), 7.3% ( $\lambda_2$ ), 60% ( $\lambda_3$ ), 74% ( $\lambda_4$ ), and 86% ( $\lambda_5$ ) for the  $1.7 \mu\text{m}$  size-distribution, and 30% ( $\lambda_1$ ), 6.6% ( $\lambda_2$ ), 68% ( $\lambda_3$ ), 86% ( $\lambda_4$ ), and 95% ( $\lambda_5$ ) for the  $r = 1.7 \mu\text{m}$  single size dust. The size-distribution and single-size is more absorptive in the  $\lambda_1$  and  $\lambda_2$  band than the single-size dust, but more solar energy is deposited in the  $\lambda_2$  band ( $F^-(0) \sim 225 \text{ W m}^{-2}$ ) than in the  $\lambda_1$  band ( $F^-(0) \sim 75 \text{ W m}^{-2}$ ). In the longwave, more absorption takes place in the lower layers by single-size dust compared to the size-distributed dust since the single-size absorption efficiency is larger than the size-distribution absorption efficiency. However, in the single-size dust case, the larger number of dust particles also means more thermal infrared energy emission. The single-size thermal absorption seems to compensate the thermal emission making the single-size and size-distribution longwave flux divergences similar. The larger amount of single-size dust at all height-levels, but particularly in the lower levels, means more energy is available for absorption in the upper dust layers. In the upper layers absorption of the emitted flux from below is stronger in the single-size case than in the size-distributed case, since the single-size upward flux is larger than the size-distributed upward flux, e.g., at 28 km in the ULDM case, the single-size upward thermal infrared flux is  $223 \text{ W m}^{-2}$  as opposed to the size-distribution upward thermal infrared flux of  $203 \text{ W m}^{-2}$ , and at 18 km in the Conrath case, the single-size upward thermal infrared flux is  $229 \text{ W m}^{-2}$  as opposed to the size-distribution upward thermal infrared flux of  $212 \text{ W m}^{-2}$ . In the upper layers, more thermal infrared absorption by the single-size dust than by the size-distribution dust means that single-size dust underestimates the size-distribution cooling.

In the upper layers (but below 50 km) in both profiles, the single-size net heating tends to overestimate the distribution net heating by a maximum of  $\sim 23 \text{ K/sol}$  (ULDM1) and  $18 \text{ K/sol}$  (Conrath). Dust emission in the upper layers is less in the single-size case (meaning less cooling) and largely contributes to the overestimation of net heating in the uppers below

50 km. The underestimation of shortwave heating is less of a factor except for the lowermost and uppermost dust layers where it tends to cause an underestimation in the net heating rates. The pronounced difference between the single-size and size-distribution heating rate profiles, resulting ultimately from the difference in optical properties, reinforces the necessity of predicting dust sizes and coupling the dust distribution to radiative transfer calculations in GCM modelling studies.

## C.6 Dust impacts under nighttime temperature conditions

Martian ground temperatures are much cooler at night than daytime ground temperatures and typically range between 150 K to 210 K. Nighttime heating rate profiles of both vertical dust distributions are similar to the daytime heating rate profiles. While thermal infrared cooling will be diminished at nighttime due to decreased energy emission from the colder surface, the heating rate impacts from different ground temperatures tend to be larger in magnitude compared to the daytime heating rate impacts. Moreover, it would be expected that the nighttime impacts of the different dust distributions are smaller since the size distribution parameters have an additional impact in the shortwave.

Figures C.7(a) and C.7(b) shows the longwave heating rates of three nighttime surface temperatures along with the differences between the heating rates, respectively (note that the nighttime atmospheric lapse rate is general and assumes no temperature inversion, being linearly fixed from 190 K at the surface to 105 K at 80 km). Treating  $T_G = 190$  K and  $T_G = 260$  K respectively as the nighttime and daytime baseline cases, the nighttime impacts of decreasing and increasing the ground temperature on the atmospheric heating rates can be compared to the daytime impacts. At the surface level,  $T_G = 210$  K results in a 125%

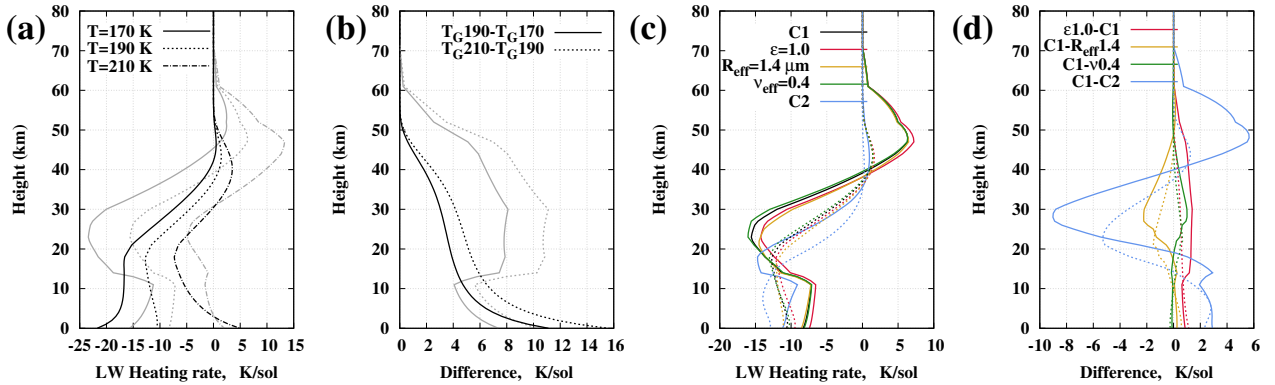


Figure C.7. Nighttime conditions. (a) Longwave heating rates for different ground temperatures ( $T_G$ ) with the Conrath dust profile (black) and the ULDM1 dust profile (grey); (b) the difference between the heating rates produced by the different ground temperatures. In (a) and (b),  $\varepsilon = 0.9$ , and  $R_{eff} = 1.7 \mu\text{m}$  and  $\nu_{eff} = 0.3$  (constant with height). (c) Longwave heating rates for: C1 (same as the  $T_G = 190 \text{ K}$  case in (a)), C1 but for an infrared surface emissivity of 1.0, C1 but for an effective radius of  $1.4 \mu\text{m}$ , C1 but for an effective variance of 0.4, and C1 but for the effective radius and effective variance decreasing with height; (d) the difference between the heating rates of the cases in (c). In (c) and (d) the ULDM1 profile is solid and the Conrath profile is dashed. The cumulative dust optical depth at the surface is unity.

(ULDM1) and 147% (Conrath) increase in heating rate, larger than during daytime where  $T_G = 280 \text{ K}$  results in increases of 109% (ULDM1) and 122% (Conrath). Decreasing  $T_G$  to 170 K results in surface-level heating rate decreases of 89% (ULDM1) and 105% (Conrath) compared to the  $T_G = 240 \text{ K}$  daytime surface-level heating rate decreases of 86% (ULDM1) and 96% (Conrath). As an example at mid-levels in the ULDM1 case, lowering the ground temperature to 170 K decreases the heating rate by 51% at the height of maximum cooling (23 km) and raising the ground temperature to 210 K increases the heating rate by 70%. These mid-level nighttime impacts are comparably larger than the daytime impacts at the height of maximum cooling (ULDM1 case at 23 km):  $T_G = 240 \text{ K}$  results in a 30% heating rate decrease and  $T_G = 280 \text{ K}$  results in a 37% increase. While the nighttime heating rates are smaller than the daytime heating rates, the physical impact of the ground temperature on the atmospheric heating is larger than the daytime impact.

Nighttime heating rates and heating rate differences of different dust configurations are given in Figures C.7(c) and C.7(d). With the baseline case denoted as C1, the impact of each dust configuration under nighttime temperature conditions to the daytime impacts is compared. While the surface emissivity affects the thermal infrared heating rates only, the shortwave heating will increase the net heating making the relative net heating rate changes larger in the daytime than in the nighttime. Increasing the surface emissivity to 1.0 increases the nighttime heating rate by 10% (ULDM1) and 11% (Conrath) at the surface level, and by 9% (ULDM1) and 5% (Conrath) at the height of maximum cooling. While increasing  $\varepsilon$  to 1.0 during daytime, the surface level increases are 55% (ULM1) and 135% (Conrath) and the mid-level increases are 15% (ULDM1) and 51% (Conrath). During daytime, the effective radius and effective variance of the distribution affect both shortwave and longwave heating rates. As such, the daytime impacts of  $R_{eff}$  and  $\nu_{eff}$  tend to be larger than the nighttime impacts. For example, in the ULDM1 profile at the height of maximum cooling,  $R_{eff} = 1.4 \mu\text{m}$  increases the (negative) nighttime heating rate by 10% and decreases the positive daytime heating rate by 14%;  $\nu_{eff} = 0.4$  decreases the nighttime heating by 4% and decreases the positive daytime heating rate by 5%. The significant reduction in the mid- and upper-level daytime heating (Section C.4) upon linearly decreasing the first two moments of the distribution with height is mostly due to reduction of the absorption of solar energy.

## Appendix D

# Global and Zonal Averages of Soluble Aersosol Number Densities

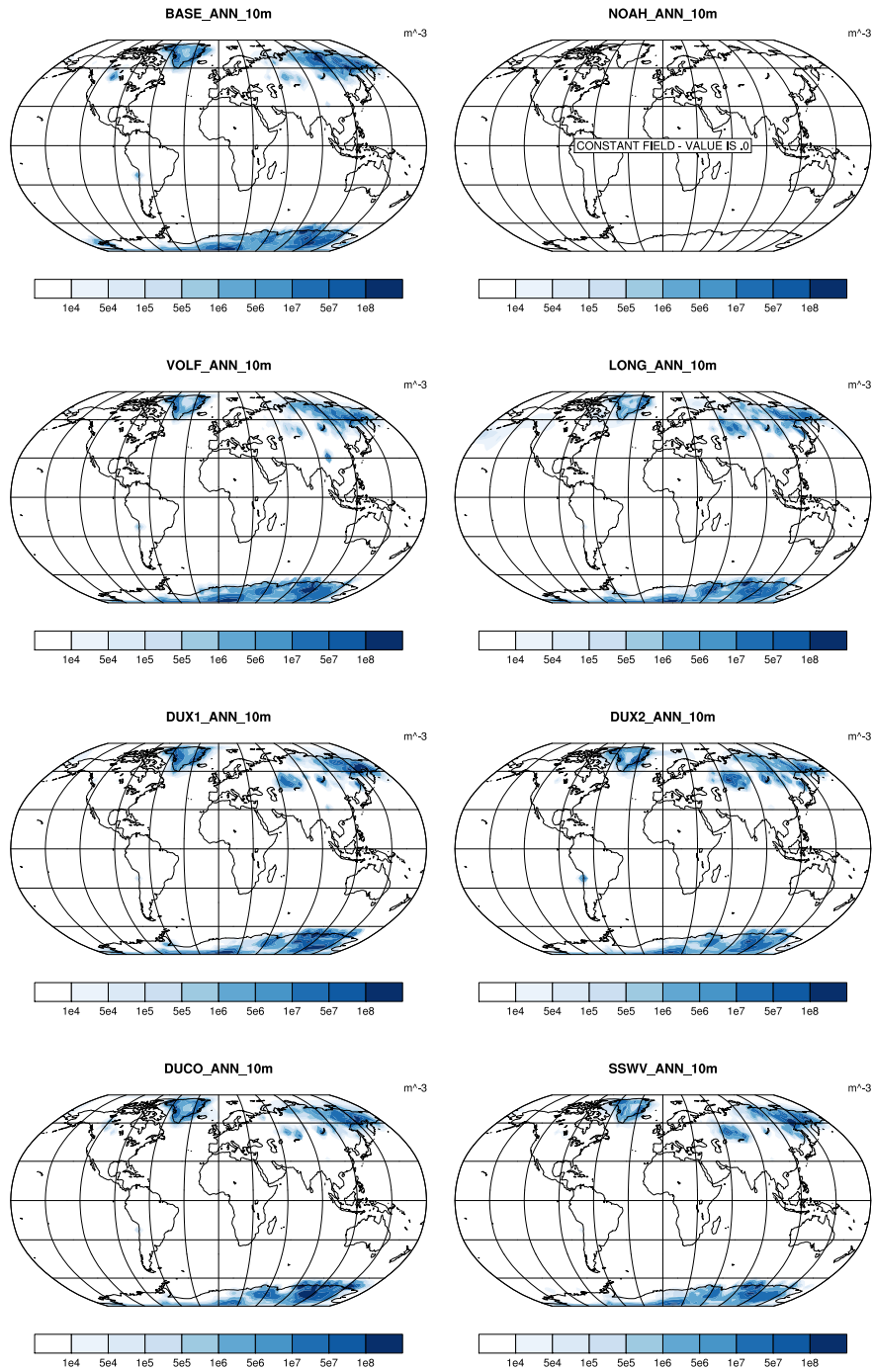


Figure D.1. 10 m mode 1 aerosol number density ( $\text{m}^{-3}$ ) averaged over 2012 for BASE, NOAH, VOLF, LONG, DUX1, DUX2, DUCC, and SSWV experiments.

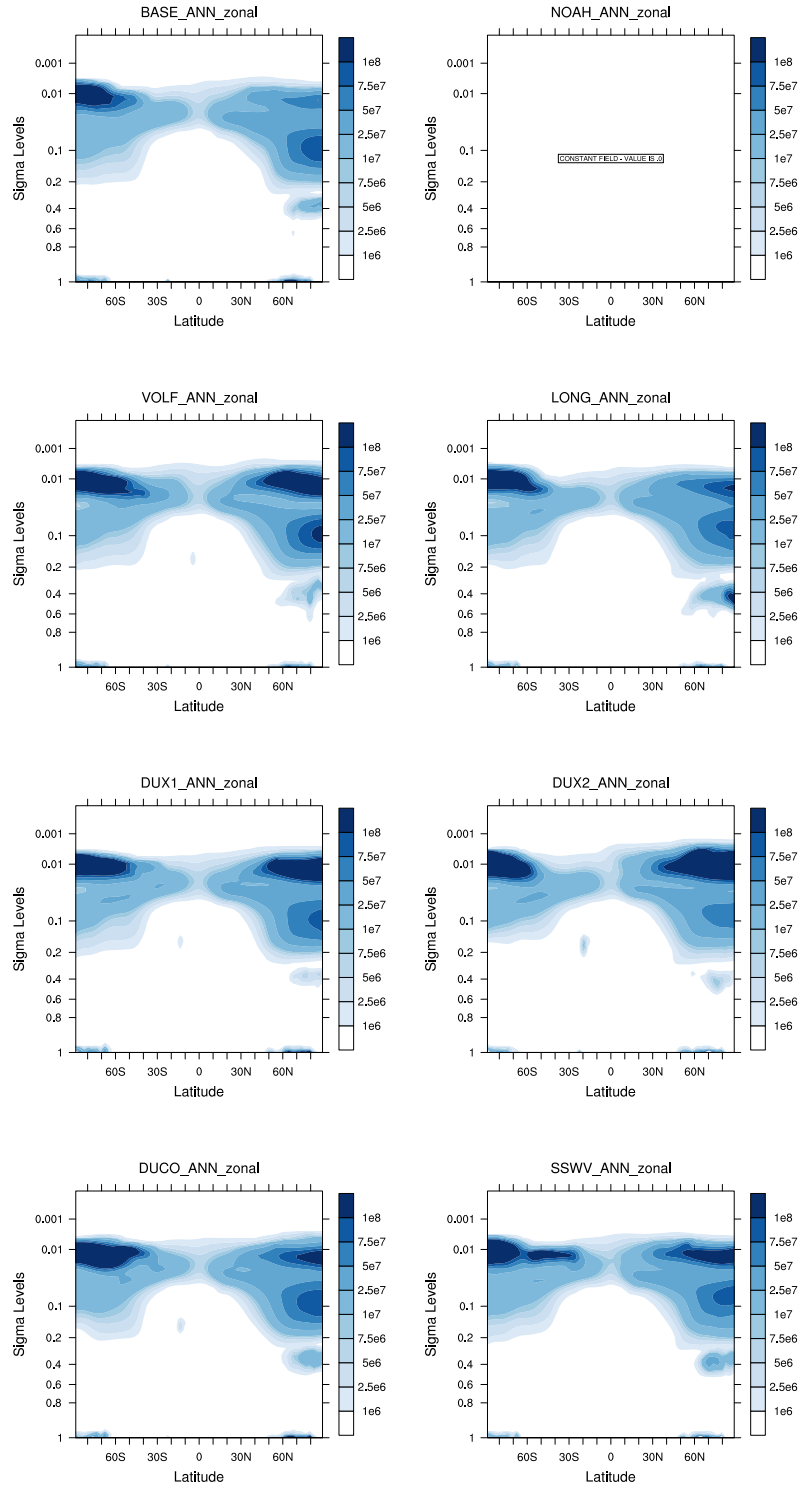


Figure D.2. 2012 zonally averaged mode 1 aerosol number density ( $m^{-3}$ ) for BASE, NOAH, VOLF, LONG, DUX1, DUX2, DUCO, and SSWV experiments.

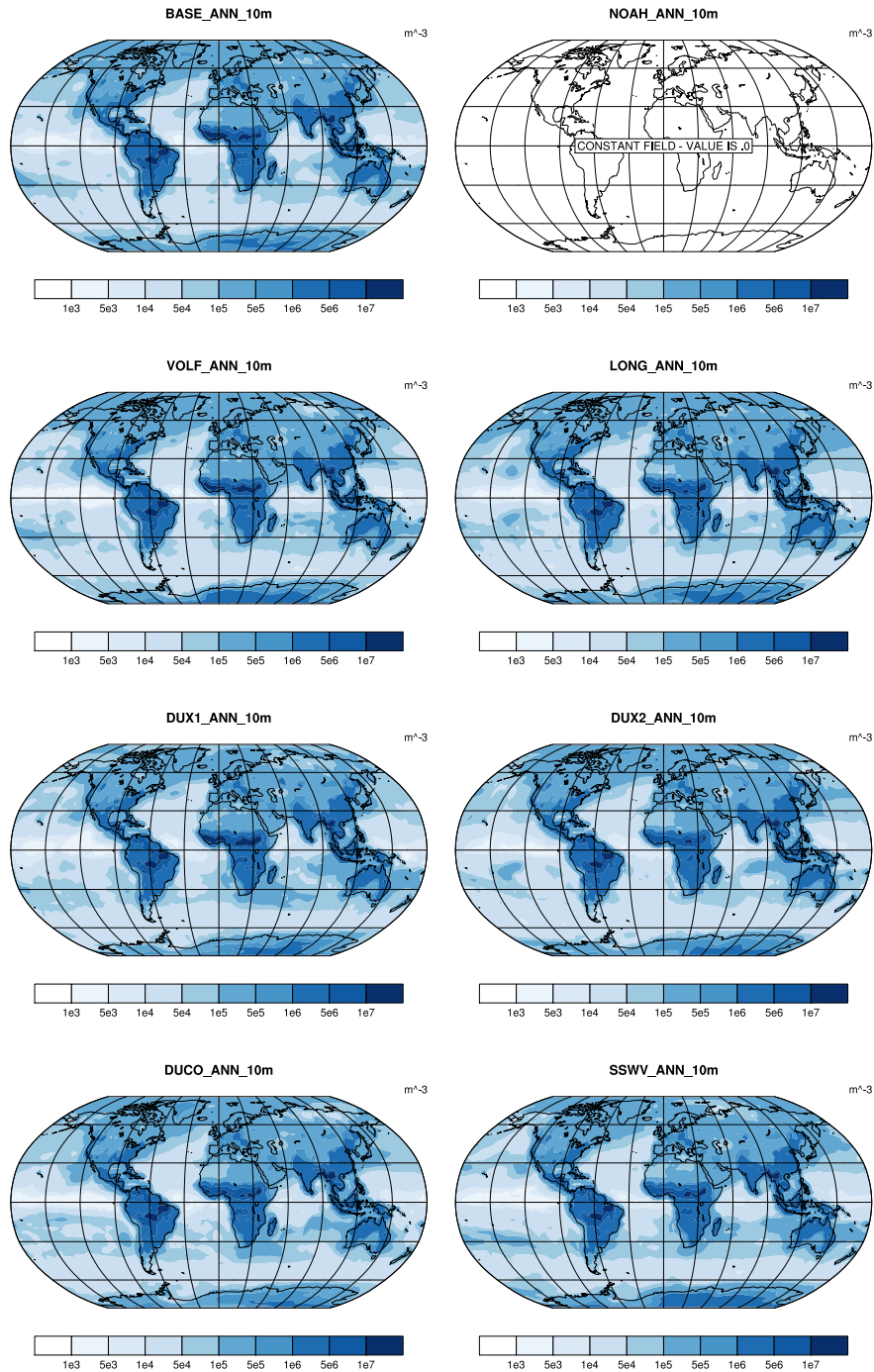


Figure D.3. 10 m mode 2 aerosol number density ( $\text{m}^{-3}$ ) averaged over 2012 for BASE, NOAH, VOLF, LONG, DUX1, DUX2, DUCCO, and SSWV experiments.

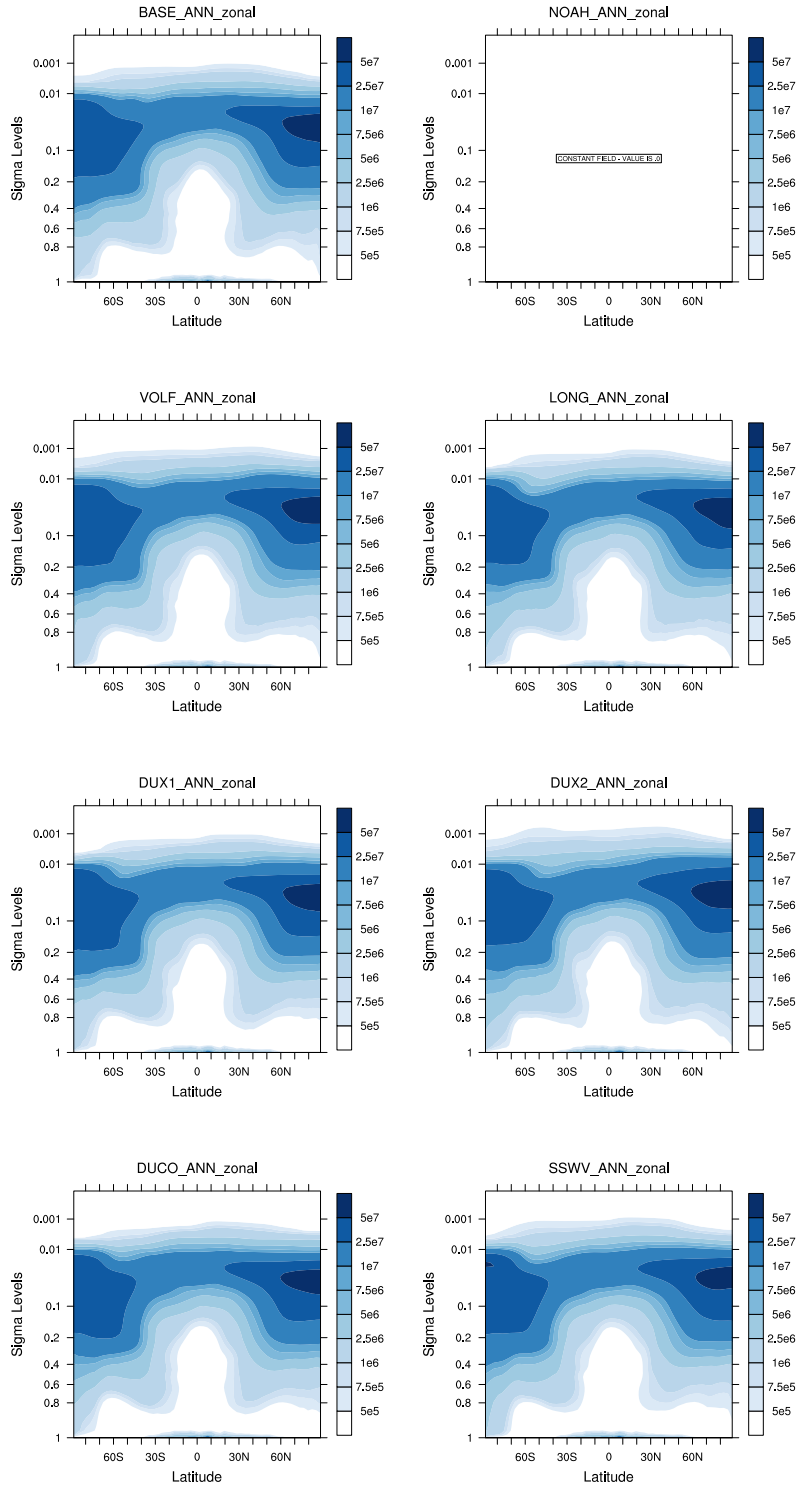


Figure D.4. 2012 zonally averaged mode 2 aerosol number density ( $m^{-3}$ ) for BASE, NOAH, VOLF, LONG, DUX1, DUX2, DUCO, and SSWV experiments.

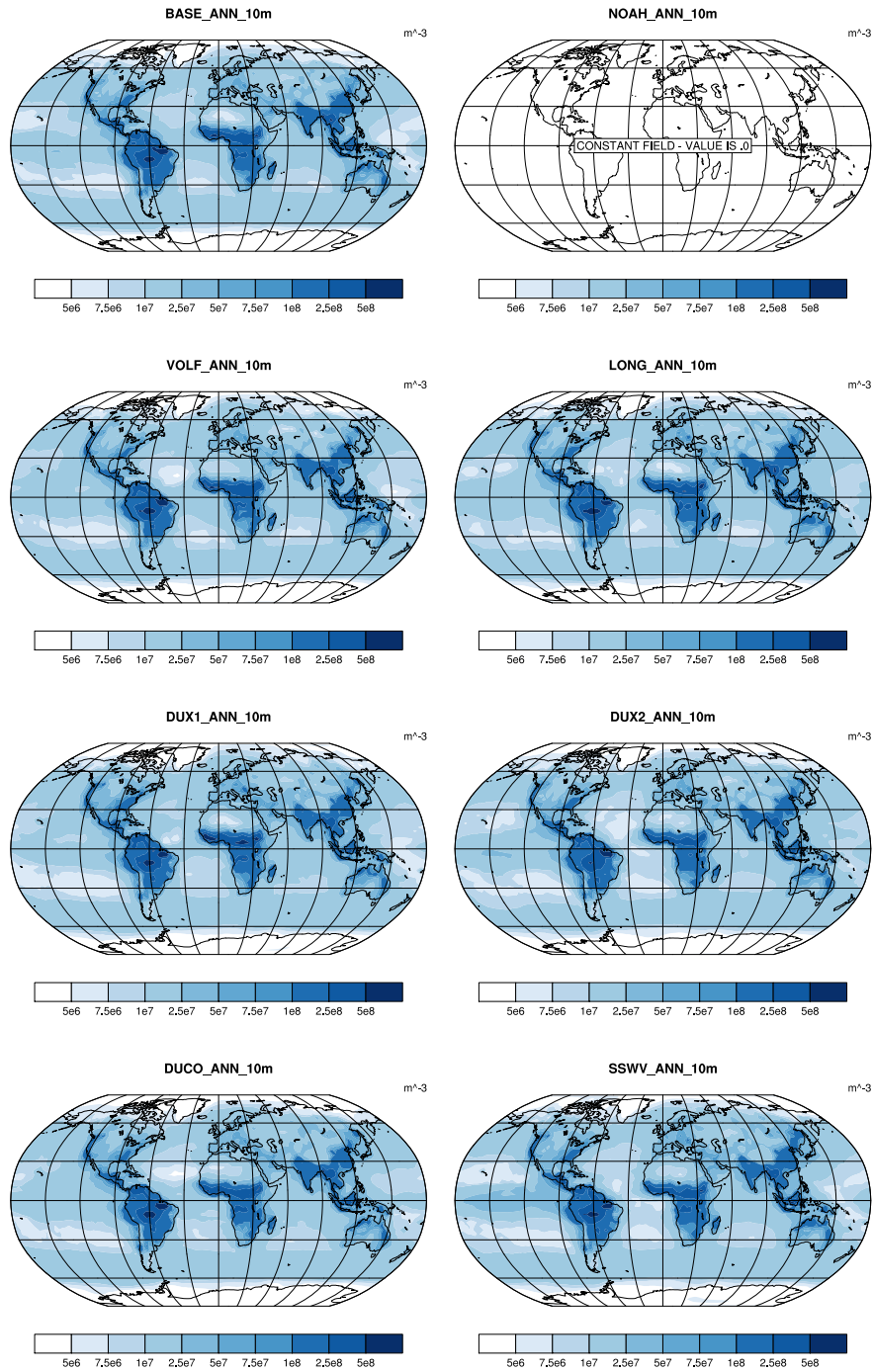


Figure D.5. 10 m mode 3 aerosol number density ( $\text{m}^{-3}$ ) averaged over 2012 for BASE, NOAH, VOLF, LONG, DUX1, DUX2, DUCC, and SSWV experiments.

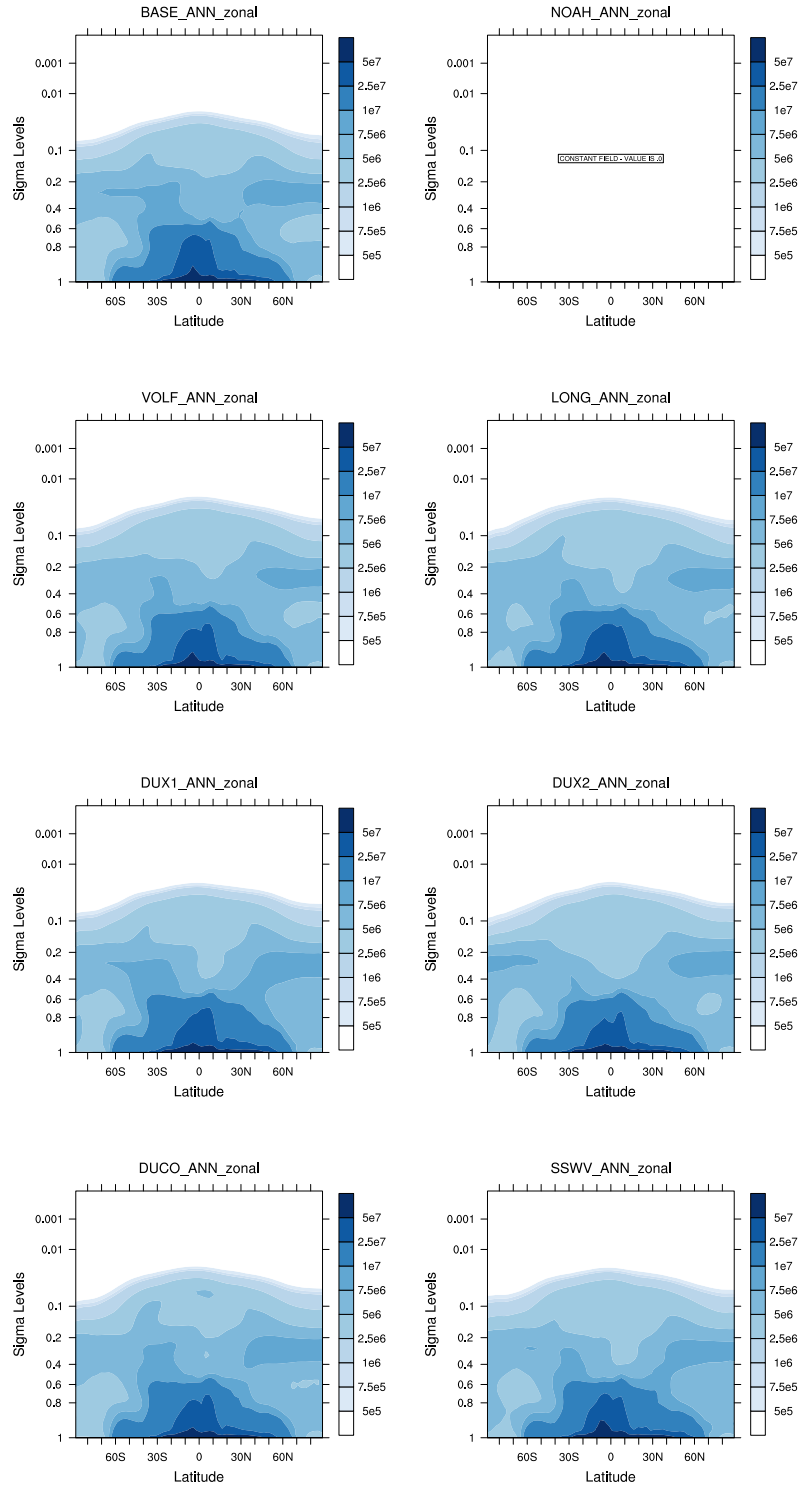


Figure D.6. 2012 zonally averaged mode 3 aerosol number density ( $m^{-3}$ ) for BASE, NOAH, VOLF, LONG, DUX1, DUX2, DUCO, and SSWV experiments.

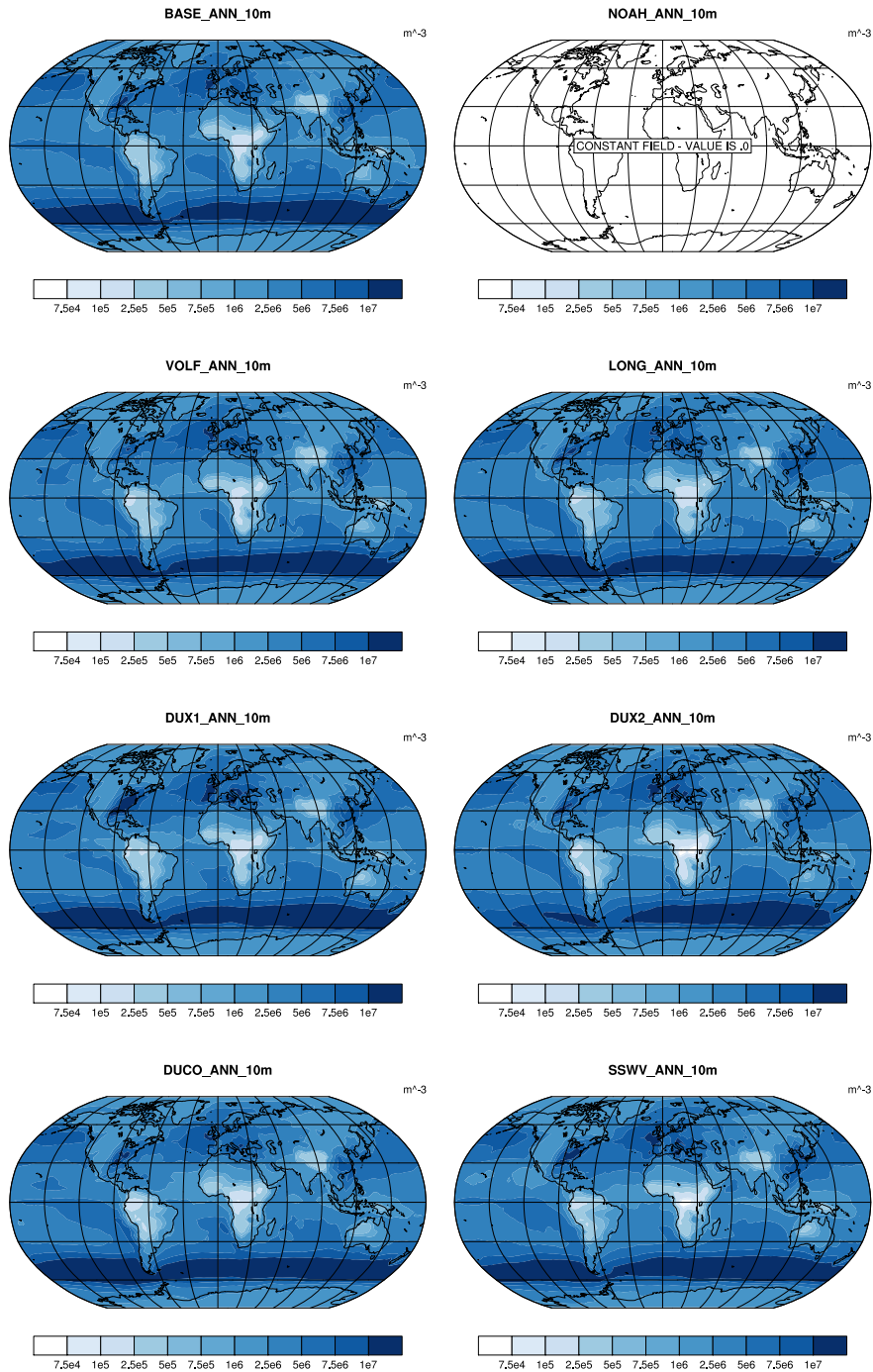


Figure D.7. 10 m mode 4 aerosol number density ( $\text{m}^{-3}$ ) averaged over 2012 for BASE, NOAH, VOLF, LONG, DUX1, DUX2, DUCCO, and SSWV experiments.

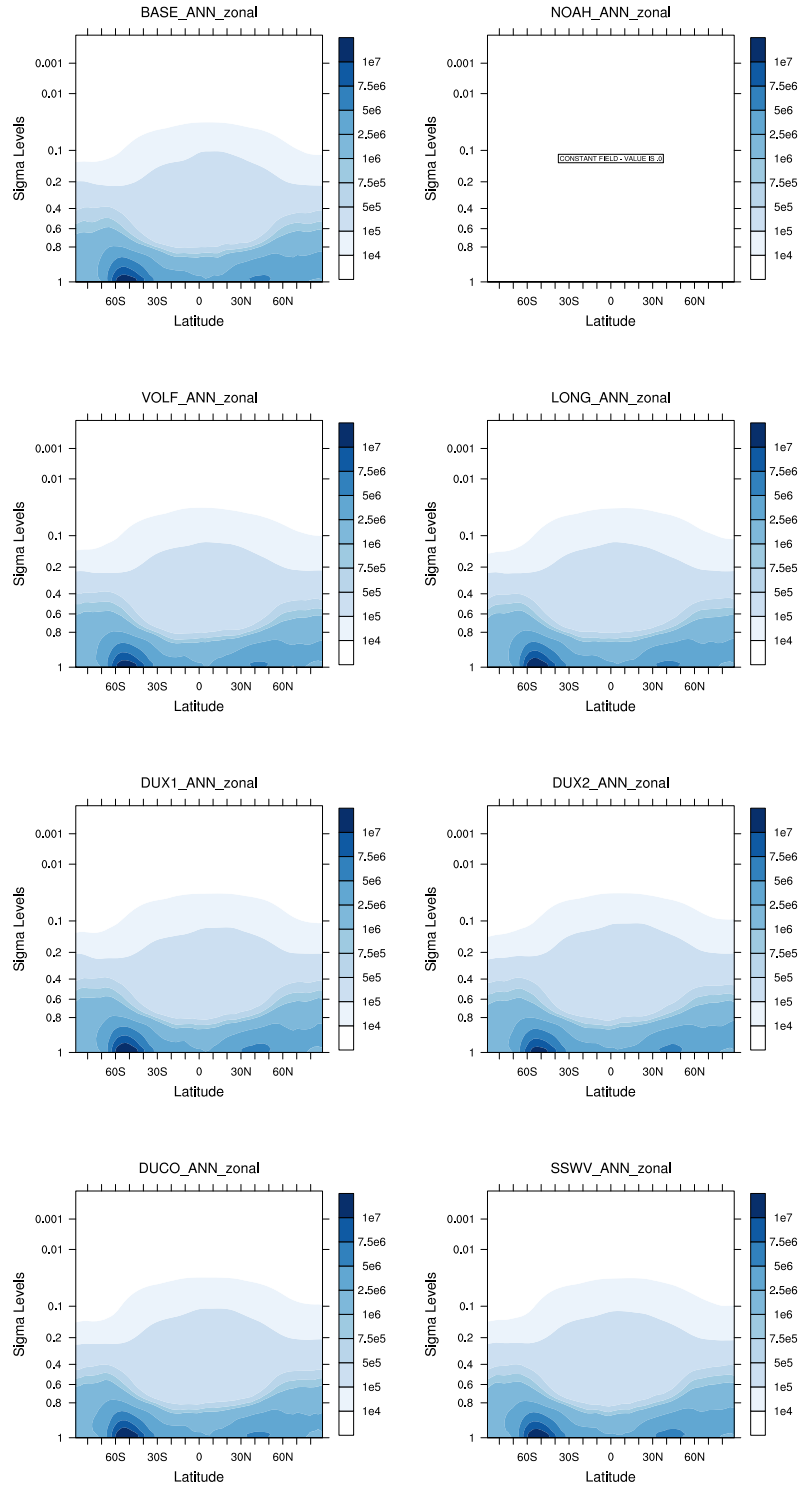


Figure D.8. 2012 zonally averaged mode 4 aerosol number density ( $m^{-3}$ ) for BASE, NOAH, VOLF, LONG, DUX1, DUX2, DUCO, and SSWV experiments.

# Appendix E

## Global and Zonal Averages of Insoluble Aerosol Number Densities

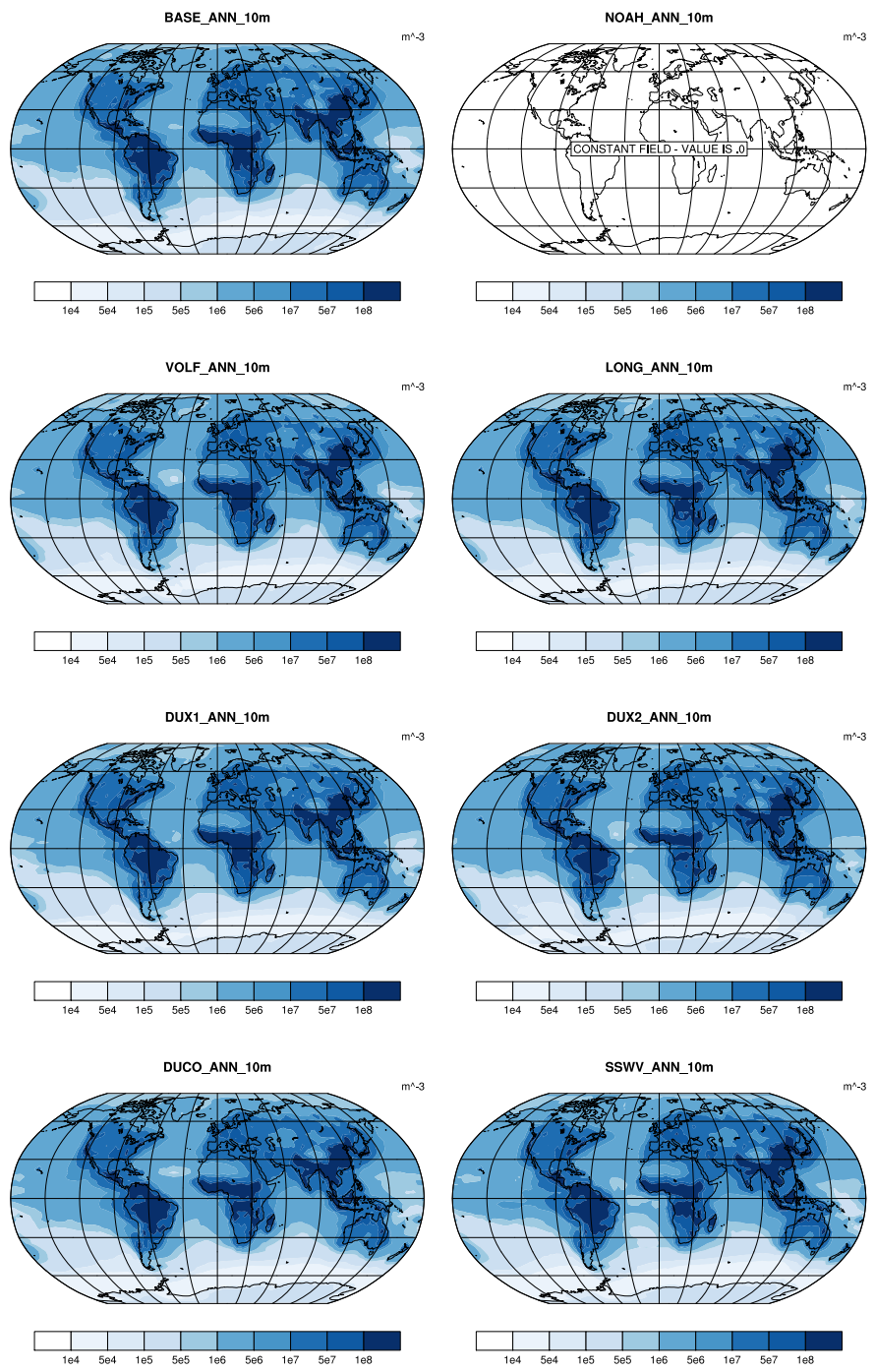


Figure E.1. 10 m mode 5 aerosol number density ( $m^{-3}$ ) averaged over 2012 for BASE, NOAH, VOLF, LONG, DUX1, DUX2, DUCCO, and SSWV experiments.

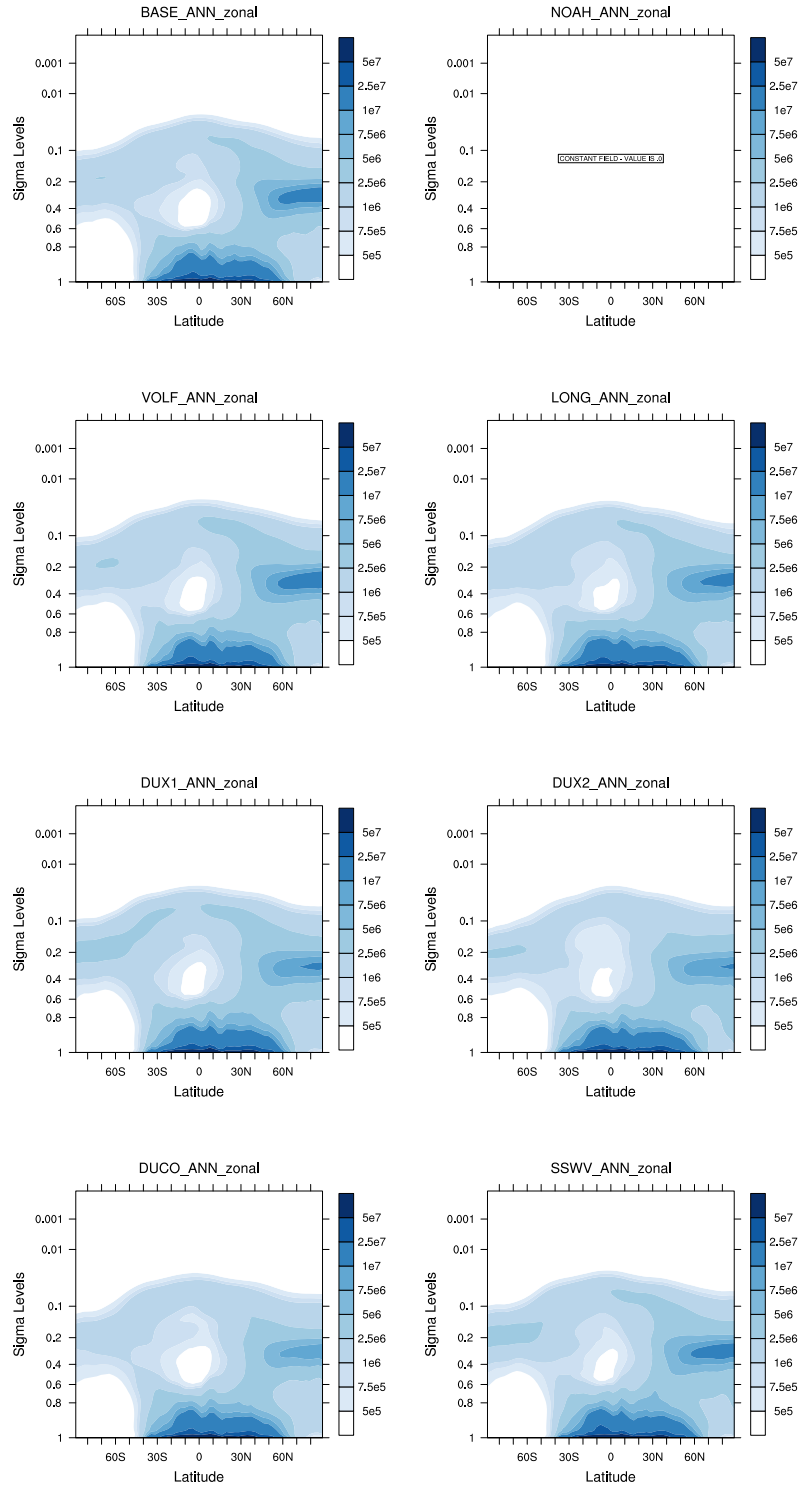


Figure E.2. 2012 zonally averaged mode 5 aerosol number density ( $\text{m}^{-3}$ ) for BASE, NOAH, VOLF, LONG, DUX1, DUX2, DUCO, and SSWV experiments.

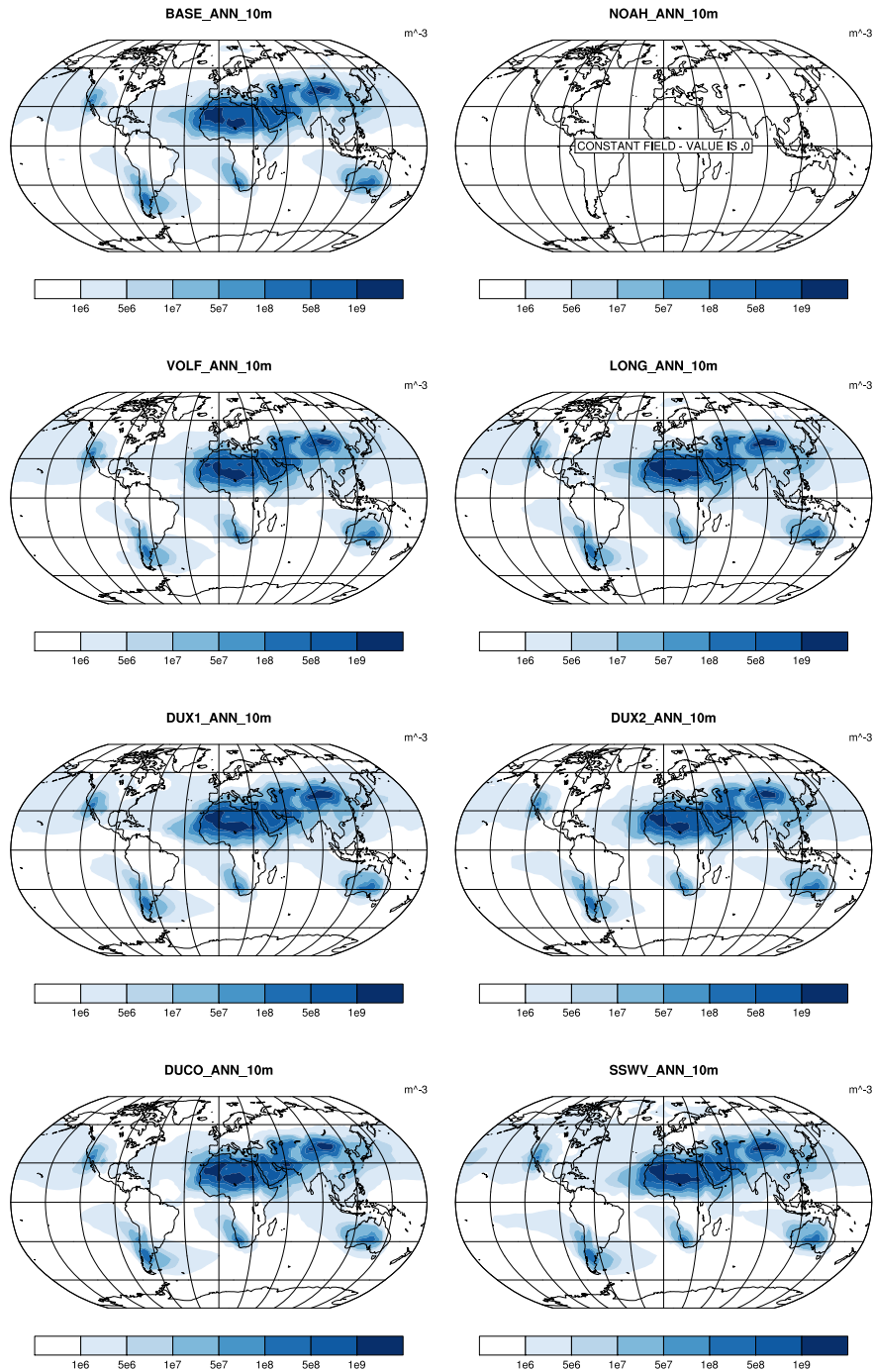


Figure E.3. 10 m mode 6 aerosol number density ( $\text{m}^{-3}$ ) averaged over 2012 for BASE, NOAH, VOLF, LONG, DUX1, DUX2, DUCC, and SSWV experiments.

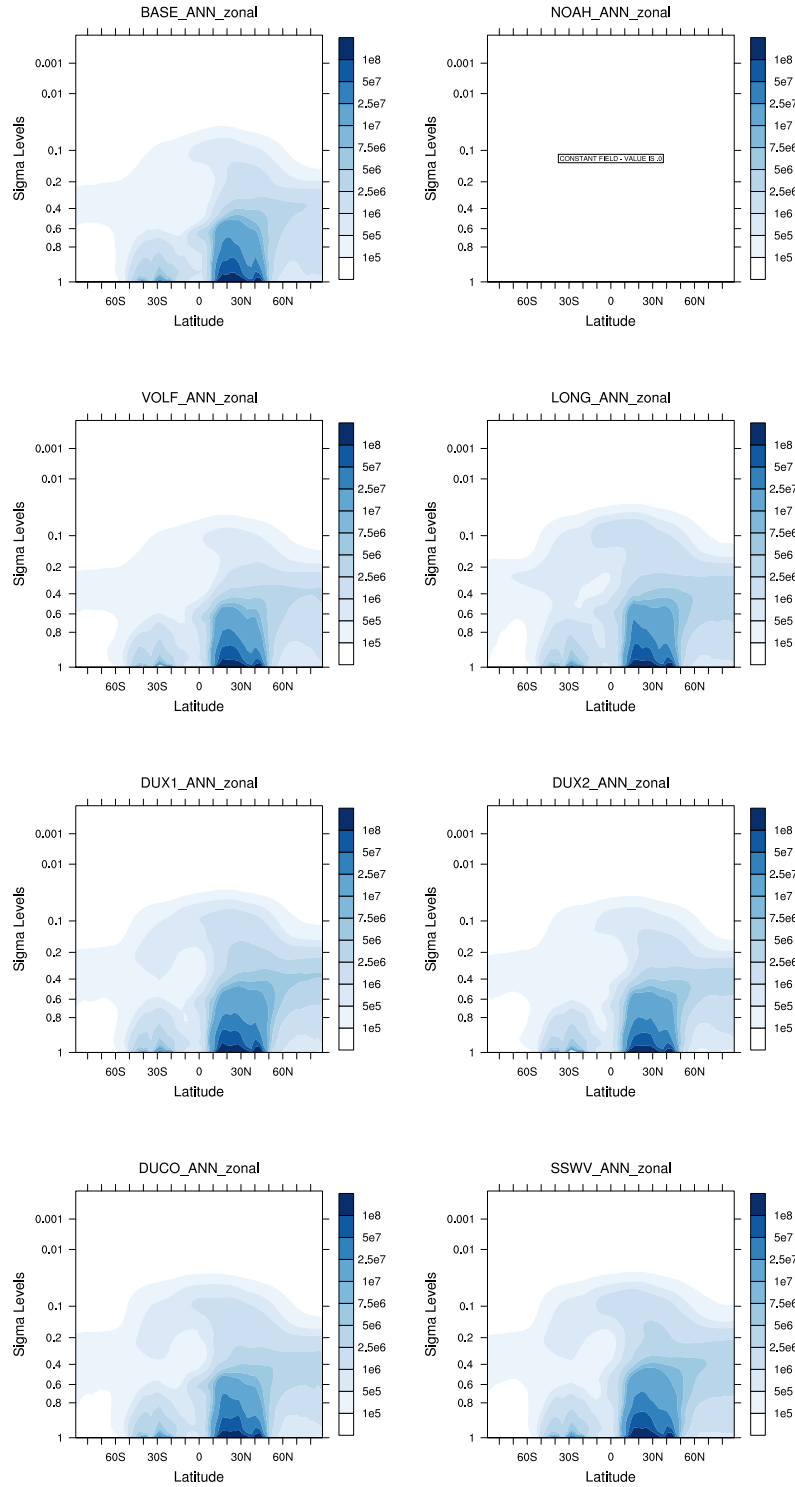


Figure E.4. 2012 zonally averaged mode 6 aerosol number density ( $m^{-3}$ ) for BASE, NOAH, VOLF, LONG, DUX1, DUX2, DUCO, and SSWV experiments.

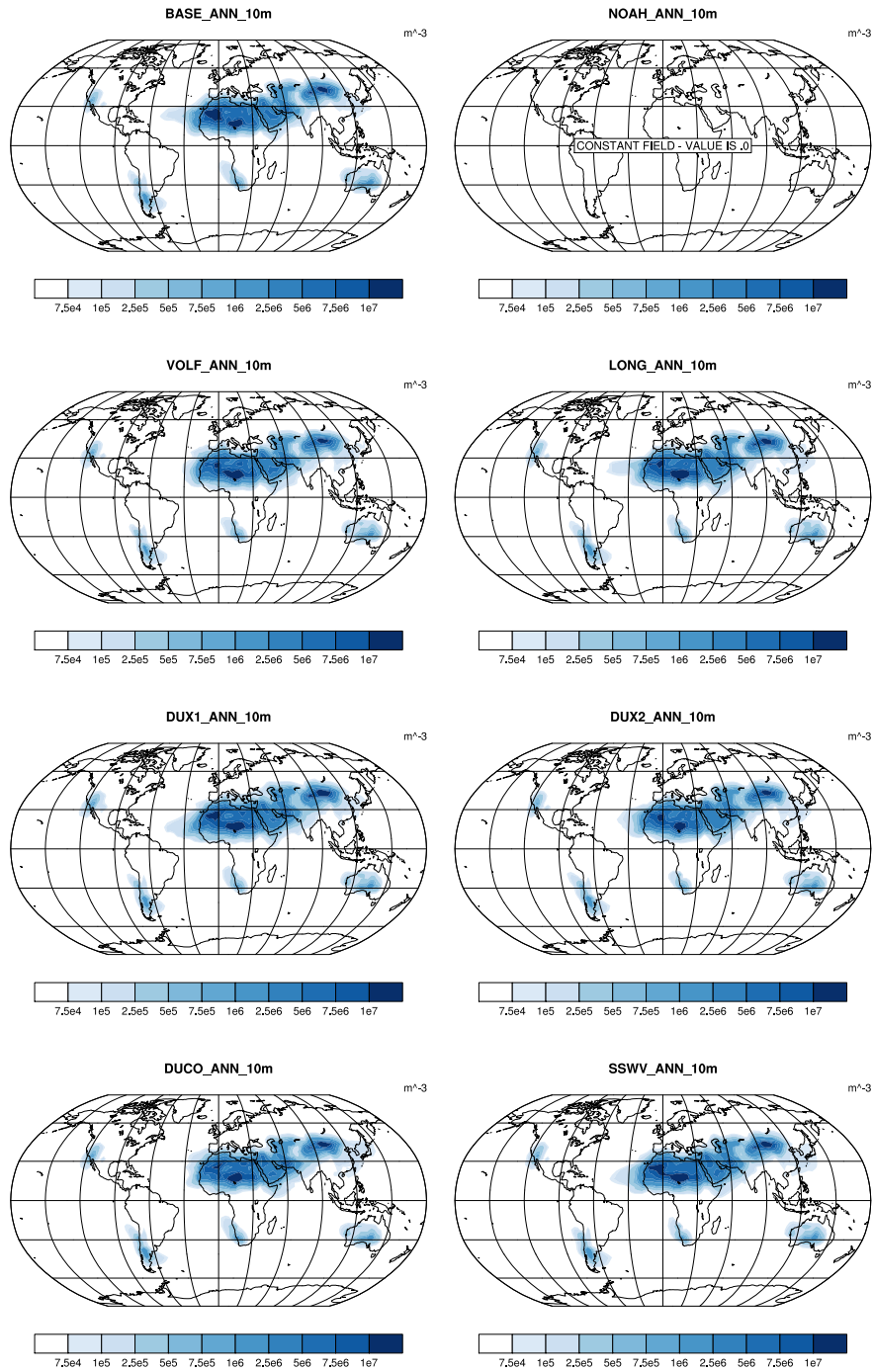


Figure E.5. 10 m mode 7 aerosol number density ( $\text{m}^{-3}$ ) averaged over 2012 for BASE, NOAH, VOLF, LONG, DUX1, DUX2, DUCC, and SSWV experiments.

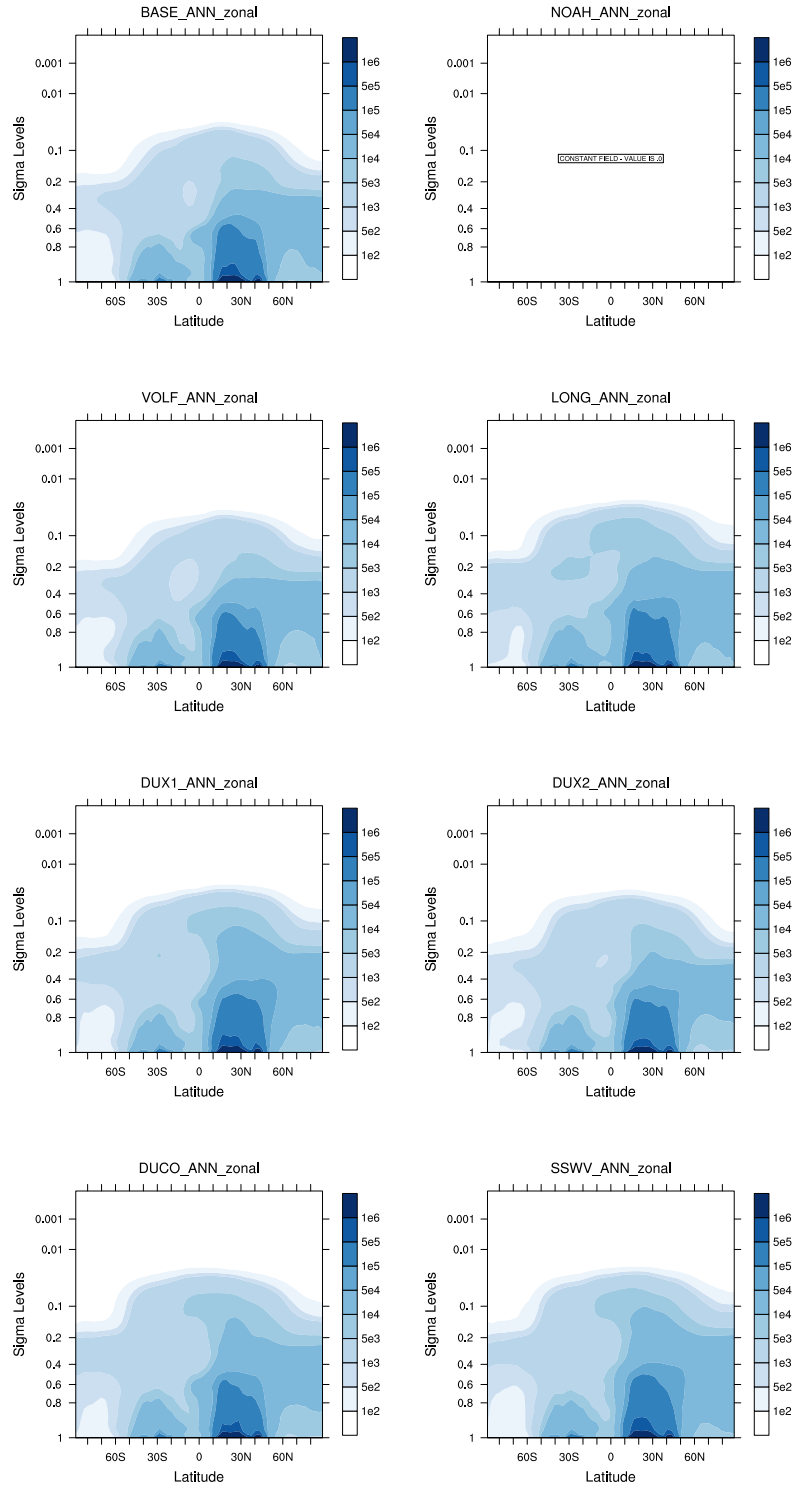


Figure E.6. 2012 zonally averaged mode 7 aerosol number density ( $m^{-3}$ ) for BASE, NOAH, VOLF, LONG, DUX1, DUX2, DUCO, and SSWV experiments.

## Appendix F

# Global and Zonal Averages of the Aersosol Species

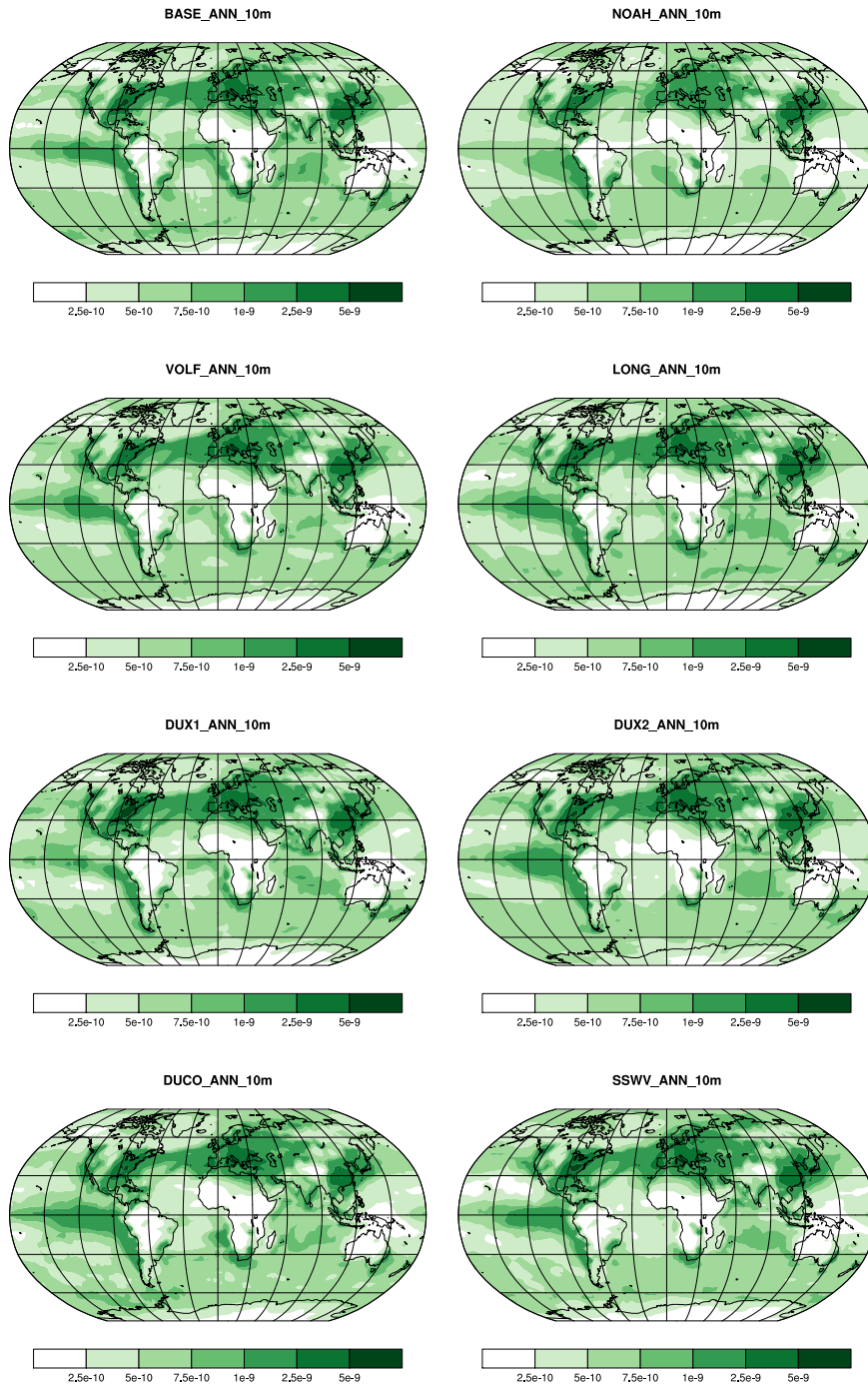


Figure F.1. 10 m ASO<sub>4</sub> volume mixing ratio (mol/mol) averaged over 2012 for BASE, NOAH, VOLF, LONG, DUX1, DUX2, DUCO, and SSWV experiments.

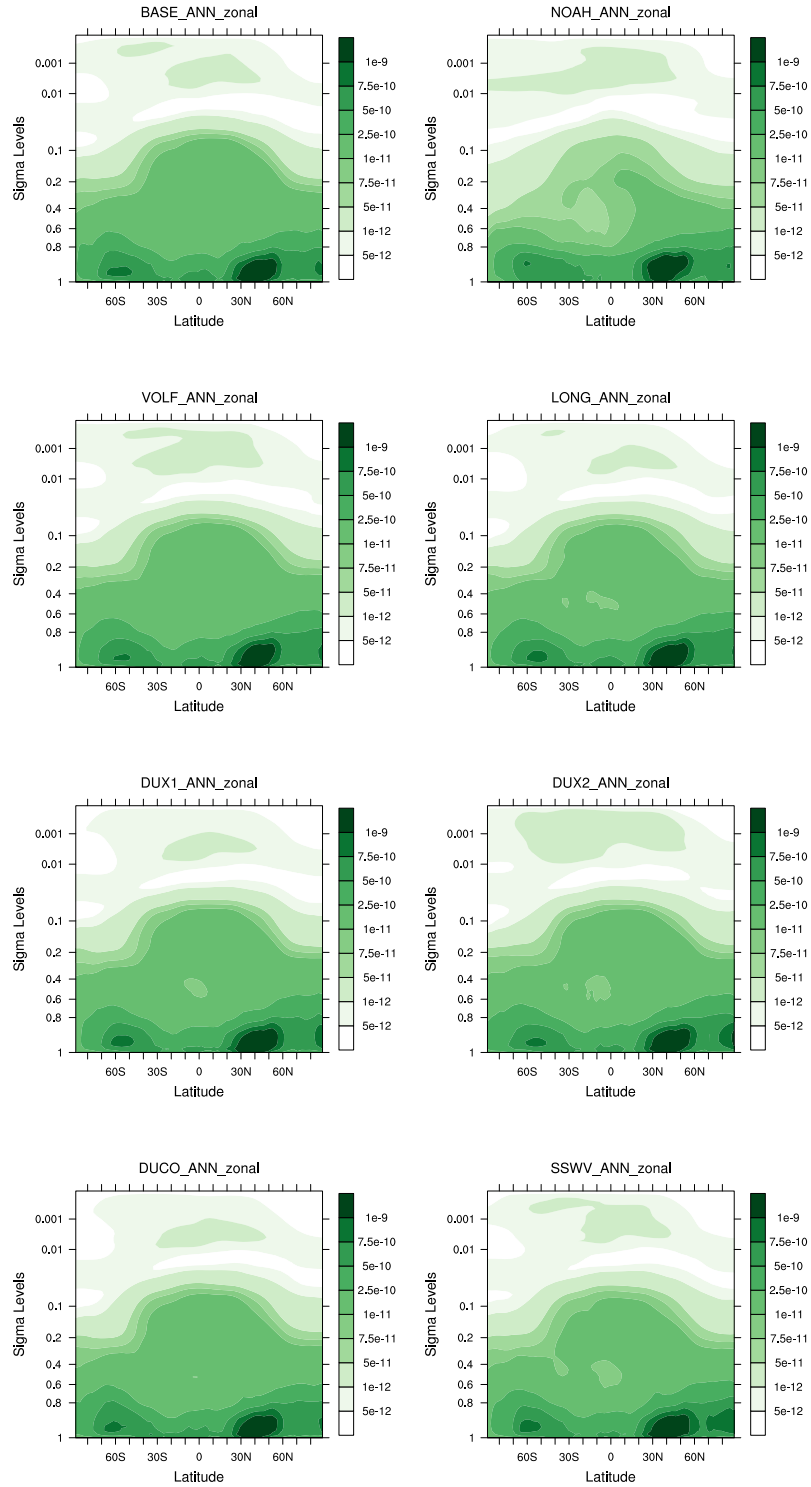


Figure F.2. 2012 zonally averaged ASO<sub>4</sub> volume mixing ratio for BASE, NOAH, VOLF, LONG, DUX1, DUX2, DUCO, and SSWV experiments.

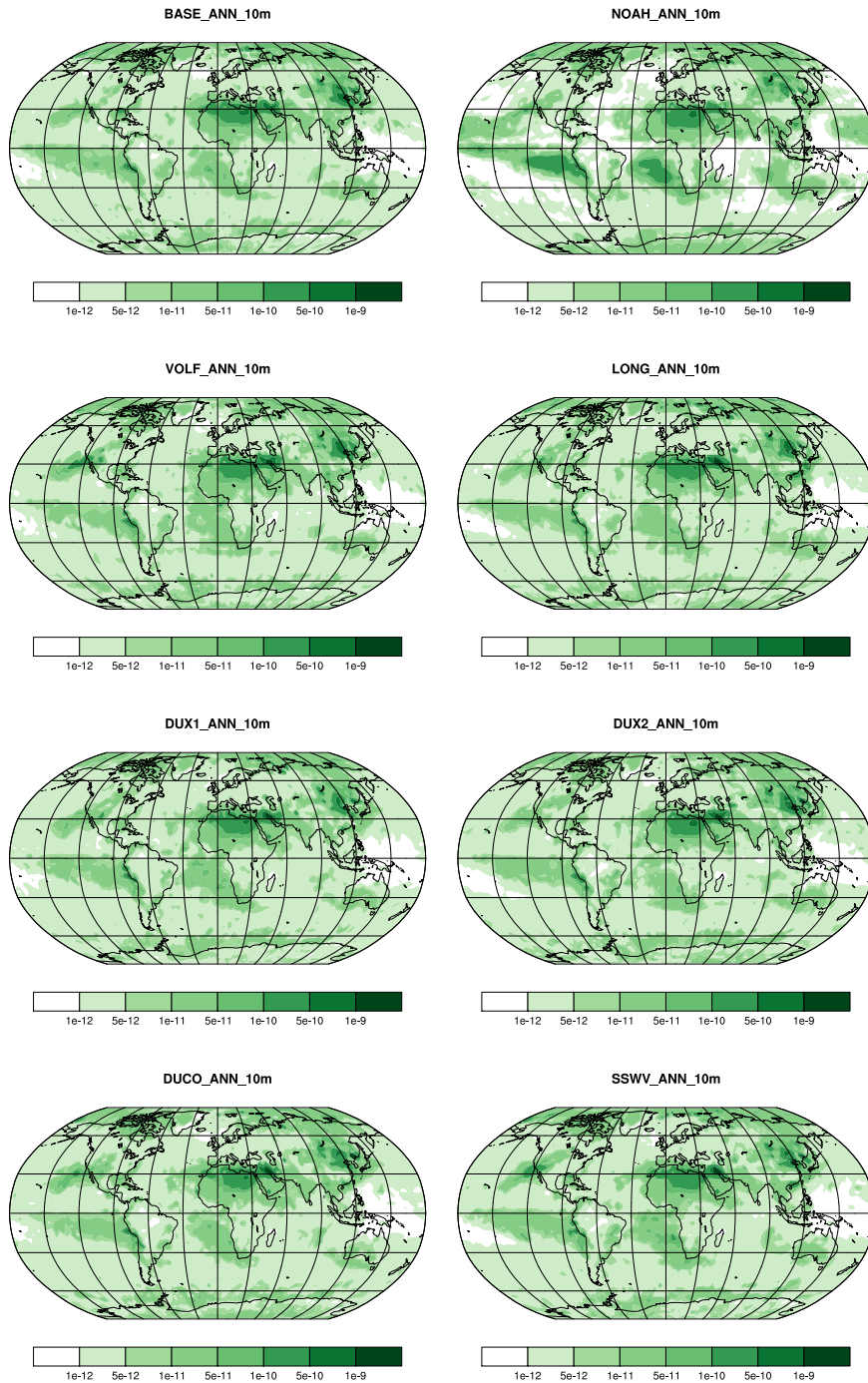


Figure F.3. 10 m ANH<sub>4</sub> volume mixing ratio (mol/mol) averaged over 2012 for BASE, NOAH, VOLF, LONG, DUX1, DUX2, DUCO, and SSWV experiments.

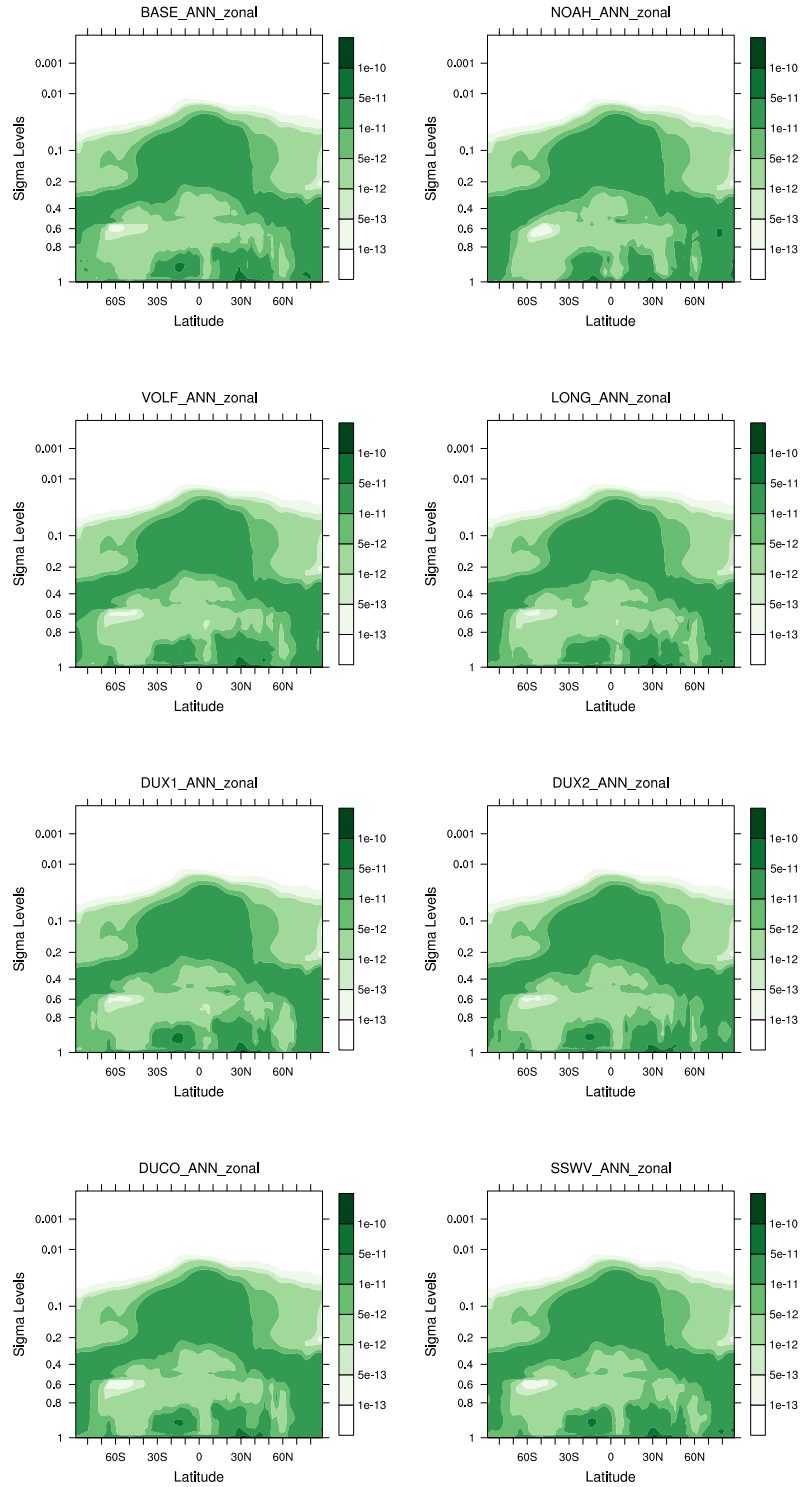


Figure F.4. 2012 zonally averaged  $\text{ANH}_4$  volume mixing ratio for BASE, NOAH, VOLF, LONG, DUX1, DUX2, DUCO, and SSWV experiments.

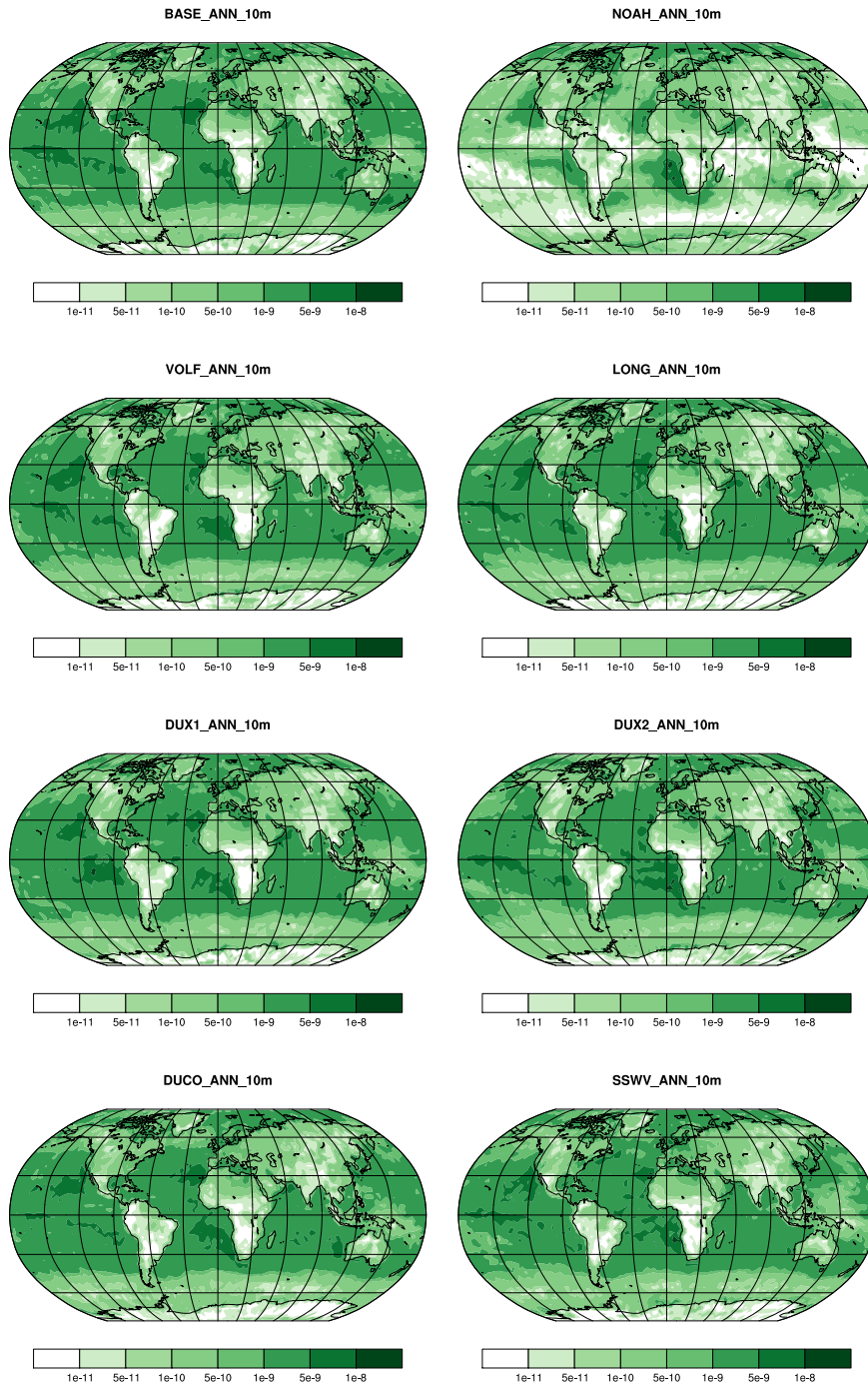


Figure F.5. 10 m ANO<sub>3</sub> volume mixing ratio (mol/mol) averaged over 2012 for BASE, NOAH, VOLF, LONG, DUX1, DUX2, DUCO, and SSWV experiments.

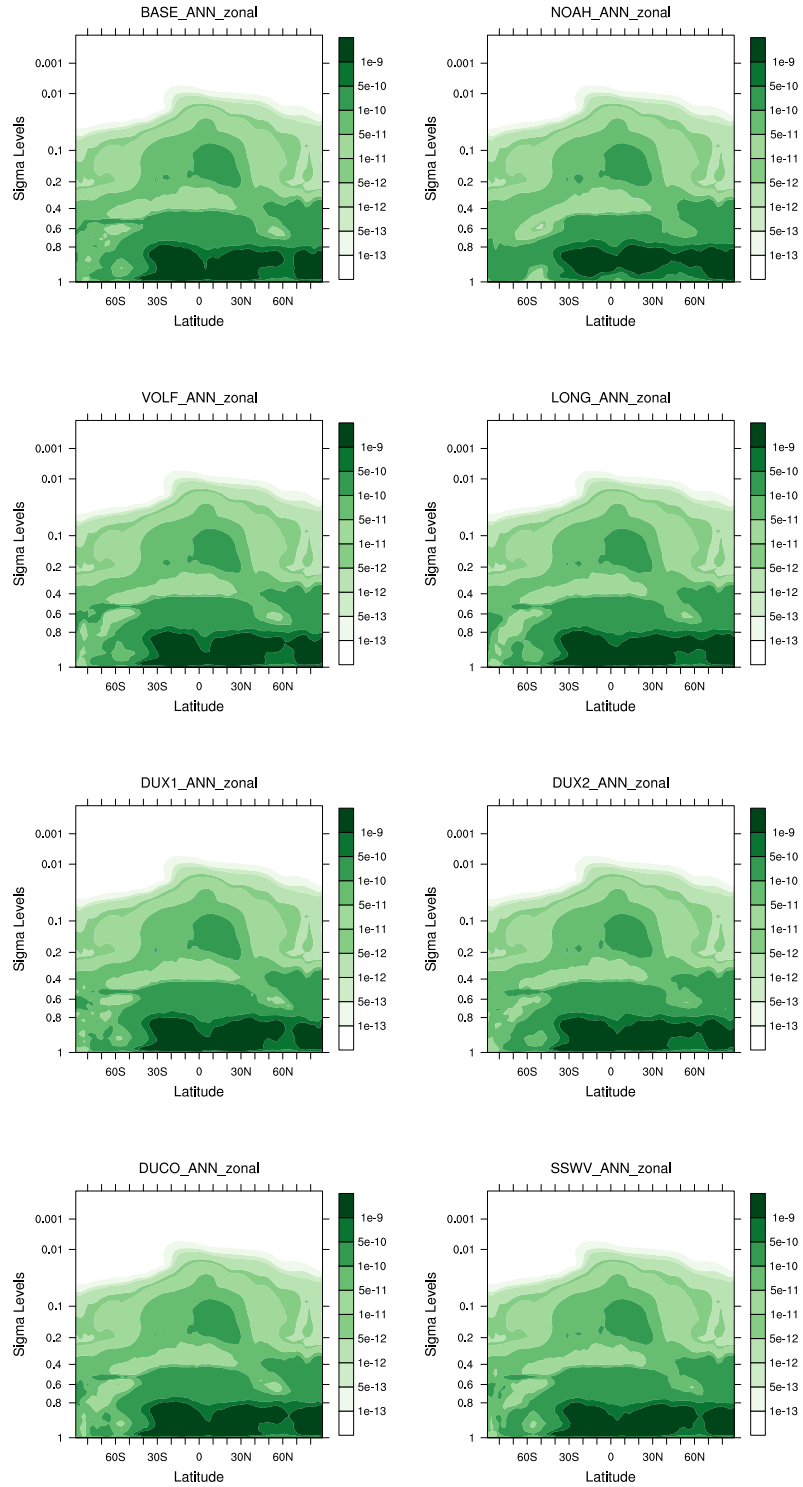


Figure F.6. 2012 zonally averaged ANO<sub>3</sub> volume mixing ratio for BASE, NOAH, VOLF, LONG, DUX1, DUX2, DUCO, and SSWV experiments.

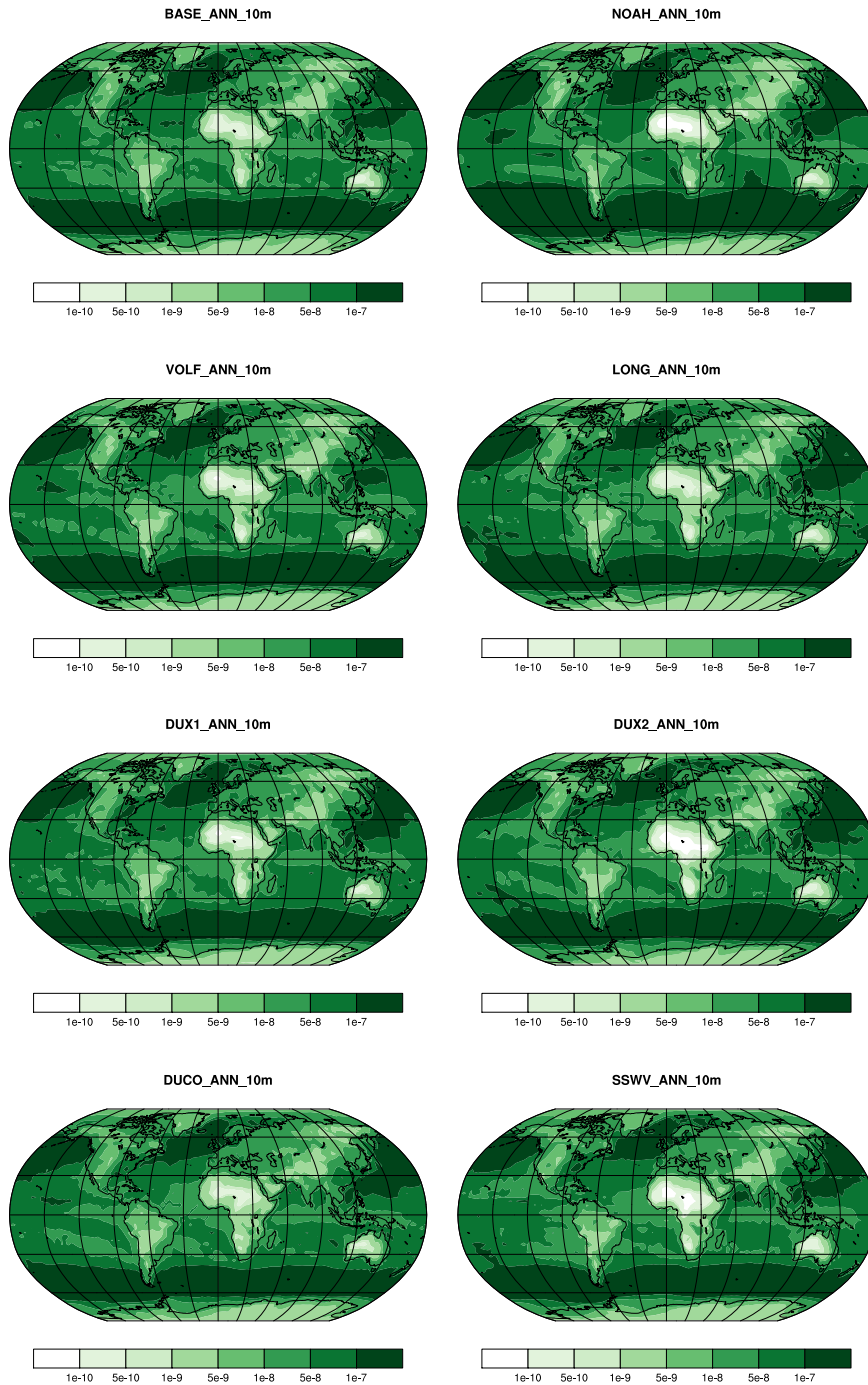


Figure F.7. 10 m AH<sub>2</sub>O volume mixing ratio (mol/mol) averaged over 2012 for BASE, NOAH, VOLF, LONG, DUX1, DUX2, DUCCO, and SSWV experiments.

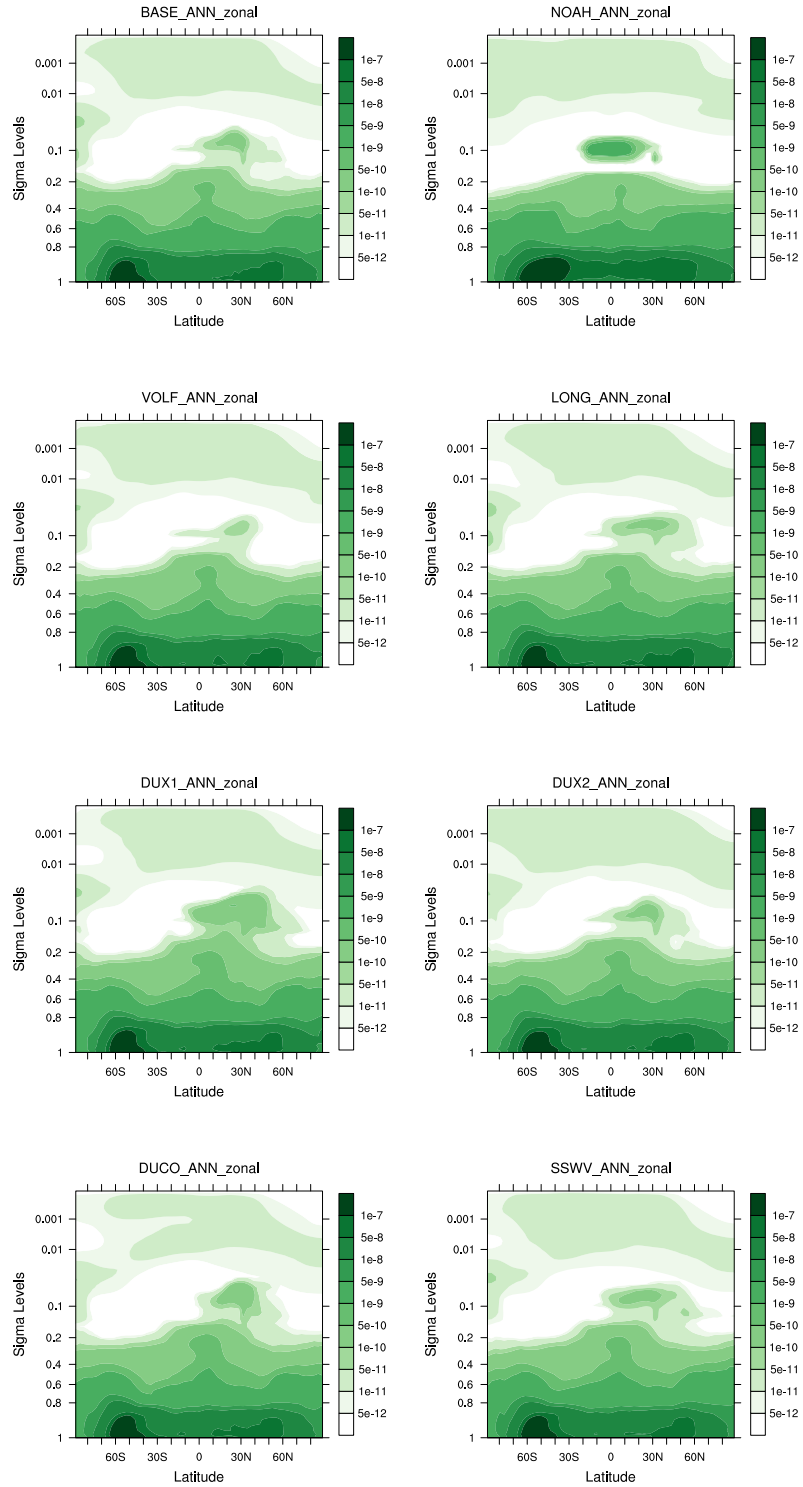


Figure F.8. 2012 zonally averaged  $\text{AH}_2\text{O}$  volume mixing ratio for BASE, NOAH, VOLF, LONG, DUX1, DUX2, DUCO, and SSWV experiments.

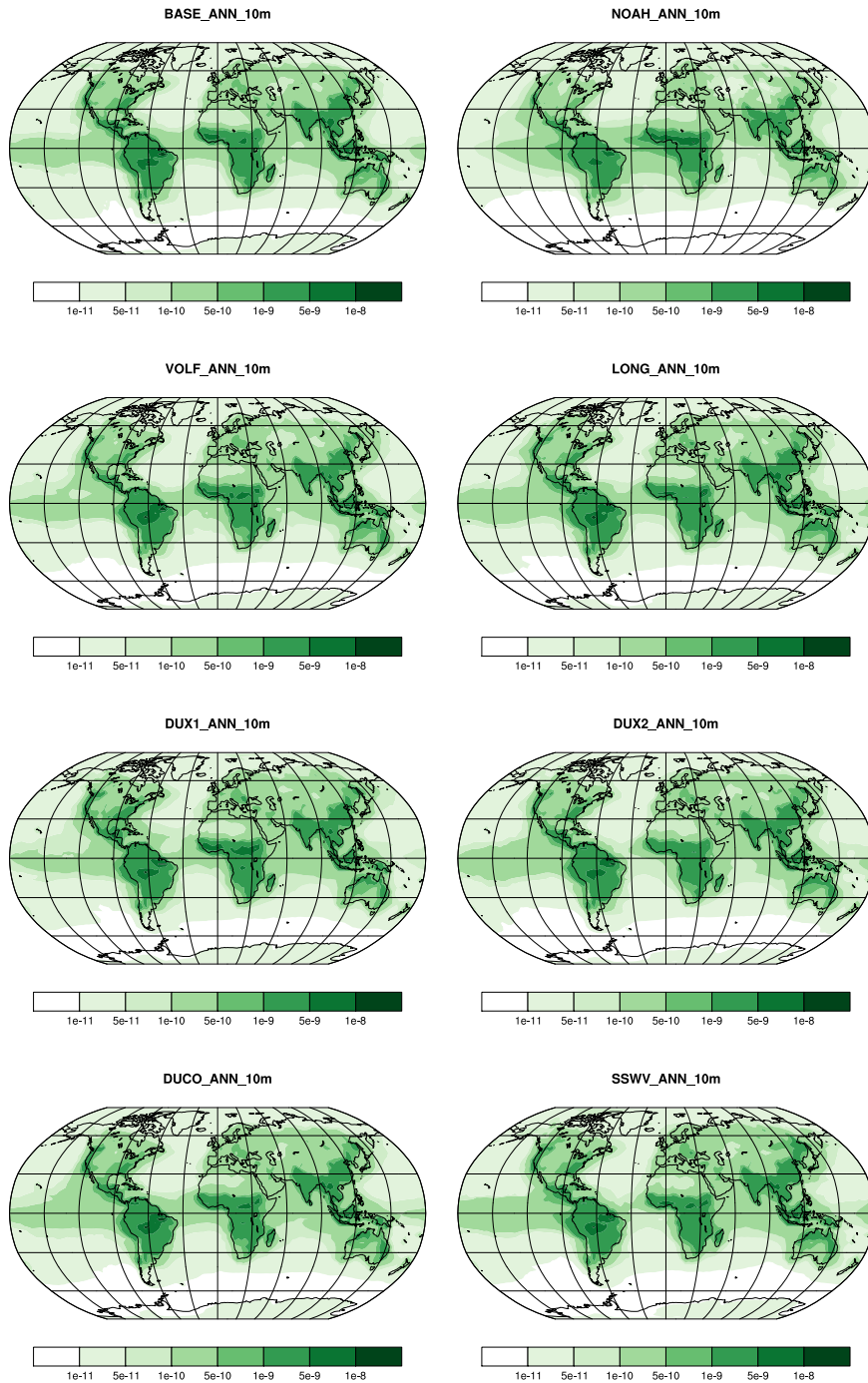


Figure F.9. 10 m AOC volume mixing ratio (mol/mol) averaged over 2012 for BASE, NOAH, VOLF, LONG, DUX1, DUX2, DUCO, and SSWV experiments.

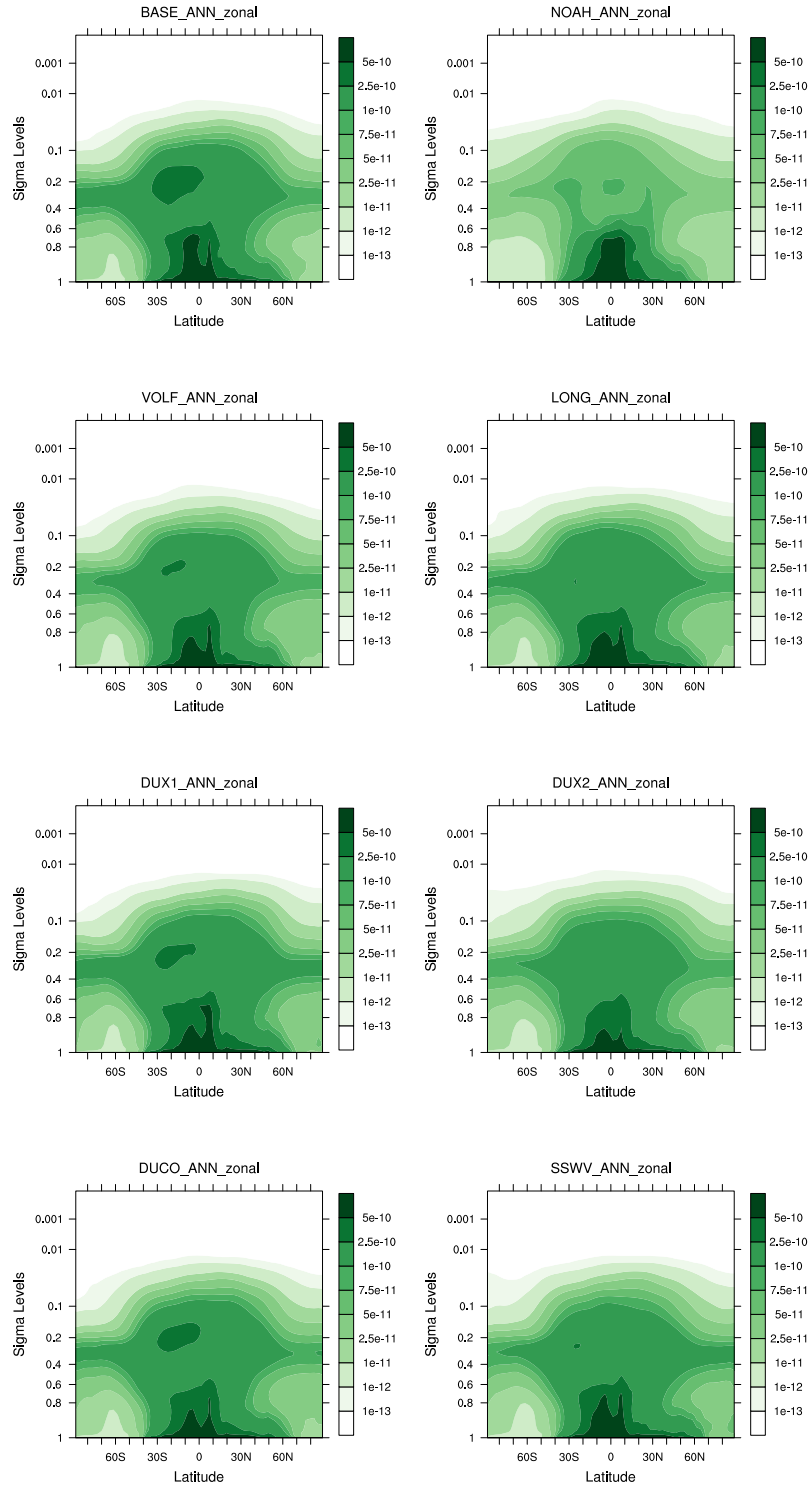


Figure F.10. 2012 zonally averaged AOC volume mixing ratio for BASE, NOAH, VOLF, LONG, DUX1, DUX2, DUCO, and SSWV experiments.

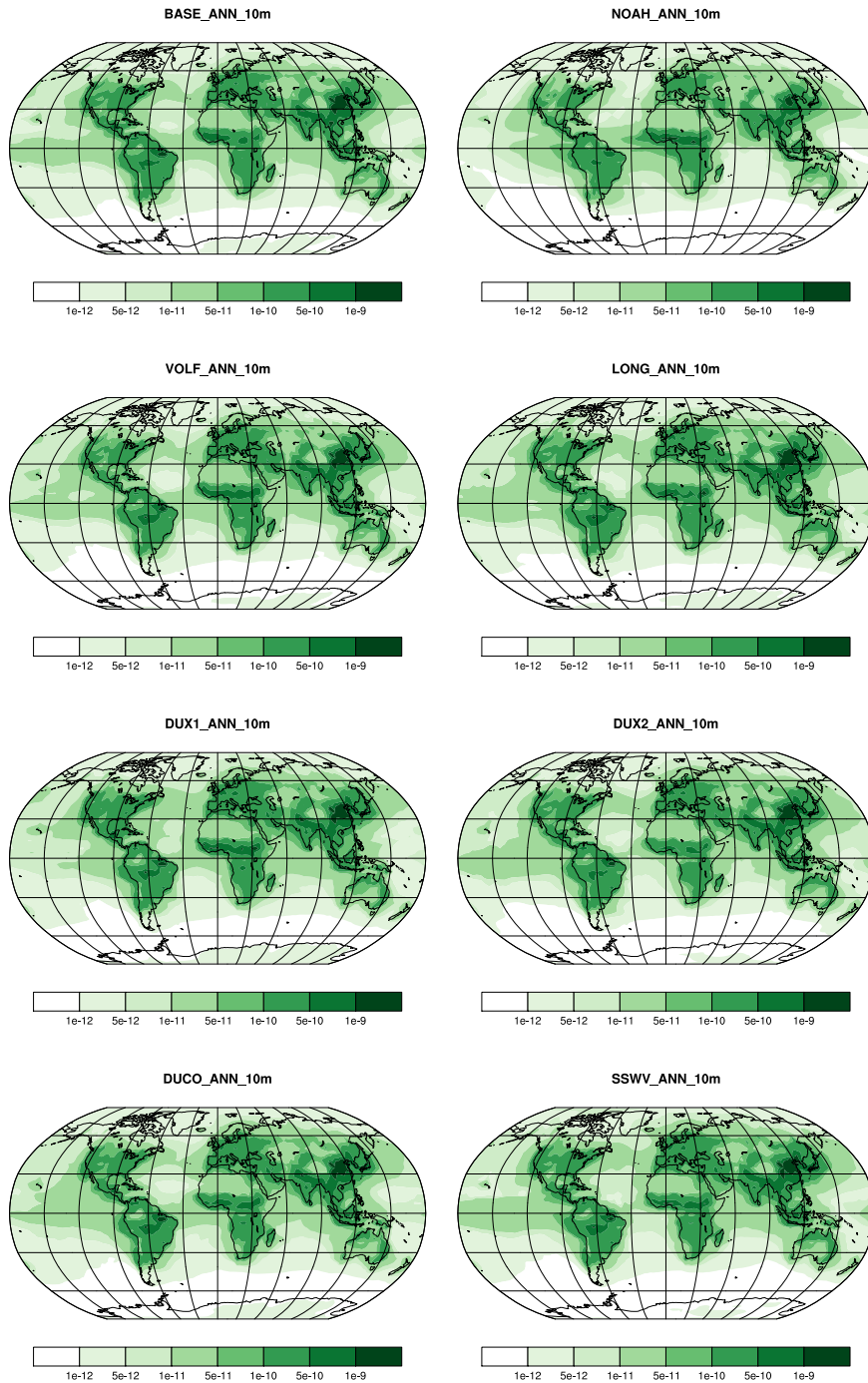


Figure F.11. 10 m ABC volume mixing ratio (mol/mol) averaged over 2012 for BASE, NOAH, VOLF, LONG, DUX1, DUX2, DUCO, and SSWV experiments.

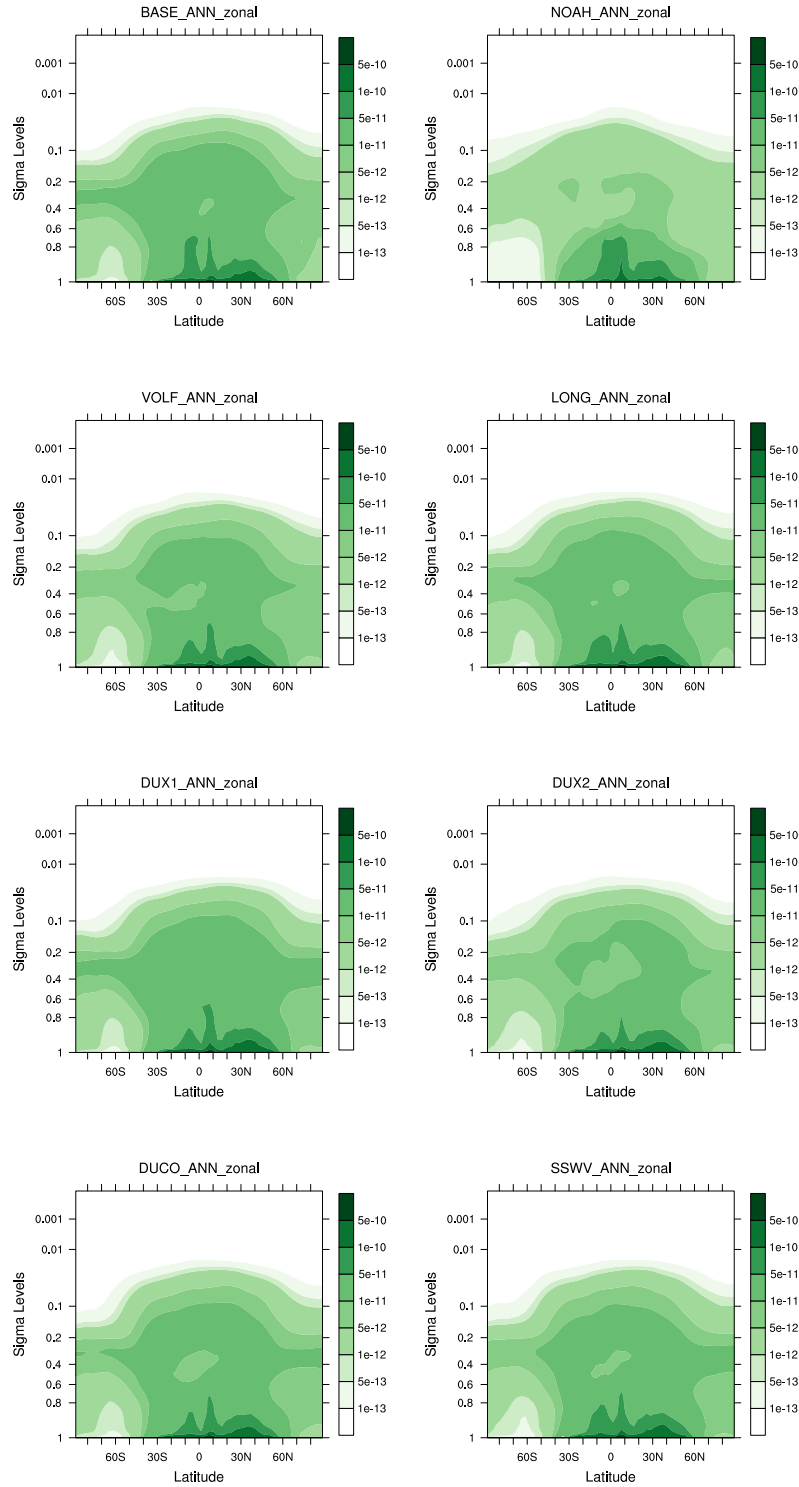


Figure F.12. 2012 zonally averaged ABC volume mixing ratio for BASE, NOAH, VOLF, LONG, DUX1, DUX2, DUCO, and SSWV experiments.

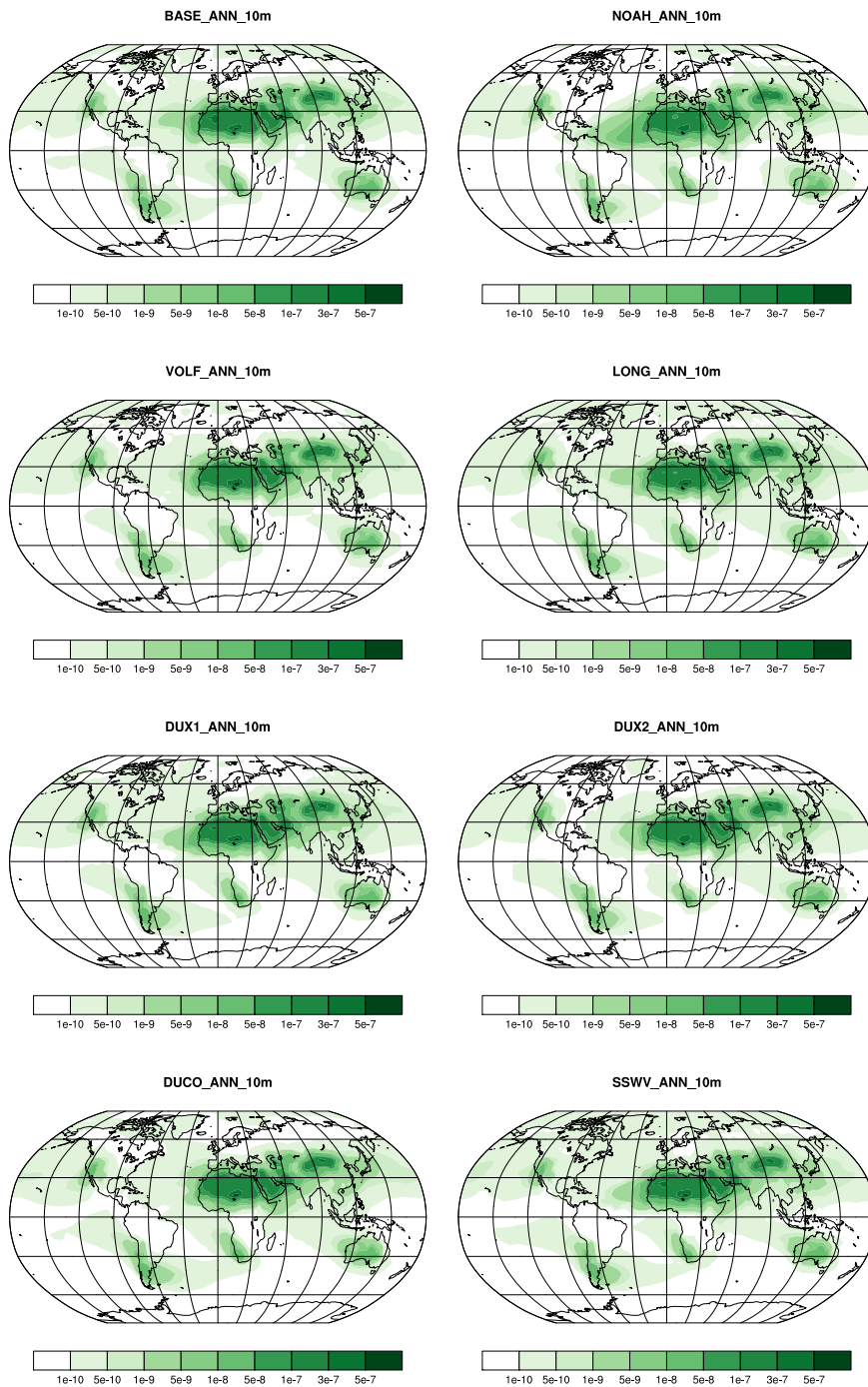


Figure F.13. 10 m ADU volume mixing ratio (mol/mol) averaged over 2012 for BASE, NOAH, VOLF, LONG, DUX1, DUX2, DUCO, and SSWV experiments.

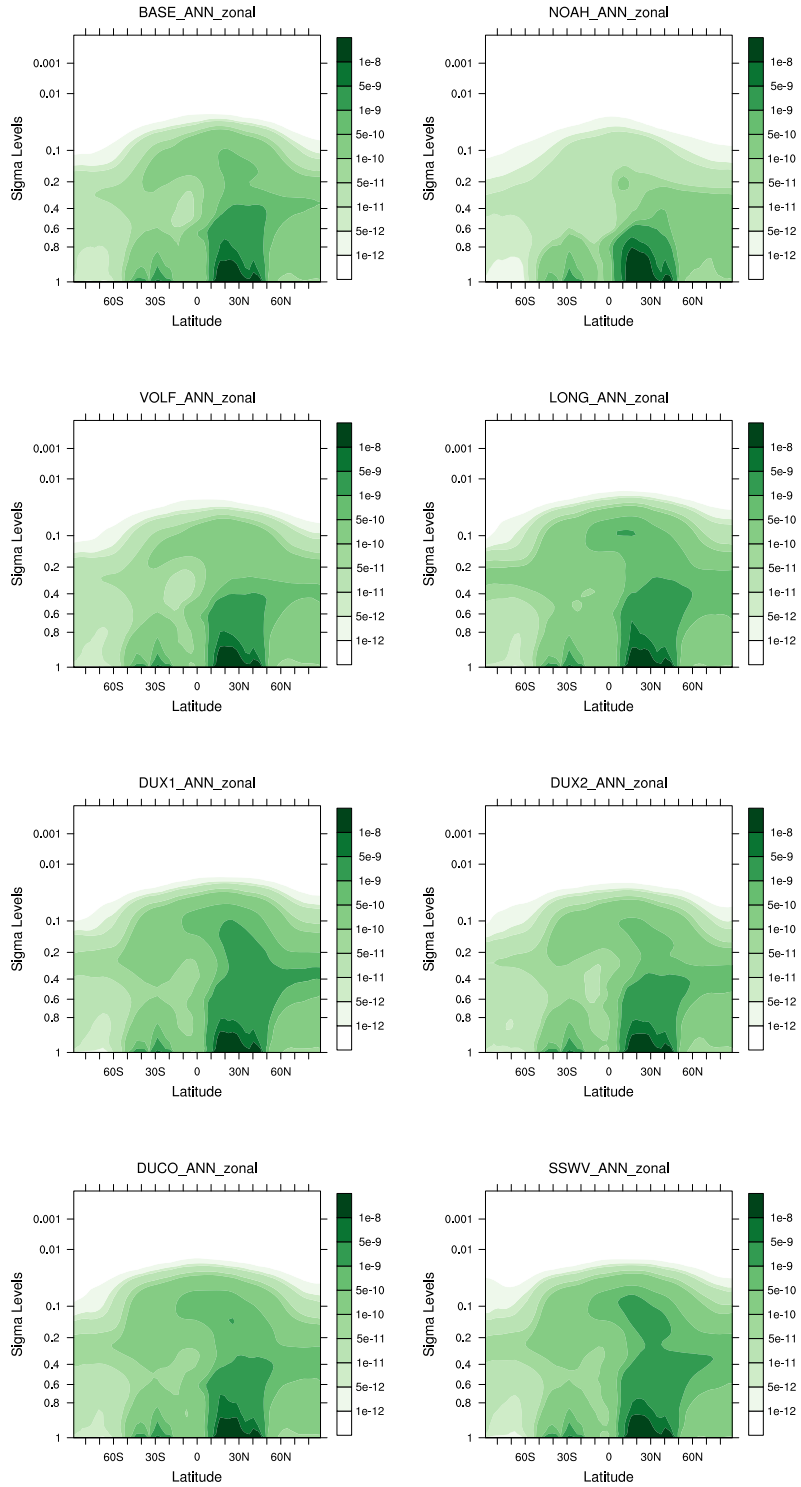


Figure F.14. 2012 zonally averaged ADU volume mixing ratio for BASE, NOAH, VOLF, LONG, DUX1, DUX2, DUCO, and SSWV experiments.

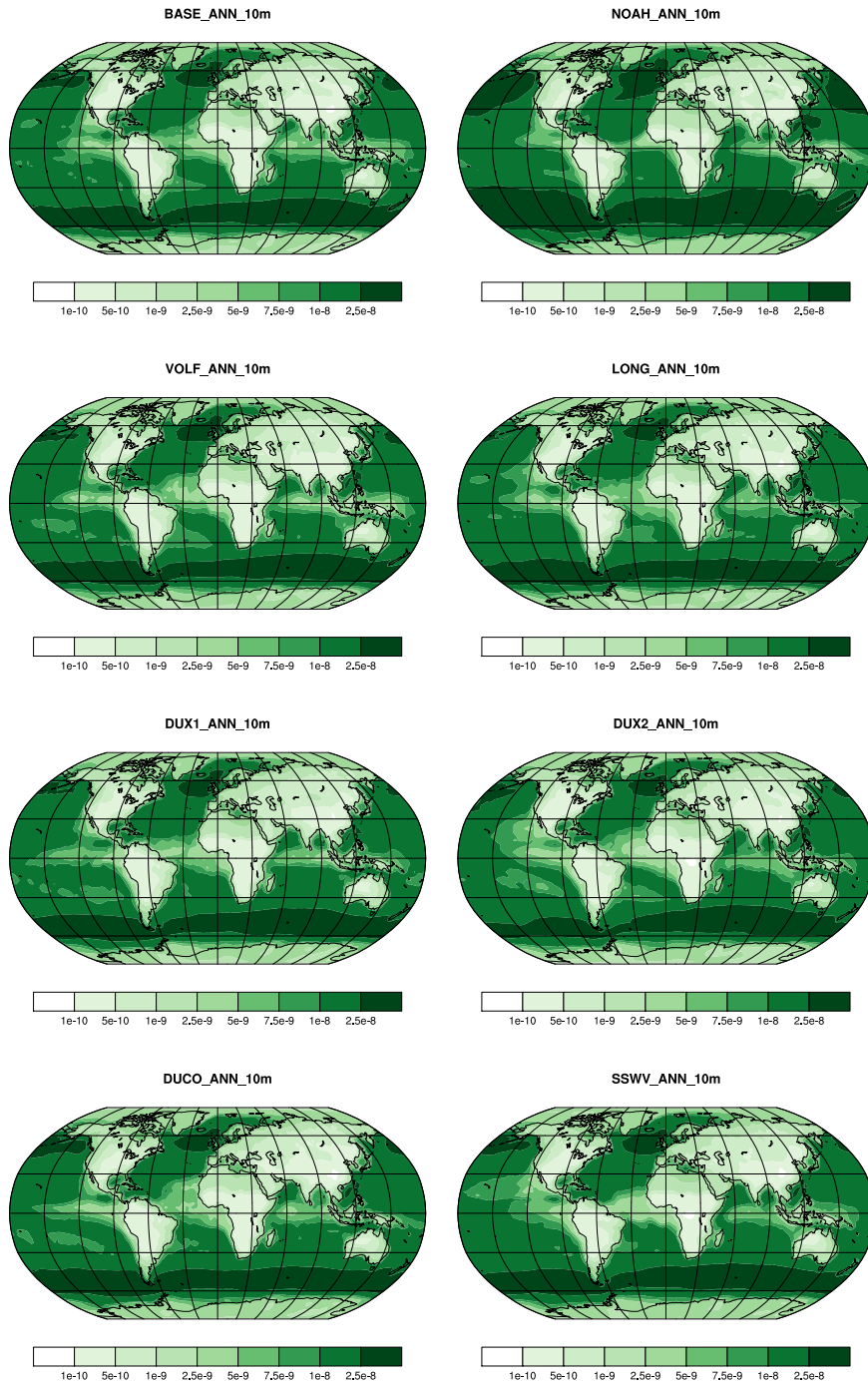


Figure F.15. 10 m ASEA volume mixing ratio (mol/mol) averaged over 2012 for BASE, NOAH, VOLF, LONG, DUX1, DUX2, DUCO, and SSWV experiments.

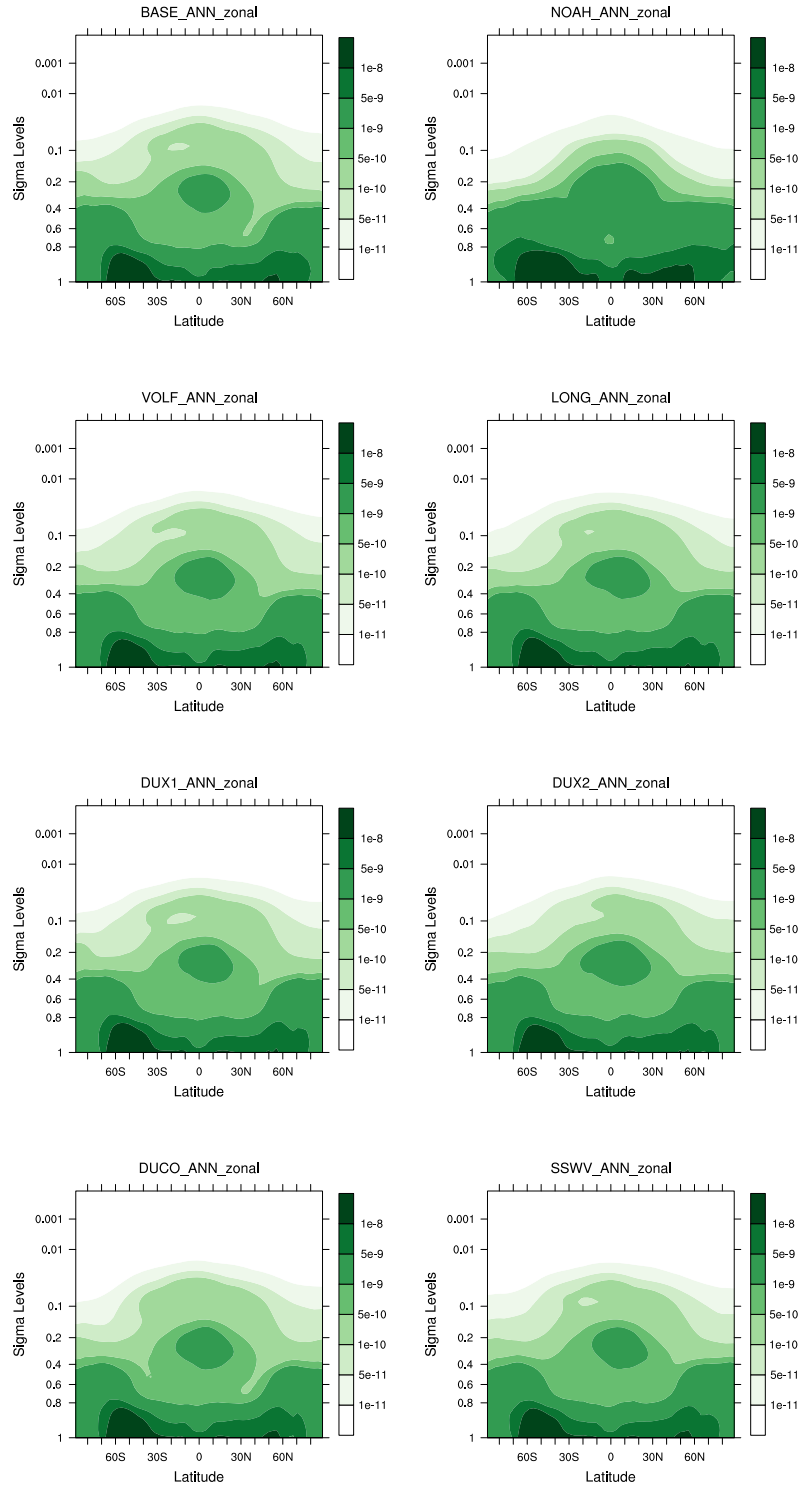


Figure F.16. 2012 zonally averaged ASEA volume mixing ratio for BASE, NOAH, VOLF, LONG, DUX1, DUX2, DUCO, and SSWV experiments.

## Appendix G

# Seasonal Global Load Averages of Aersosol and Chemical Species

Aerosol Mode	CASE							
	BASE	NOAH	VOLF	LONG	DUX1	DUX2	DUCO	SSWV
1	15.24	-	20.2	16.7	21.1	24.2	18.7	19.3
2	10.5	-	10.7	10.5	10.6	10.9	10.5	10.5
3	6.0	-	5.7	5.9	5.8	6.0	5.9	5.9
4	0.50	-	0.49	0.51	0.50	0.50	0.52	0.51
5	3.2	-	3.3	3.1	3.1	3.1	2.8	3.3
6	3.3	-	3.2	3.6	3.6	3.0	3.8	4.2
7	0.024	-	0.023	0.026	0.026	0.022	0.027	0.026

Table G.1. 2012 DJF global averages of the aerosol number density ( $\times 10^6 \text{ m}^{-3}$ ) in the seven M7 aerosol modes and eight experiments.

Aerosol Mode	CASE							
	BASE	NOAH	VOLF	LONG	DUX1	DUX2	DUCO	SSWV
1	11.8	-	16.4	13.0	16.2	16.0	16.7	15.3
2	9.3	-	9.5	9.2	9.5	9.6	9.5	9.6
3	5.4	-	5.3	5.7	5.6	5.4	5.5	5.8
4	0.63	-	0.60	0.63	0.67	0.62	0.66	0.68
5	2.5	-	2.5	2.6	2.7	2.4	2.2	2.7
6	3.4	-	3.4	4.8	4.7	3.9	3.9	4.8
7	0.026	-	0.025	0.035	0.036	0.029	0.029	0.037

Table G.2. 2012 MAM global averages of the aerosol number density ( $\times 10^6 \text{ m}^{-3}$ ) in the seven M7 aerosol modes and eight experiments.

Aerosol Mode	CASE							
	BASE	NOAH	VOLF	LONG	DUX1	DUX2	DUCO	SSWV
1	9.4	-	16.8	7.1	7.7	7.8	10.9	11.4
2	6.8	-	7.2	6.6	6.9	7.3	7.1	6.9
3	4.9	-	7.7	8.2	9.3	7.5	8.2	9.0
4	0.66	-	0.64	0.65	0.71	0.63	0.70	0.65
5	3.3	-	3.4	3.4	3.8	3.1	3.4	3.7
6	3.3	-	2.9	3.9	3.5	3.8	3.4	3.5
7	0.024	-	0.021	0.027	0.024	0.026	0.024	0.025

Table G.3. 2012 JJA global averages of the aerosol number density ( $\times 10^6 \text{ m}^{-3}$ ) in the seven M7 aerosol modes and eight experiments.

Aerosol Mode	SON Global Average ( $\text{m}^{-3}$ )							
	BASE	NOAH	VOLF	LONG	DUX1	DUX2	DUCO	SSWV
1	1.6	-	2.5	0.9	1.3	1.5	1.5	1.4
2	5.4	-	5.7	5.1	5.2	5.8	5.3	5.2
3	6.9	-	6.8	7.0	7.1	6.4	6.9	7.2
4	0.61	-	0.63	0.61	0.61	0.61	0.61	0.60
5	2.3	-	2.4	2.5	2.5	2.3	2.3	2.5
6	3.8	-	3.2	4.4	3.9	4.4	3.9	4.1
7	0.026	-	0.022	0.030	0.027	0.029	0.027	0.028

Table G.4. 2012 SON global averages of the aerosol number density ( $\times 10^6 \text{ m}^{-3}$ ) in the seven M7 aerosol modes and eight experiments.

Variable	CASE							
	BASE	NOAH	VOLF	LONG	DUX1	DUX2	DUCO	SSWV
ASO <sub>4</sub>	1.51	1.34	1.49	1.50	1.49	1.52	1.60	1.48
ANH <sub>4</sub>	0.0892	0.0865	0.0853	0.0856	0.0855	0.0855	0.0860	0.0886
ANO <sub>3</sub>	1.94	1.96	1.99	2.03	1.85	1.90	2.02	1.93
AH <sub>2</sub> O	45.0	81.0	43.5	46.0	46.2	42.5	46.2	46.4
AOC	0.832	0.565	0.768	0.790	0.821	0.772	0.795	0.802
ABC	0.107	0.0734	0.101	0.107	0.111	0.102	0.107	0.108
ADU	6.67	5.63	6.50	7.27	7.22	6.40	7.38	7.32
ASEA	11.6	18.2	11.1	11.5	11.5	10.8	11.3	11.8
NO <sub>2</sub>	19.1	18.5	19.0	19.0	19.1	18.9	18.9	18.9
NO <sub>3</sub>	0.167	0.141	0.175	0.162	0.174	0.153	0.157	0.138
N <sub>2</sub> O <sub>5</sub>	0.0341	0.0490	0.0324	0.0361	0.0299	0.0334	0.0325	0.0331
HNO <sub>3</sub>	36.1	34.1	36.0	35.6	35.7	35.9	36.3	35.4
O <sub>3</sub>	17900	17400	17800	17900	17900	17900	18100	17900
OH	0.680	0.680	0.680	0.680	0.680	0.680	0.679	0.679

Table G.5. DJF global load averages ( $\times 10^{-10} \text{ mol mol}^{-1}$ ) of aerosol sulphate (ASO<sub>4</sub>), aerosol ammonium (ANH<sub>4</sub>), aerosol nitrate (ANO<sub>3</sub>), aerosol water (AH<sub>2</sub>O), aerosol organic carbon (AOC), aerosol black carbon (ABC), aerosol dust (ADU), aerosol sea salt (ASEA), NO<sub>2</sub>, NO<sub>3</sub>, N<sub>2</sub>O<sub>5</sub>, HNO<sub>3</sub>, O<sub>3</sub>, and OH.

Variable	CASE							
	BASE	NOAH	VOLF	LONG	DUX1	DUX2	DUCO	SSWV
ASO <sub>4</sub>	1.47	1.32	1.50	1.51	1.51	1.60	1.51	1.56
ANH <sub>4</sub>	0.0803	0.0791	0.0758	0.0777	0.0738	0.0746	0.0785	0.0790
ANO <sub>3</sub>	2.00	1.79	1.77	2.04	1.98	1.75	1.96	1.97
AH <sub>2</sub> O	65.6	93.5	64.7	68.1	69.3	64.6	70.8	69.3
AOC	0.690	0.394	0.625	0.686	0.695	0.633	0.681	0.748
ABC	0.0856	0.0497	0.080	0.0913	0.0957	0.0845	0.0883	0.104
ADU	7.42	5.89	7.38	9.43	9.95	8.15	8.41	10.1
ASEA	15.2	21.3	14.6	15.4	16.1	14.4	16.2	15.9
NO <sub>2</sub>	18.9	18.2	18.8	18.7	18.5	18.4	18.3	18.7
NO <sub>3</sub>	0.0969	0.0882	0.0951	0.0936	0.0959	0.0923	0.0927	0.0917
N <sub>2</sub> O <sub>5</sub>	0.0236	0.0241	0.0242	0.0215	0.0222	0.0226	0.0223	0.0239
HNO <sub>3</sub>	36.4	35.2	36.2	36.5	36.3	35.9	36.7	36.1
O <sub>3</sub>	18300	17700	18200	18100	18200	18000	18300	18200
OH	0.661	0.660	0.661	0.661	0.661	0.660	0.660	0.660

Table G.6. MAM global load averages ( $\times 10^{-10}$  mol mol<sup>-1</sup>) of aerosol sulphate (ASO<sub>4</sub>), aerosol ammonium (ANH<sub>4</sub>), aerosol nitrate (ANO<sub>3</sub>), aerosol water (AH<sub>2</sub>O), aerosol organic carbon (AOC), aerosol black carbon (ABC), aerosol dust (ADU), aerosol sea salt (ASEA), NO<sub>2</sub>, NO<sub>3</sub>, N<sub>2</sub>O<sub>5</sub>, HNO<sub>3</sub>, O<sub>3</sub>, and OH.

Variable	CASE							
	BASE	NOAH	VOLF	LONG	DUX1	DUX2	DUCO	SSWV
ASO <sub>4</sub>	1.13	1.11	1.12	1.08	1.22	1.09	1.14	1.07
ANH <sub>4</sub>	0.0567	0.0637	0.0558	0.0574	0.0570	0.0568	0.0555	0.0607
ANO <sub>3</sub>	1.72	1.41	1.67	1.59	1.82	1.45	1.67	1.60
AH <sub>2</sub> O	89.64	89.60	82.15	85.82	86.28	83.02	89.70	82.05
AOC	1.29	0.669	1.14	1.33	1.49	1.08	1.25	1.46
ABC	0.0148	0.0714	0.135	0.163	0.178	0.123	0.152	0.161
ADU	7.44	3.96	6.92	9.54	8.38	8.03	8.39	8.93
ASEA	19.5	21.0	19.0	18.7	20.2	19.0	20.2	19.0
NO <sub>2</sub>	18.6	18.5	18.3	18.3	18.3	18.0	18.1	18.1
NO <sub>3</sub>	0.101	0.109	0.101	0.103	0.103	0.101	0.109	0.103
N <sub>2</sub> O <sub>5</sub>	0.0165	0.0168	0.0166	0.0168	0.0182	0.0168	0.0162	0.0169
HNO <sub>3</sub>	35.7	33.6	35.5	35.3	35.6	35.1	35.6	34.7
O <sub>3</sub>	17300	17100	17400	17100	17100	17100	17400	17100
OH	0.681	0.681	0.681	0.679	0.680	0.680	0.679	0.679

Table G.7. JJA global load averages ( $\times 10^{-10}$  mol mol<sup>-1</sup>) of aerosol sulphate (ASO<sub>4</sub>), aerosol ammonium (ANH<sub>4</sub>), aerosol nitrate (ANO<sub>3</sub>), aerosol water (AH<sub>2</sub>O), aerosol organic carbon (AOC), aerosol black carbon (ABC), aerosol dust (ADU), aerosol sea salt (ASEA), NO<sub>2</sub>, NO<sub>3</sub>, N<sub>2</sub>O<sub>5</sub>, HNO<sub>3</sub>, O<sub>3</sub>, and OH.

Variable	CASE							
	BASE	NOAH	VOLF	LONG	DUX1	DUX2	DUCO	SSWV
ASO <sub>4</sub>	1.25	1.06	1.22	1.16	1.25	1.26	1.20	1.17
ANH <sub>4</sub>	0.0507	0.0571	0.0497	0.0514	0.0519	0.0516	0.0502	0.0539
ANO <sub>3</sub>	1.83	1.70	1.96	1.87	1.89	1.82	1.85	1.77
AH <sub>2</sub> O	58.84	82.42	58.34	56.98	56.64	58.21	56.85	55.30
AOC	1.25	0.587	1.10	1.19	1.24	1.02	1.17	1.24
ABC	0.141	0.0659	0.122	0.136	0.144	0.121	0.130	0.141
ADU	7.60	4.62	6.69	9.26	8.23	8.35	8.45	8.68
ASEA	13.5	18.4	13.6	13.4	13.0	13.5	12.8	13.0
NO <sub>2</sub>	18.6	18.4	18.6	18.5	18.8	18.6	18.3	18.5
NO <sub>3</sub>	0.0973	0.0951	0.0988	0.0987	0.0987	0.0974	0.0984	0.0970
N <sub>2</sub> O <sub>5</sub>	0.0179	0.0185	0.0182	0.0181	0.0182	0.0181	0.0177	0.0179
HNO <sub>3</sub>	37.3	34.5	36.9	36.2	36.5	36.9	36.9	35.7
O <sub>3</sub>	18100	17900	18200	18000	18000	18100	18100	18100
OH	0.675	0.675	0.675	0.675	0.676	0.675	0.675	0.675

Table G.8. SON global load averages ( $\times 10^{-10}$  mol mol<sup>-1</sup>) of aerosol sulphate (ASO<sub>4</sub>), aerosol ammonium (ANH<sub>4</sub>), aerosol nitrate (ANO<sub>3</sub>), aerosol water (AH<sub>2</sub>O), aerosol organic carbon (AOC), aerosol black carbon (ABC), aerosol dust (ADU), aerosol sea salt (ASEA), NO<sub>2</sub>, NO<sub>3</sub>, N<sub>2</sub>O<sub>5</sub>, HNO<sub>3</sub>, O<sub>3</sub>, and OH.

# Bibliography

B. A. Albrecht.

Aerosols, cloud microphysics and fractional cloudiness.

*Science*, 245:1227–1230, 1989.

R. J. Allen and S. C. Sherwood.

The impact of natural versus anthropogenic aerosols on atmospheric circulation in the community atmosphere model.

*Clim. Dyn.*, 2011.

doi: 10.1007/s00382-010-0898-8.

L. C. Allison, H. L. Johnson, D. P. Marshall, and D. R. Munday.

Where do winds drive the antarctic circumpolar current?

*Geophys. Res. Lett.*, 37, L12605, 2010.

doi: 10.1029/2010GL043355.

M. Andreae and P. Crutzen.

Atmospheric aerosols: Biogeochemical sources and role in atmospheric chemistry.

*Science*, 276:1052–1058, 1997.

E. L. Andreas, J. B. Edson, E. C. Monahan, M. P. Rouault, and S. D. Smith.

The spray contribution to net evaporation from the sea: A review of recent progress.

*Boundary-Layer Meteorology*, 72:3–52, 1995.

T. Ayash, S. L. Gong, C. Q. Jia, P. Huang, T. L. Zhao, and D. Lavoue.

Global modelling of multicomponent aerosol species: Aerosol optical parameters.

*J. Geophys. Res.*, 113,D12203, 2008.

doi: 10.1029/2007JD008968.

H. W. Barker, J. N. S. Cole, J.-J. Morecrette, R. Pincus, P. Raisanen, K. von Salzen, and P. A. Vaillancourt.

The monte carlo independent column approximation: An assessment using several global atmospheric models.

*Quart. J. Roy. Meteorol. Soc.*, 134:1463–1478, 2008.

S. Basu, M. Richardson, and R. J. Wilson.

Simulation of the Martian dust cycle with the GFDL Mars GCM.

*J. Geophys. Res.*, 109,E11006, 2004.

doi: 10.1029/2004JE002243.

S. Basu, J. Wilson, M. Richardson, and A. Ingersoll.

Simulation of spontaneous and variable global dust storms with the GFDL Mars GCM.

*J. Geophys. Res.*, 111,E09004, 2006.

doi: 10.1029/2005JE002660.

T. Berman, V.-M. Kerminen, H. Korhonen, K. J. Lehtinen, R. Makkonen, A. Arola, T. Mielonen, S. Romakkaniemi, M. Kulmala, and H. Kokkola.

Evaluation of the sectional aerosol microphysics module SALSA implementation in ECHAM5-HAM aerosol-climate model.

*Geosci. Model Dev.*, 5:845–868, 2012.

doi: 10.5194/gmd-5-845-2012.

M. Boichu, I. Chiapello, C. Brogniez, J.-C. Péré, F. Thieuleux, B. Torres, L. Blarel, A. Mortier, T. Podvin, P. Goloub, N. Söhne, L. Clarisse, S. Bauduin, F. Hendrick, N. Theys, M. van Roozendaal, and D. Tanré.

Tracking far-range air pollution induced by the 2014-15 bárdarbunga fissure eruption (Iceland).

*Atmos. Chem. Phys. Discuss.*, 2016.

doi: 10.5194/acp-2016-159.

T. C. Bond and R. W. Bergstrom.

Light absorption by carbonaceous particles: An investigative review.

*Aerosol Science and Technology*, 40, 27-67, 2006.

doi: 0.1080/02786820500421521.

CAMx.

CAMx user's guide: Comprehensive Air quality Model with extensions, version 5.40.

*ENVIRON International Corporation*, 2011.

B. A. Cantor.

MOC observations of the 2001 Mars planet-encircling dust storm.

*Icarus*, 186:60–96, 2007.

E. G. Chapman, W. I. Gustafson Jr., R. C. Easter, J. C. Barnard, S. J. Ghan, M. S. Pekour, and J. D. Fast.

Coupling aerosol-cloud-radiative processes in the WRF-Chem model: Investigating the radiative impact of elevated point sources.

*Atm. Chem. Phys.*, 9:945–964, 2009.

R. T. Clancy, S. W. Lee, G. R. Gladstone, W. W. McMillan, and T. Rousch.

A new model for Mars atmospheric dust based upon analysis of ultraviolet through infrared observations from Mariner 9, Viking, and Phobos.

*J. Geophys. Res.*, 100:5251–5264, 1995.

B. J. Conrath.

Thermal structure of the Martian atmosphere during the dissipation of dust storm of 1971.

*Icarus*, 24:36–46, 1975.

G. A. D’Almeida.

On the variability of desert aerosol radiative characteristics.

*J. Geophys. Res.*, 92, D3, 3017-3026, 1987.

G. A. D’Almeida, P. Koepke, and E. P. Shettle.

*Atmospheric Aerosol, Global Climatology and Radiative Characteristics.*

A. Deepak Pub., Hampton, Va., USA, 1991.

A. Davidi, A. B. Kostinski, I. Koren, and Y. Lehahn.

Observational bounds on atmospheric heating by aerosol absorption: Radiative signature of transatlantic dust.

*Geophys. Res. Lett.*, 39, L04803, 2012.

doi: 10.1029/2011GL050358.

D. W. Davies.

Effects of dust on the heating of Mars’ surface and atmosphere.

*J. Geophys. Res.*, 84,B14:8289–8293, 1979.

G. de Leeuw, E. L. Andreas, M. D. Magdalena, D. Anguelova, C. W. Fairall, E. R. Lewis, C. O’Dowd, M. Schulz, and S. E. Schwartz.

Production flux of sea spray aerosol.

*Rev. Geophys.*, 49, RG2001, 2011.

doi: 10.1029/2010RG000349.

F. Dentener, S. Kinne, T. Bond, O. Boucher, J. Cofala, S. Generoso, P. Ginoux, S. Gong, J. J. Hoelzemann, J. E. Penner, J.-P. Putand, C. Textor, M. Schulz, G. R. van der Werf, and J. Wilson.

Emissions of primary aerosol and precursor gases in the years 2000 and 1750 prescribed data-sets for aerocom.

*Atmos. Chem. Phys.*, 6, 4321-4344, 2006.

F. J. Dentener and P. J. Crutzen.

Reaction of  $N_2O_5$  on tropospheric aerosols: Impact on the global distributions of  $no_x$ ,  $O_3$ , and OH.

*J. Geophys. Res.*, 98, D4:7149–7163, 1993.

A. Elteto and O. B. Toon.

The effects and characteristics of atmospheric dust during martian global dust storm 2001A.

*Icarus*, 210:589–611, 2010.

S. Fadnavis, K. Semeniuk, L. Pozzoli, M. G. Schultz, S. D. Ghude, S. Das, and R. Kakatkar.

Transport of aerosols into the UTLS and their impact on the Asian monsoon region as seen in a global model simulation.

*Atm. Chem. Phys.*, 13:8771–8786, 2013.

doi: 10.5194/acp-13-8771-2013.

F. Fécan, B. Marticorena, and G. Bergametti.

Parametrization of the increase of the aeolian erosion threshold wind friction velocity due to soil moisture for arid and semi-arid areas.

*Ann. Geophysicae*, 17, 149-157, 1999.

J. M. Flores, R. Z. Bar-Or, N. Bluvshstein, A. Abo-Riziq, A. Kostinski, S. Borrmann, I. Koren, and Y. Rudich.

Absorbing aerosols at high relative humidity: linking hygroscopic growth to optical properties.

*Atmos. Chem. Phys.*, 12, 2012.

doi: 10.5194/acp-12-5511-2012.

F. Forget.

Improved optical properties of the Martian atmospheric dust for radiative transfer calculations in the infrared.

*Geophys. Res. Lett.*, 25-7:1105–1108, 1998.

Y. Fouquart and B. Bonnel.

Computations of solar heating of the Earth's atmosphere.

*Beitr. Phys. Atmos.*, 53:35–62, 1980.

Q. Fu, K. N. Liou, M. C. Cribb, T. P. Charlock, and A. Grossman.

Multiple scattering parameterization in thermal infrared radiative transfer.

*J. Atm. Sci.*, 54:2799–2812, 1997.

S. D. Fuerstenau.

Solar heating of suspended particles and the dynamics of Martian dust devils.

*Geophys. Res. Lett.*, 33,L19S03, 2006.

doi: 10.1029/2006GL026798.

S. Fuzzi, U. Baltensperger, K. Carlslaw, S. Decesari, H. Denier van der Gon, M. C. Facchini, D. Fowler, I. Koren, B. Langford, U. Lohmann, E. Nemitz, S. Pandis, I. Riipinen,

Y. Rudich, M. Schaap, J. G. Slowik, D. V. Spracklen, E. Vignati, M. Wild, M. Williams, and S. Gilardoni.

Particulate matter, air quality and climate: lessons learned and future needs.

*Atmos. Chem. Phys.*, 15:8217–8299, 2015.

doi: 10.5194/acp-15-8217-2015.

P. J. Gierasch and R. M. Goody.

A model of a Martian great dust storm.

*J. Atm. Sci.*, 30:169–179, 1973.

P. Ginoux, M. Chin, I. Tegen, J. M. Prospero, B. Holben, O. Dubovik, and S.-J. Lin.

Sources and simulated distributions with the of dust GOCART aerosols model.

*J. Geophys. Res.*, 106, D17, 20,255-20,273, 2001.

N. Goldenson, S. Desch, and P. Christensen.

Non-equilibrium between dust and gas temperatures in the Mars atmosphere.

*Geophys. Res. Lett.*, 35,L08813, 2008.

doi: 10.1029/2007GL032907.

S. L. Gong.

A parameterisation of sea-salt aerosol source function for sub- and super-micron particles.

*Global Biogeochem. Cycles*, 17(4),1097, 2003.

doi: 10.1029/2003GB002079.

W. Guelle, M. Schulz, Y. Balkanski, and F. Dentener.

influence of the source formulation on modeling the atmospheric global distribution of sea salt aerosol.

*J. Geophys. Res.*, 106, D21, 27,509-27,524, 2001.

R. M. Haberle, C. B. Leovy, and J. B. Pollack.

Some effects of global dust storms on the atmospheric circulation of Mars.

*Icarus*, 50:322–367, 1982.

R. M. Haberle, H. C. Houben, R. Hertenstein, and T. Herdtle.

A boundary layer model for Mars: Comparison with Viking lander and entry data.

*J. Atm. Sci.*, 50:1544–1559, 1993.

G. B. Hansen.

Control of the radiative behavior of the Martian polar caps by surface  $CO_2$  ice.

*J. Geophys. Res.*, 104, E7:16,471–16,486, 1999.

J. Haywood and O. Boucher.

Estimates of the direct and indirect radiative forcing due to tropospheric aerosol: a review.

*Rev. Geophysics*, 38, 4:513–543, 2000.

N. G. Heavens, M. I. Richardson, A. Kleinböhl, D. M. Kass, D. J. McCleese, W. Abdou, J. L. Benson, J. T. Schofield, J. H. Shirley, and P. M. Wolkenberg.

Vertical distribution of dust in the Martian atmosphere during northern spring and summer: High-altitude tropical dust maximum at northern summer solstice.

*J. Geophys. Res.*, 116,E01007, 2011a.

doi: 10.1029/2010JE003692.

N. G. Heavens, M. I. Richardson, A. Kleinböhl, D. M. Kass, D. J. McCleese, W. Abdou, J. L. Benson, J. T. Schofield, J. H. Shirley, and P. M. Wolkenberg.

The vertical distribution of dust in the Martian atmosphere during northern spring and summer: Observations by the Mars Climate Sounder and analysis of zonal average vertical dust profiles.

*J. Geophys. Res.*, 116,E04003, 2011b.

doi: 10.1029/2010JE003691.

J. D. Iversen and B. R. White.

Saltation threshold on Earth, Mars and Venus.

*Sedimentology*, 29, 111-119, 1982.

F. Jaquin, P. Gierasch, and R. Kahn.

The vertical structure of limb hazes in the Martian atmosphere.

*Icarus*, 68:442–461, 1986.

K. S. Johnson, V. A. Elrod, S. E. Fitzwater, J. N. Plant, F. P. Chavez, S. J. Tanner, R. M.

Gordon, D. L. Westphal, K. D. Perry, J. Wu, and D. M. Karl.

Surface ocean-lower atmosphere interaction in the northeast pacific ocean gyre: Aerosols, iron, and the ecosystem response.

*Global Biogeochem. Cyc.*, 17, 2, 1063, 2003.

doi: 1029/2002GB002004.

M. A. Kahre, J. R. Murphy, and R. M. Haberle.

Modeling the Martian dust cycle and surface dust reservoirs with the NASA Ames general circulation model.

*J. Geophys. Res.*, 111,E06008, 2006.

doi: 10.1029/2005JE002588.

M. A. Kahre, J. L. Hollingsworth, R. M. Haberle, and J. R. Murphy.

Investigations of the variability of dust particle sizes in the martian atmosphere using the NASA Ames General Circulation Model.

*Icarus*, 195:576–597, 2008.

J. W. Kaminski, L. Neary, J. Struzewska, J. C. McConnell, A. Lupu, J. Jarosz, K. Toyota,

S. L. Gong, J. Côté, X. Liu, K. Chance, and A. Richter.

GEM-AQ, and on-line global multiscale chemical weather modelling system: Model description and evaluation of gas phase chemistry processes.

*Atmos. Chem. Phys.*, 8:3255–3281, 2008.

J. W. Kaminski, M. Porebska, K. Semeniuk, and A. Lupu.

Impact of aviation emissions on the Arctic environments – GEM-AC model simulations.

*Conference Paper: American Geophysical Union's 46th annual Fall Meeting at San Francisco, California*, 2013.

J. F. Kok.

A scaling theory for the size distribution of emitted dust aerosols suggests climate models underestimate the size of the global dust cycle.

*Proc. Natl. Acad. Sci. U. S. A.*, 108(3):1016–1021, 2011.

doi: 10.1073/pnas.1014798108.

M. Krekov.

*Aerosol Effects on Climate*.

University of Arizona Press, USA, 1993.

C. Leovy.

Weather and climate on Mars.

*Nature*, 412:245–249, 2001.

doi: 10.1038/35084192.

J. Li.

Accounting for unresolved clouds in a 1D infrared radiative transfer model. part i: Solution for radiative transfer, including cloud scattering and overlap.

*J. Atmos. Sci.*, 59:3302–3320, 2002.

J. Li and H. W. Barker.

Accounting for unresolved clouds in a 1D infrared radiative transfer model. part ii: Horizontal variability of cloud water path.

*J. Atmos. Sci.*, 59:3321–3339, 2002.

J. Li and H. W. Barker.

A radiation algorithm with correlated k-distribution. part i: Local thermal equilibrium.

*J. Atmos. Sci.*, 62:286–309, 2005.

H. Liao, J. H. Seinfeld, P. J. Adams, and L. J. Mickley.

Global radiative forcing of coupled tropospheric ozone and aerosols in a unified general circulation model.

*J. Geophys. Res.*, 109, D16207, 2004.

doi: 10.1029/2003JD004456.

K. N. Liou.

*An Introduction to Atmospheric Radiation*, volume 84 of *International Geophysics Series*.

Academic Press, 2 edition, 2002.

X. Liu, R. C. Easter, S. J. Ghan, R. Zaveri, P. Rasch, X. Shi, J.-R. Lamarque, A. Gettelman,

H. Morrison, F. Vitt, A. Conley, S. Park, R. Neale, C. Hannay, A. M. L. Ekman, P. Hess,

N. Mahowald, W. Collins, M. J. Iacono, C. S. Bretherton, M. G. Flanner, and D. Mitchell.

Toward a minimal representation of aerosols in climate models: description and evaluation in the Community Atmosphere Model CAM5.

*Geosci. Model Dev.*, 5:709–739, 2012.

doi: 10.5194/gmd-5-709-2012.

U. Lohmann and J. Feichter.

Global indirect aerosol effects: a review.

*Atmos. Chem. Phys.*, 5:715–737, 2005.

A. Lupu, K. Semeniuk, J. W. Kaminski, and J. C. McConnell.

GEM-AC: A stratospheric-tropospheric global and regional model for air quality and climate change - evaluation of gas-phase properties.

In P. Bernath, editor, *The Atmospheric Chemistry Experiment ACE at 10: A Solar Occultation Anthology*, pages 285–293. A. Deepak Publishing, Hampton, Virginia, 2013.

J. B. Madeleine, F. Forget, E. Millour, L. Montabone, and M. J. Wolff.

Revisiting the radiative impact of dust on Mars using the LMD Global Climate Model.

*J. Geophys. Res.*, 116,E11010, 2011.

doi: 10.1029/2011JE003855.

N. Mahowald, D. S. Ward, S. Kloster, M. G. Flanner, C. L. Heald, N. G. Heavens, P. G. Hess, J.-F. Lamarque, and P. Y. Chuang.

Aerosol impacts on climate and biogeochemistry.

*Annual Review of Environment and Resources*, 36:45–74, 2011.

doi: 10.1146/annurev-environ-042009-094507.

G. W. Mann, K. S. Carslaw, D. V. Spracklen, D. A. Ridley, P. T. Manktelow, M. P. Chipperfield, S. J. Pickering, and C. E. Johnson.

Description and evaluation of GLOMAP-mode: a modal global aerosol microphysics model for the UKCA composition-climate model.

*Geosci. Model Dev.*, 3:519–551, 2010.

doi: 10.5194/gmd-3-519-2010.

W. J. Markiewicz, R. M. Sablotny, H. U. Keller, N. Thomas, D. Titov, and P. H. Smith.

Optical properties of the Martian aerosols as derived from Imager for Mars Pathfinder midday sky brightness data.

*J. Geophys. Res.*, 104:9009–9017, 1999.

E. M. Mårtensson, E. D. Nilsson, G. de Leeuw, L. H. Cohen, and H.-C. Hansson.

Laboratory simulations and parameterisation of the primary marine aerosol production.

*J. Geophys. Res.*, 108(D9),4297, 2003.

doi: 10.1029/2002JD002263.

B. Marticorena and G. Bergametti.

Modeling the atmospheric dust cycle: 1. design of a soil-derived dust emissionscheme.

*J. Geophys. Res.*, 100, D8, 16,415-16,430, 1995.

doi: 10.3354/meps06930.

B. Marticorena, G. Bergametti, B. Aumont, Y. Callot, C. N'Doumé, and M. Legrand.

Modeling the atmospheric dust cycle 2. simulation of saharan dust sources.

*J. Geophys. Res.*, 102, D4, 4387-4404, 1997.

D. J. McCleese, N. G. Heavens, J. T. Schofield, W. A. Abdou, J. L. Bandfield, S. B. Calcutt, P. G. J. Irwin, D. M. Kass, A. Kleinböhl, S. R. Lewis, D. A. Paige, P. L. Read, M. I. Richardson, J. H. Shirley, F. W. Taylor, N. Teanby, and R. W. Zurek.

Structure and dynamics of the Martian lower and middle atmosphere as observed by the Mars Climate Sounder: Seasonal variations in zonal mean temperature, dust, and water ice aerosols.

*J. Geophys. Res.*, 115,E12016, 2010.

doi: 10.1029/2010JE003677.

R. McGraw, S. Nemesure, and S. E. Schwartz.

Properties and evolution of aerosols with size distributions having identical moments.

*J. Aerosol Sci.*, 29, 7:761–772, 1998.

E. C. Monahan, D. E. Spiel, and K. L. Davidson.

*A model of marine aerosol generation via whitecaps and wave disruption.*

D. Reidel, Norwell, Mass., 1986.

F. Montmessin, P. Rannou, and M. Cabane.

New insights into Martian dust distribution and water-ice cloud microphysics.

*J. Geophys. Res.*, 107, 2002.

doi: 10.1029/2001JE001520.

W. T. Morgan, B. Ouyang, J. D. Allan, E. Aruffo, P. Di Carlo, O. J. Kennedy, D. Lowe,

M. J. Flynn, P. D. Rosenberg, P. I. Williams, R. Jones, G. B. McFiggans, and H. Coe.

Influence of aerosol chemical composition on  $\text{N}_2\text{O}_5$  uptake: airborne regional measurements in northwestern europe.

*Atmos. Chem. Phys.*, 15:973–990, 2015.

doi: 10.5194/acp-15-973-2015.

Nobuhito Mori, Tomoya Shimura, Sota Nakajo, Tomohiro Yasuda, and Hajime Mase.

Multi-model ensemble projection of future coastal climate change.

*Coastal Engineering Proceedings*, 1(33), 2012.

URL <http://journals.tdl.org/icce/index.php/icce/article/view/6448>.

C. E. Newman, S. R. Lewis, P. L. Read, and F. Forget.

Modelling the Martian dust cycle: 1. representations of dust transport processes.

*J. Geophys. Res.*, 107, E2, 5123, 2002a.

doi: 10.1029/2002JE001910.

C. E. Newman, S. R. Lewis, P. L. Read, and F. Forget.

Modelling the martian dust cycle; 2. multiannual radiatively active dust transport simulations.

*J. Geophys. Res.*, 107, E2, 5124, 2002b.

doi: 10.1029/2002JE001920.

C. E. Newman, S. R. Lewis, and P. L. Read.

The atmospheric circulation and dust activity in different orbital epochs on Mars.

*Icarus*, 174:135–160, 2005.

J. Ovadnevaite, A. Manders, G. de Leeuw, D. Ceburnis, C. Monahan, A.-I. Partanen, H. Korhonen, and C. D. O’Dowd.

A sea spray aerosol flux parameterization encapsulating wave state.

*Atmos. Chem. Phys.*, 14, 1837-1852, 2014.

doi: 10.5194/acp-14-1837-2014.

R. C. Owen and A. L. Steiner.

Effect of emissions inventory versus climate model resolution on radiative forcing and precipitation over the continental United States.

*J. Geophys. Res.*, 117, D05201, 2012.

doi: 10.1029/2011JD016096.

Y. Peng, K. von Salzen, and J. Li.

Simulation of mineral dust aerosol with piecewise log-normal approximation (PLA) in CanAM4-PAM.

*Atmos. Chem. Phys.*, 12:6891–6914, 2012.

doi: 10.5194/acp-12-6891-2012.

R. Pincus, H. W. Barker, and J.-J. Morcrette.

A fast, flexible, approximate technique for computing radiative transfer in inhomogeneous cloud fields.

*J. Geophys. Res.*, 108,D13,4376, 2003.

doi: 10.1029/2002JD003322.

U. Poeschl.

Atmospheric aerosol: Composition, transformation, climate and health effects.

*Angew. Chem. Int. Ed.*, 44:7520–7540, 2005.

doi: 10.1002/anie.200501122.

M. Porebska, J. Struzewska, and J. W. Kaminski.

High resolution dynamical-chemical modelling of the upper troposphere and lower stratosphere region over the arctic: GEM-AC model simulations for current climate with and without aviation emissions.

*Conference Paper: 15th EMS Annual Meeting & 12th European Conference on Applications of Meteorology (ECAM) at Sofia, Bulgaria*, 12:EMS2015–24, 2015.

A. Pozzer, A. de Meij, K. J. Pringle, H. Tost, U. M. Doering, J. van Aardenne, and J. Lelieveld.

Distributions and regional budgets of aerosols and their precursors simulated with the EMAC chemistry-climate model.

*Atmos. Chem. Phys.*, 12:961–987, 2012.

doi: 10.5194/acp-12-961-2012.

K. J. Pringle, H. Tost, S. Message, B. Steil, D. Giannadaki, A. Nenes, C. Fountoukis, P. Stier, E. Vignati, and J. Lelieveld.

Description and evaluation of GMXe: a new aerosol submodel for global simulations (v1).

*Geosci. Model Dev.*, 3:391–412, 2010.

doi: 10.5194/gmd-3-391-2010.

J.-P. Putaud, F. Raes, R. Van Dingenen, E. Brüggeman, M.-C. Facchini, S. Decesari, S. Fuzzi, R. Gehrig, C. Hüglin, P. Laj, G. Lorbeer, W. Maenhaut, N. Mihalopoulos, K. Müller,

X. Querol, S. Rodriguez, J. Schneider, G. Spindler, H. ten Brink, K. Toersth, and A. Wiedensohler.

A european aerosol phenomenology 2: Chemical characteristics of particulate matter at kerbside, urban, rural, and background sites in Europe.

*Atmos. Environ.*, 38, 2579-2595, 2004.

doi: 10.1016/j.atmosenv.2004.01.041.

S. C. R. Rafkin.

A positive radiative-dynamic feedback mechanism for the maintenance and growth of Martian dust storms.

*J. Geophys. Res.*, 114,E01009, 2009.

doi: 10.1029/2008JE003217.

S. C. R. Rafkin, A. Rothchild, T. I. Michaels, and Sr. R. A. Pielke.

Interaction of radiation and dust (WEIRD) and the growth and maintenance of local dust storms on Mars.

*submitted: International Journal of Mars Science and Exploration*, 2011.

S. Ramachandran and S. Kedia.

Aerosol-precipitation interactions over India: Review and future perspectives.

*Adv. Meteorol.*, 2013.

doi: 10.1155/2013/649156.

V. Ramanathan, P. J. Crutzen, J. T. Kiehl, and D. Rosenfeld.

Aerosol, climate, and the hydrological cycle.

*Science*, 294:2119–2124, 2001.

doi: 10.1126/science.1064034.

N. Riemer, H. Vogel, B. Vogel, B. Schell, I. Ackermann, C. Kessler, and H. Hass.

Impact of the heterogeneous hydrolysis of  $\text{N}_2\text{O}_5$  on chemistry and nitrate aerosol formation in the lower troposphere under photosmog conditions.

*J. Geophys. Res.*, 108, D4, 4144, 2003.

doi: 10.1029/2002JD00243.

H. U. Riisgård and P. S. Larsen.

Viscosity of seawater controls beat frequency of water-pumping cilia and filtration rate of mussels *mytilus edulis*.

*Mar. Ecol. Prog. Ser.*, 343, 141-150, 2007.

doi: 10.3354/meps06930.

C. Risi, D. Noone, J. Worden, C. Frankenberg, G. Stiller, M. Kiefer, B. Funke, K. Walker, P. Bernath, M. Schneider, S. Bony, J. Lee, D. Brown, and C. Sturm.

Process-evaluation of tropospheric humidity simulated by general circulation models using water vapour isotopic observations: 2. Using isotopic diagnostics to understand the mid and upper tropospheric moist bias in the tropics and subtropics.

*J. Geophys. Res.*, 117,D05304, 2012.

doi: 10.1029/2011JD016623.

L. D. Rotstayn, M. D. Keywood, B. W. Forgan, A. J. Gabric, I. E. Galbally, J. L. Gras, A. K. Luhar, G. H. McTainsh, R. M. Mitchell, and S. A. Young.

Possible impacts of anthropogenic and natural aerosols on Australian climate: a review.

*Int. J. Climatol.*, 29:461–479, 2009.

doi: 10.1002/joc.1729.

M. Santee and D. Crisp.

Thermal structure and dust loading of the Martian atmosphere during late southern summer: Mariner 8 revisited.

*J. Geophys. Res.*, 98:3261–3279, 1993.

M. Schulz, Y. Balkanski, W. Guelle, and F. Dulac.

Role of aerosol size distribution and source location in a three-dimensional simulation of a Saharan dust episode tested against satellite-derived optical thickness.

*J. Geophys. Res.*, 103, D9, 10,579-10,592, 1998.

N. A. J. Schutgens, D. G. Partridge, and P. Stier.

The importance of temporal collocation for the evaluation of aerosol models with observations.

*Atmos. Chem. Phys.*, 16:1065–1079, 2016.

doi: 10.5194/acp-16-1065-2016.

S. C. Sherwood.

Maintenance of the free tropospheric tropical water vapor distribution. part ii: Simulation of large-scale advection.

*J. Climate*, 11:2919–2934, 1996.

M. D. Smith.

Interannual variability in TES atmospheric observations of Mars during 1999-2003.

*Icarus*, 167:148–165, 2004.

M. H. Smith and N. M. Harrison.

The sea spray generation function.

*J. Aerosol Sci.*, 29, Suppl 1, S189-190, 1998.

M. Sofiev, R. Vankevich, T. Ermakova, and J. Hakkarainen.

Global mapping of maximum emission heights and resulting profiles of wildfire emissions.

*Atmos. Chem. Phys.*, 13:7039–7052, 2013.

doi: 10.5194/acp-13-7039-2013.

- M. Spada, O. Jorba, C. Pérez García-Pando, Z. Janjic, and J. M. Baldasano.  
Modeling and evaluation of the global sea-salt aerosol distribution: sensitivity to emission schemes and resolutions effects at coastal/orographic sites.  
*Atmos. Chem. Phys.*, 13:11735–11755, 2013.  
doi: 10.5194/acp-13-11735-2013.
- C. Spyrou, C. Mitsakou, G. Kallos, P. Louka, and G. Vlastou.  
An improved limited area model for describing the dust cycle in the atmosphere.  
*J. Geophys. Res.*, 115, D17211, 2010.  
doi: 10.1029/2009JD013682.
- P. Stier, J. Feichter, S. Kinne, S. Kloster, E. Vignati, J. Wilson, L. Ganzeveld, I. Tegen, M. Werner, Y. Balkanski, M. Schulz, O. Boucher, A. Minikin, and A. Petzold.  
The aerosol-climate model ECHAM5-HAM.  
*Atmos. Chem. Phys.*, 5:1125–1156, 2005.
- P. Stier, J. H. Seinfeld, S. Kinne, and O. Boucher.  
Aerosol absorption and radiative forcing.  
*Atmos. Chem. Phys.*, 7, 5237-5261, 2007.
- Y. Tang, G. R. Carmichael, I. Uno, J.-H. Woo, G. Kurata, B. Lefer, R. E. Shetter, H. Huang, B. E. Anderson, M. A. Avery, A. D. Clarke, and D. R. Blake.  
Impacts of aerosols and clouds on photolysis frequencies and photochemistry during TRACE-P: 2. three-dimensional study using a regional chemical transport model.  
*J. Geophys. Res.*, 108, D21, 2003.  
doi: 10.1029/2002JD003100.
- M. G. Tomasko, L. R. Doose, M. Lemmon, P. H. Smith, and E. Wegryn.  
Properties of dust in the Martian atmosphere from the Imager on Mars Pathfinder.

*J. Geophys. Res.*, 104:8987–9007, 1999.

O. B. Toon, C. P. McKay, and T. P. Ackerman.

Rapid calculation of radiative heating rates and photodissociation rates in inhomogeneous multiple scattering atmospheres.

*J. Geophys. Res.*, 94:16,287–16,301, 1989.

E. C. Tuazon, R. Atkinson, C. N. Plum, A. M. Winer, and Jr. J. N. Pitts.

The reaction of gas phase  $\text{N}_2\text{O}_5$  with water vapor.

*Geophys. Res. Lett.*, 10:953–956, 1983.

S. A. Twomey.

The nuclei of natural cloud formation. part ii: the supersaturation in natural clouds and the variation of cloud droplet concentrations.

*Geofis. Pure Appl.*, 43:227–242, 1959.

E. Vignati, J. Wilson, and P. Stier.

M7: An efficient size-resolved aerosol microphysics module for large-scale aerosol transport models.

*J. Geophys. Res.*, 109,D22202, 2004.

doi: 10.1029/2003JD004485.

K. von Salzen.

Piecewise log-normal approximation of size distributions for aerosol modelling.

*Atmos. Chem. Phys.*, 6:1351–1372, 2006.

K. Wang, Y. Zhang, A. Nenes, and c. Fountoukis.

Implementation of dust emission and chemistry into the community multiscale air quality modeling system and initial application to an asian dust storm episode.

*Atmos. Chem. Phys.*, 12, 10209-10237, 2012.

doi: 10.5194/acp-12-10209-2012.

M. Wang, S. Ghan, R. Easter, M. Ovchinnikov, X. Liu, E. Kassianov, Y. Qian, W. I. Gustafson Jr., V. E. Larson, D. P. Schanen, M. Khairoutdinov, and H. Morrison.

The multi-scale aerosol-climate model PNNL-MMF: model description and evaluation.

*Geosci. Model Dev.*, 4:137–168, 2011.

doi: 10.5194/gmd-4-137-2011.

T. Wang, S. Li, Y. Shen, J. Deng, and M. Xie.

Investigations on direct and indirect effect of nitrate on temperature and precipitation in China using a regional climate chemistry modeling system.

*J. Geophys. Res.*, 115,D7, 2010.

doi: 10.1029/2009JD013264.

B. R. White.

Soil transport by winds on Mars.

*J. Geophys. Res.*, 84, B9, 1979.

R. J. Wilson, R. M. Haberle, J. Noble, A. F. C. Bridger, J. Schaeffer, J. R. Barnes, and B. A. Cantor.

Simulation of the 2001 planet-encircling dust storm with the NASA/NOAA Mars general circulation model.

*LPI Contrib.*, 1447:9023, 2008.

W. J. Wiscombe.

Mie scattering calculations: Advances in technique and fast, vector-speed computer codes. NCAR technical note NCAR/TN-140+STR, National Center for Atmospheric Research, Boulder, Colorado, 80307, 1979.

M. J. Wolff and R. T. Clancy.

Constraints on the size of Martian aerosols from Thermal Emission Spectrometer observations.

*J. Geophys. Res.*, 108(E9),5097, 2003.

doi: 10.1029/2003JE002057.

M. J. Wolff, M. D. Smith, R. T. Clancy, R. Arvidson, M. Kahre, F. Seelos IV, S. Murchie, and H. Savijävi.

Wavelength dependence of dust aerosol single scattering albedo as observed by the Compact Reconnaissance Imaging Spectrometer.

*J. Geophys. Res.*, 114, E00D04, 2009.

doi: 10.1029/2009JE003350.

M. C. Wyant, C. S. Bretherton, R. Wood, G. R. Carmichael, A. Clarke, J. Fast, R. George, W. I. Gustafson Jr., C. Hannay, A. Lauer, Y. Lin, J.-J. Morcrette, J. Mulcahy, P. E. Saide, S. N. Spak, and Q. Yang.

Global and regional modeling of clouds and aerosol in the marine boundary layer during the VOCALS: the VOCA intercomparison.

*Atmos. Chem. Phys.*, 15:153–172, 2015.

doi: 10.5194/acp-15-153-2015.

H. Yu, Y. J. Kaufman, M. Chin, g. Feingold, L. A. Remer, T. L. Anderson, Y. Balkanski, N. Bellouin, O. Boucher, S. Christopher, P. DeCola, R. Kahn, D. Koch, M. S. Reddy, M. Schulz, T. Takemura, and M. Zhou.

A review of measurement-based assessments of the aerosol direction radiative effect and forcing.

*Atmos. Chem. Phys.*, 6:613–666, 2006.

S. Yu and Y. Zhang.

An examination of the effects of aerosol chemical composition and size on radiative properties of multi-component aerosols.

*Atmospheric and Climate Sciences*, 1:19–32, 2011.

doi: 10.4236/acs.2011.12003.

C. S. Zender, H. Bian, and D. Newman.

Mineral dust entrainment and deposition (DEAD) model: Description and 1990s dust climatology.

*J. Geophys. Res.*, 108, D14, 4416, 2003.

doi: 10.1029/2002JD002775.

K. Zhang, H. Wan, B. Wang, M. Zhang, J. Feichter, and X. Liu.

Tropospheric aerosol size distributions simulated by three online global aerosol models using the M7 microphysics module.

*Atmos. Chem. Phys.*, 10:6409–6434, 2010.

doi: 10.5194/acp-10-6409-2010.

R. W. Zurek.

Solar heating of the Martian dusty atmosphere.

*Icarus*, 35:196–203, 1978.